Electrothermal Modelling for Doubly Fed Induction Generator Converter Reliability in Wind Power

PETER BRUCE WYLLIE

Electrothermal Modelling for Doubly Fed Induction Generator Converter Reliability in Wind Power

Peter Bruce Wyllie

Thesis submitted towards the
degree of Doctor of Philosophy

Energy Group
School of Engineering and Computing Sciences
Durham University
United Kingdom
July 2014

Electrothermal Modelling for Doubly Fed Induction Generator Converter Reliability in Wind Power

Peter Bruce Wyllie

Abstract

Increased reliance upon renewable energy sources, chiefly wind, places a growing emphasis on the reliability of the technology used in Wind Turbines. The current Wind Turbine fleet is dominated by the Doubly Fed Induction Machine WT, which utilises a partially rated power electronic converter to vary the speed of the rotor and thus ensure the maximum energy capture available from the wind. This converter is associated with a significant percentage of WT failures. This thesis examines the low frequency temperature cycling occurring in one half of the back to back converter which results in a high failure rate of the rotor side converter as compared to the grid side converter. To this end a MATLAB/PLECS model was constructed to demonstrate the temperature cycling occurring in a 2.5MW DFIG WT. Lifetime of the semiconductor devices was extrapolated. An adaptation to the standard Maximum Power Point Tracking control method was suggested in which the lowest operating frequencies (less than 2.33Hz) were avoided. In doing so, lifetime was observed to increase at a minor cost to energy yield from the WT.

Declaration

The work in this thesis is based on research carried out in the Energy Group, School of Engineering and Computing Sciences, Durham University. No part of this report has been submitted elsewhere for any other degree or qualification and it is all my own work unless referenced to the contrary in the text.

Acknowledgments

I would like to express my sincere thanks to my supervisor Prof Li Ran, for his considerable support, advice, patience and above all encouragement over the course of this thesis.

I would also like to thank Dr Rob Dominy who had the thankless task of dragging me across the finishing line at a time when my motivation was flagging. Further thanks go to my colleagues in the Energy Group of whom there are too many to name, but who all made the process great fun and were a great resource of technical (and less technical) information.

I am indebted to all the technical staff who assisted me in the development of the test rig, including Paul Jarvis, Colin Wintrip, Ian Hutchison, Neil Clarey, Ian Garrett and Martin Feeney. Special thanks are due to David Jones, whose years of experience and vast knowledge were invaluable as were his countless anecdotes. Thanks also to Terry Ho for doing much of the initial work troubleshooting on the test rig and taking time to give advice on issues throughout. Also thanks to Mahmoud Zaggout for his input in regards to the test rig. Prof Aurelio Garcia-Cerrada also deserves my thanks for his enthusiasm and technical expertise on tuning the controller for the test rig.

For his unending train of anecdotes alone, but also for his boundless energy and passion for Wind Power, thanks to Prof Peter Tavner (DSc).

Finally thanks to Wenjuan for unfailing encouragement and support.

This research was made possible by funding from the UK Engineering and Physical Sciences Research Council (EPSRC) via the Energy China FRENS Consortium EP/F061811/1.

For my Mum and Dad

Contents

List of Figures

List of Tables

Nomenclature

A	availability
ASD	adjustable speed drives
A_{wt}	rotor swept area
C_{dc}	DC link capacitance
c_{p_max}	maximum coefficient of performance
CREW	Continuous Reliability Enhancement for Wind
CTE	coefficient of thermal expansion
C_{th}	thermal capacitance
$C_{th\_initial\_temp}$	initial temperature of thermal capacitance
CTM	constant torque control
DFIG	doubly fed induction generator
DFIM	doubly fed induction machine
e	dq reference frame
E_{on+off}	switching on + off loss energy
E_r^R	rotor Back EMF
E_{rr}	reverse recovery
E_s	stator Back EMF
$freq_{Tj}$	frequency of temperature cycling
GSC	grid side converter
I_a	armature current
i_{ag}	grid side converter current phase a
i_{ar}	rotor current phase a
i_{ar}	rotor current phase c
i_{as}	stator current phase a
i_{br}	rotor current phase b
i_{bs}	stator current phase b
i_c	collector current
i_{cs}	stator current phase c
i_{dg}	grid side converter current d component
i_{dg_ref}	grid side converter current d component reference
i_{dr}	rotor current d component
i_{dr_ref}	rotor current d component reference
i_{ds}	stator current d component
IEA	International Energy Agency
I_f	field current
i_f	diode forward current

i_{or}	rotor side converter DC link current
i_{os}	grid side converter DC link current
i_{qg}	grid side converter current q component
i_{qg_ref}	grid side converter current q component reference
i_{qr}	rotor current q component
i_{qs}	stator current q component
i_r	rotor current
I_{r_max}	rotor current at max speed
I_{r_synch}	rotor current at synchronous speed
i_s	stator current
I_{s_max}	stator current at maximum speed
I_{s_synch}	stator current at synchronous speed
k	power curve constant
K_t	machine constant
K_t'	machine constant
L_l	line leakage inductance
L_{lr}	rotor leakage inductance
L_{ls}	stator leakage inductance
L_m	magnetising inductance
L_r	rotor inductance
L_s	stator inductance
m	modulation index
MTTF	mean time to failure
MTTR	mean time to repair
N_f	number of cycles to failure
N_r	rotor turns
N_s	stator turns
N_{sr}	turns ratio
P	power
$P_{\ loss\ conduction}$	conduction power loss
P_e	stator power
P_{gsc}	grid side converter power
P_{gsc_loss}	grid side converter power loss
P_m	mechanical power
P_{max}	maximum power
PMSG	permanent magnet synchronous generator
P_r	rotor power
P_{r_loss}	rotor side converter power loss
P_{r_synch}	rotor power at synchronous speed

P_s	stator power
P_{s_max}	maximum stator power
P_{sw_Tref}	switching power loss at reference temperature
P_{sw_diode}	diode switching power loss
P_{sw_IGBT}	IGBT switching power loss
P_t	total power
P_{t_max}	total power at maximum speed
P_{t_synch}	total power at synchronous speed
PWM	pulse width modulation
P_{wt}	wind turbine power
Q	reactive power
Q_{gsc}	grid side converter reactive power
Q_r	rotor side converter reactive power
Q_{r_ref}	rotor side converter reactive power reference
Q_s	stator reactive power
R	blade length
^{R}	rotor reference frame
R'_r	rotor resistance
r_{ce}	on state slope resistance
r_f	forward slope resistance
R_l	line resistance
R_m	resistance representing core loss
R_s	stator Resistance
RSC	rotor side converter
R_{th}	thermal resistance
s	slip
^{s}	stator side reference frame
s_{max}	maximum slip
t	time
TC_{Err}	temperature coefficients of the diode switching losses
TC_{Esw}	temperature coefficient of the switching losses
T_e	electromagnetic torque
T_j	junction temperature
T_{j_mean}	mean junction temperature
T_{jmax}	maximum junction temperature
T_m	mechanical torque
T_{ref}	reference temperature
v_a	grid voltage phase a
v_{abs}	stator line to line voltage ab

v_{ag}	grid side converter voltage phase a
V_{ar}	rotor voltage phase a
V_{as}	stator voltage phase a
v_{bcs}	stator line to line voltage bc
v_{bg}	grid side converter voltage phase b
V_{br}	rotor voltage phase b
V_{bs}	stator voltage phase b
v_{ce}	collector-emitter voltage
v_{ce0}	collector-emitter threshold voltage
v_{cg}	grid side converter voltage phase c
V_{cr}	rotor voltage phase c
V_{cs}	stator voltage phase c
v_d	grid voltage d component
v_{dc}	dc link voltage
v_{dg}	grid side converter voltage d component
v_{dr}	rotor voltage d component
v_{ds}	stator voltage d component
v_f	forward voltage
v_{qg}	grid side converter voltage q component
v_{qr}	rotor voltage q component
v_{qs}	stator voltage q component
v_r	rotor voltage
V_{r_fund}	rotor voltage, fundamental component
V_{r_synch}	rotor voltage at synchronous speed
V_s	stator voltage rms
v_s	stator voltage
v_w	wind speed
WMEP	Wissenschaftliches Mess und Evaluierungsprogramm
WSD	Windstats Germany
WSDK	Windstats Denmark
WT	Wind Turbine
X'_r	rotor reactance
X_m	stator magnetizing reactance
X_s	stator reactance
Z_{ls}	stator leakage impedance
ΔT_j	temperature cycle magnitude
θ	blade angle
θ_r	rotor angle
$\theta_{r\ offset}$	encoder offset angle

θ_v	grid voltage angle
θ_{vs}	stator voltage angle
$\theta_{\psi s}$	stator flux linkage angle
λ	failure rate
λ	tip speed ratio
μ	downtime
ρ	air density
σ	leakage factor
τ_m	blade torque
φ	power factor angle
ψ_{ar}	rotor flux linkage phase a
ψ_{as}	stator flux linkage phase a
ψ_{br}	rotor flux linkage phase b
ψ_{bs}	stator flux linkage phase b
ψ_{cr}	rotor flux linkage phase c
ψ_{cs}	stator flux linkage phase c
ψ_{ds}	stator flux linkage d component
ψ_g	grid flux linkage
ψ_{qr}	rotor flux linkage q component
ψ_{qs}	stator flux linkage q component
ψ_r	rotor flux linkage
ψ_s	stator flux linkage
ω_e	electrical speed
ω_{max}	maximum rotor speed
ω_r	rotor speed
ω_r	rotor speed (mechanical)
ω_s	synchronous speed

Chapter 1. **Introduction**

1.1. Decarbonising the UK power grid

The outlook for future power systems involves a great deal of work in restructuring the way we generate, transmit and use energy. The very real prospect of atmospheric CO_2 (combined with other greenhouse gases such as CH_4) reaching levels at which damaging climate change consequences will be likely, means that the continued development of renewable technologies is paramount. There are many options for decarbonising power systems each with their own strengths and weaknesses. In the absence of an outstanding solution to the problem of CO_2 abatement, the future of energy generation is likely to involve a spectrum of both traditional thermal and renewable generation technologies.

There are numerous proposed strategies for decarbonising the power system. Two possible scenarios outlined by the International Energy Agency (IEA) are shown in Figure 1-1 both require a high RE penetration. The Blue scenario aims at halving global energy-related CO_2 emissions by 2050, as compared with 2005 levels by reducing reliance on fossil fuels in so doing improving energy security. The Blue hi REN scenario modifies the Blue scenario by stipulating that 75% of global electricity production be from renewables, by 2050.

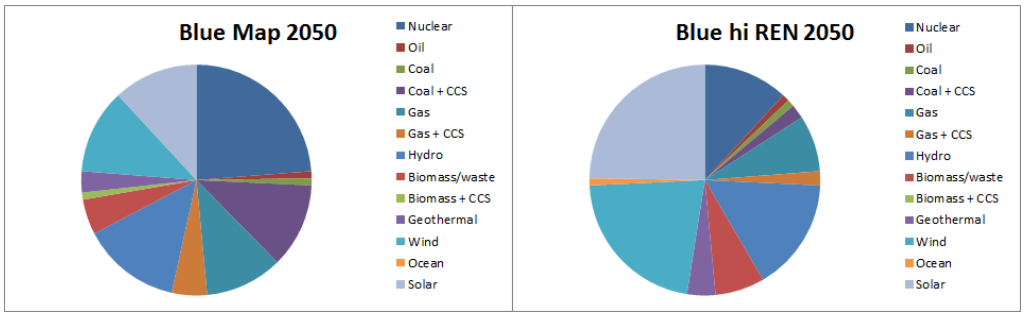

Figure 1-1 Global Energy Production for two possible scenarios [1]

Carbon capture, nuclear and solar power are all likely to play an important part in the attempt to keep greenhouse gas levels below the 450ppm of CO_2-equivalent targeted by the IEA. This level is consistent with a near 50% chance of limiting the global average temperature rise to 2°C [2]; above which some of the worst consequences of climate change are expected.

Recent investment has been encouraging. In each of the last four years (2008-2012) renewable energy made up more than half of the newly installed European generation capacity and in 2012 30GW of the 45GW installed were from renewable sources, of which 11.5GW was from wind farm installations [3]. Market leaders USA and China both installed more than 10GW of wind power in 2012.

Wind power looks set to play a significant role in climate change mitigation. Together with solar power wind has seen a rapid expansion in recent years making renewables an indispensable part of the global energy mix [4]. On its own wind may indeed provide somewhere in the region of 10-20% of the global demand by 2050 [1]. Increasing the wind penetration to such a level would require a €2.2 trillion investment over the next 40 years [5]. While this may seem like a considerable sum it indeed only represents 1% of the total spend required to maintain 2°C warming. The global investment realised in the year 2012 as operating capacity was €56 billion [6].

Despite these promising moves towards a more sustainable energy future, it is worth noting that emissions targets have been frequently revised or missed. They are often set at unambitious or unrealistic levels with deadlines far into the future so that a sense of urgency is not promoted.

Continued investment and support of wind and other renewables will also have to keep pace with the rapid development in countries like China and India. Global demand for electricity currently is growing almost twice as fast as consumption [4]. Combined with the need in many countries to replace existing generation capacity that is due for decommissioning, the need for reliable green energy technology is considerable.

1.2. Energy Security

The price and availability of other fuel types has a direct impact upon the impetus behind wind power research, development and the uptake of wind energy technology by industry and governments alike. International events can have a dramatic effect of primary fuel source pricing. The 1973 Oil Crisis saw dramatic rises in oil cost which in turn resulted in increased funding of Wind Power R&D especially in the USA. Oil prices have continued to fluctuate in response to international politics and stability of relations specifically in the Middle East. With much of the global reserves of crude oil concentrated in the less politically stable regions of the world, sustainable alternatives are becoming more and more significant in strategic energy security policy. Other fossil fuel power plants often rely on similar imports and so the price of fuel is again subject to the political conditions in the region where the resource is mined/drilled. As these fossil resources become more scarce or

more expensive to extract price will naturally increase. With an ever increasing demand for energy, ensuring a secure supply of fossil resource will become increasingly difficult. Nuclear resources are hard to gauge as most of the world's resource lies in seawater and is as yet non-recoverable. Further, as there is room for more efficient use of the resource, by means of alternative reactor technologies, the time until it is exhausted is also difficult to estimate. One estimate puts this time as 100 years based on the identified resource and consumption rate as of 2008 [7]. However as governments look to replace existing thermal power plants with non-fossil fuel generation there is potential that uranium resources will become stretched leaving a deficit to be filled by mature renewable technologies such as wind.

1.3. The importance of reliability

Reliability and efficiency are two of the most critical factors in power generation. The use of fossil fuelled power plants with steam turbines for over 100 years has led to optimised efficiencies. Renewable power technologies are less well established in main stream power generation. Despite this most renewable energy conversion systems have grown out of designs that utilised standard components that have been used in conventional generation systems or in other mainstream applications. Generators, gearboxes and power electronic converters are found in a wide variety of industrial applications and so a large body of operating experience has been built up over the years. However there is a much smaller body of operating knowledge in regards to the stochastic loading experienced by a WT drive train and electrical system over the course of the WT's expected 20 year lifetime. It is indeed this new operating environment that is the driving factor for reliability concerns. Loading in conventional power plants is forecast, planned and controlled, based on the likely demand, the fuel supply available (which with good supply chains and market stability is constant) and the need for any maintenance or cover for maintenance at other plants. Renewable technologies have often to cope with a stochastic energy source and this is the case with WTs. Wind variations can be categorised into three timescales. These are clearly visible on the Van der Hoven wind spectrum [8] as the Synoptic, Diurnal and Turbulent peaks (Figure 1-2). The wind variations are thus concentrated in the small variations caused by gusts and boundary layer effects, the daily changes caused by the earth acting as sink and source of heat during day and night respectively and the longer time scale variations caused by changes in the weather.

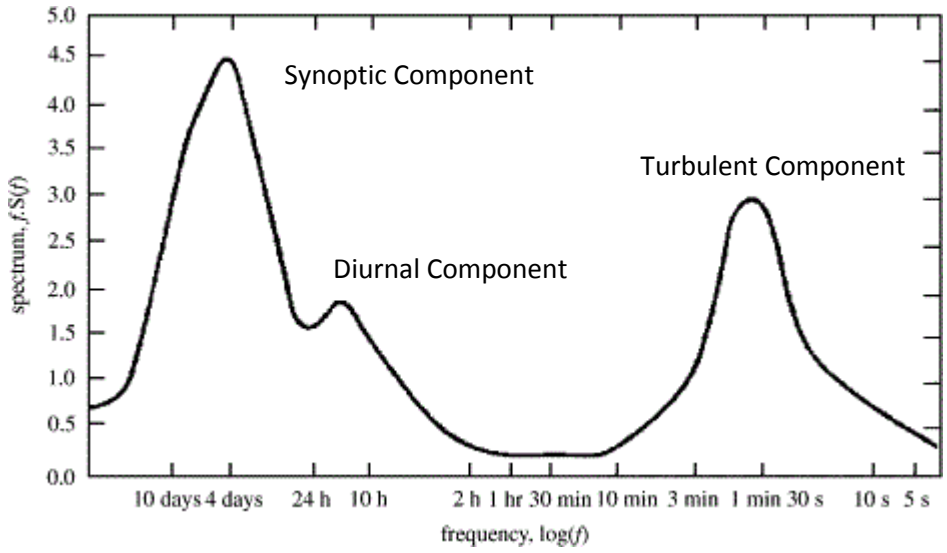

Figure 1-2 Van der Hoven horizontal wind speed spectrum [8]

Whereas the output of a traditional thermal power plant can be carefully scheduled and reserves dispatched to meet unpredicted variation in demand, a WT has to respond to the availability of the energy source across a range of timescales that do not necessarily have any correspondence to demand. This means that there is cyclic loading across a range of frequencies which the WT must withstand during the course of its lifetime.

It has been suggested that the reliability of WT can be characterised by the 'bathtub' curve [9]. This describes the lifetime distribution of failures as the combination of three functions which separately describe the early life failure, the intrinsic or random failure and the wearout failures that occur towards the end of lifetime.

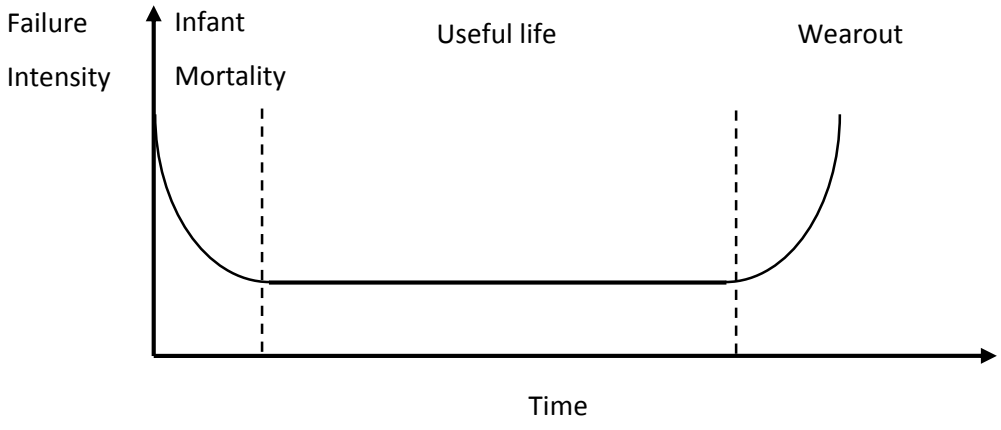

Figure 1-3 Bathtub Reliability Characteristic [10]

WT failures can have many causes and usually depend upon one subassembly failing and making the whole WT inoperable. Reliability of each component of the WT varies. Some of the WT subassemblies being more resilient to the stochastic loading or perhaps suffering a less variable load due to damping inherent in the system, contribute less to the overall failure rate of the turbine.

The failure rate does not describe the full picture of the impact of reliability upon the operation of any repairable machine. A more elucidating measure of the impact of recurrent failures requires some consideration of the inconvenience caused by the specific failures. The Mean Time to Repair (MTTR) quantifies the necessary time required to repair and thus recover from any failure. Combining this with the Mean Time to Failure (MTTF) gives a mean downtime per failure. It is the downtime per year that is of most concern to the WT operator as this will represent a loss in generating time and thus revenue.

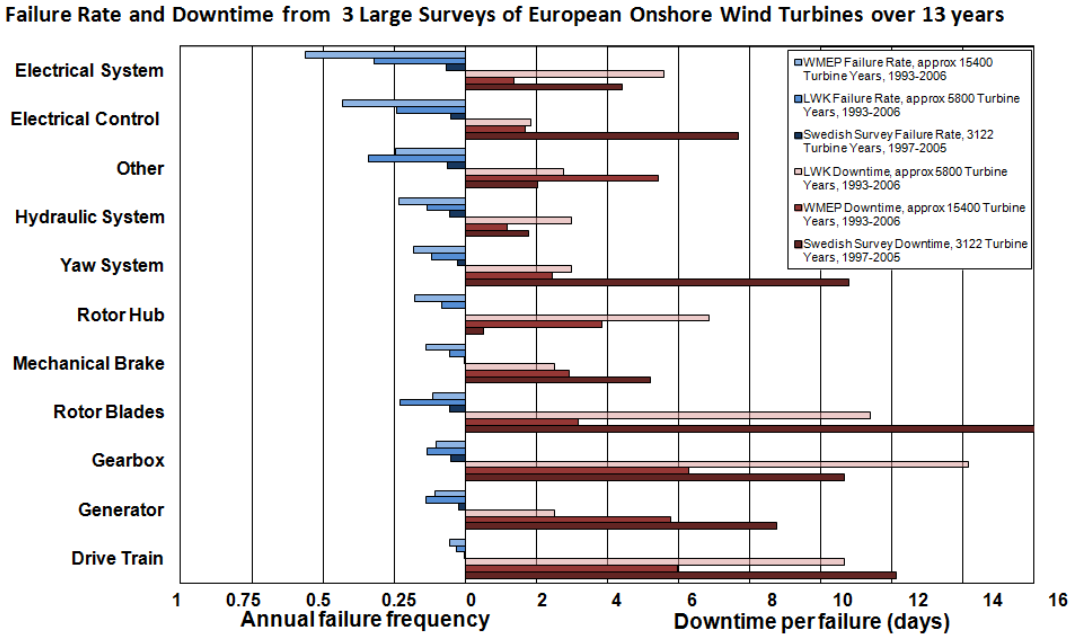

Figure 1-4 Reliability characteristic by subassembly [11] based on [12]

Figure 1-4 shows these two reliability characteristics (failure rate is used instead of MTTF) for three groups of turbines The problem with relying on MTTF alone is that it may conceal the fact that a component may require considerable effort to repair or replace; where some electrical components may be swapped with relative ease, the larger mechanical components may take more time. The gearbox for example has one of the lower failure rates according to these data, but as it is heavy and is housed in the nacelle, requires the use of a crane for removal and replacement. Downtimes for larger nacelle items are likely to be significantly longer offshore, due to access issues

for the bespoke maintenance barges. A gearbox failure may also cause significant additional damage to other drivetrain components as these are directly coupled to it. Of course any failure both mechanical and electrical may have knock on effects. Nevertheless these three sets of results follow a similar trend in terms of which subassemblies are the least/most reliable and which take the longest/shortest time to repair.

It can be seen that the subassembly, 'electrical system' has the highest MTTF and a high downtime per failure, making this one of the most significant areas for reliability improvement. A recent survey of industrial users of power electronics found that in the utility power industry and motor drive industry power semiconductor devices were the most fragile part of power converter [13]. There are several means by which a power device can fail. Some effects that are associated with failure are listed in [14] these include both chip related mechanisms which involve electrical overstress or discharge or thermally activated processes and also failure mechanisms associated with the packaging of the device such as bond wire lift off.

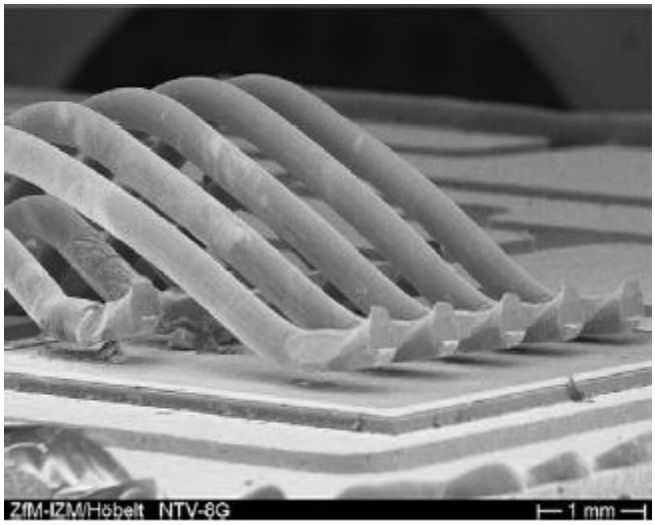

Figure 1-5 Wire bond lift-off [15]

The weak points inside a power module are indeed at the bond wire interface with the Si chip and the two solder joints [16, 17] and bond wire lift off is one of the most common failure modes [18]. At this interface there is a large Coefficient of thermal expansion (CTE) mismatch such that subjecting it to thermal cycling will induce stresses and ultimately initiate a failure. The scale, frequency and number of thermal cycles a chip is likely to experience in its lifetime will depend wholly on the application. In a WT converter there is likely to be a range of thermal cycling frequencies and magnitudes the device will be subjected to, based on the various oscillatory

components in the wind spectrum mentioned previously. The thermal profile will also depend on the type of converter the device is used in. In wind energy there are two principal WT architectures in which power electronics are incorporated. These are fully fed WTs and doubly fed WTs. Both configurations situate two converters in a back-to-back arrangement with one interfaced with the grid and operating with a fundamental frequency of 50Hz and the other connected to the generator. The generator side converter will operate within a frequency range of 10-50Hz for the fully fed WT and 0-15Hz for the doubly fed WT. Thus the grid side converter in both of these designs will experience a different electrical frequency than the generator side converter. This can have an effect upon the relative loading each converter undergoes as the thermal cycling at the device level will depend upon the frequency of current. For low frequencies the thermal impedance will be increased and so higher device temperatures cycles (ΔT) will be observed. The low frequency range of the doubly fed generator converter means it will experience large ΔT which will result in reduced lifetime [19].

Doubly Fed Induction Machines (DFIG) WTs make up 55% of the installed wind power capacity as of 2010 [20] and with manufacturers like Vestas, Sinovel, GE and REpower continuing to produce such machines and develop larger ones there is a need for an appreciation of the reliability issues effecting them, particularly in the areas where the reliability is lower. For these reason the work of this thesis is especially relevant in the expanding renewables field and in the push to mitigate the effects of manmade climate change.

1.4. Scope of this thesis

This thesis will examine the effect of low frequency temperature cycling within the power converter of a DFIG WT. Lifetime reduction will be determined and a possible solution to the problem outlined and evaluated.

The background in which the current research is carried out has been outlined above.

Chapter 2 expands on this by outlining the research effort that has been expended in the areas of power electronic reliability, thermal modelling in power electronics and modelling of the DFIG WT.

Chapter 3 provides a description of the SIMULINK/PLECS model. The control model for the WT is outlined as well as the power loss and thermal models, which determine the device losses and junction temperatures.

Chapter 4 and Chapter 5 detail the experimental work done to verify the model.

Chapter 6 examines the results from the simulation when it is run at steady state. Temperature cycling in grid and rotor side devices is compared and lifetime prediction made.

Chapter 7 describes the modifications made to the controller to mitigate the worst effects of temperature cycling by avoiding the low frequency range of operation. It also compares the results from the standard controller and modified controller and assesses the lifetime gain. The energy lost by operating off the MPPT curve at speeds close to synchronous is also assessed.

Chapter 8 provides a discussion of the work done in this thesis and presents final conclusions on the work outlined in the previous chapters as well as commenting on possibilities for further work.

1.5. Original Contribution

The current work re-examines how temperature affects the lifetime of rotor and grid side converters in a DFIG WT. The rotor side converter operates at lower frequencies and so experiences larger temperature oscillation.

The power loss variation with wind speed is determined for each device type (IGBT and diode) in the rotor side and grid side converters. An analysis of the complex power loss characteristics of each device is given, explaining the differences that occur between rotor side and grid side devices and between IGBTs and diodes of the same converter.

A novel control algorithm is suggested with the aim of avoiding operation of the WT at the most damaging operating points of the standard MPPT control curve. The new control algorithm thus represents a modified MPPT control curve. The performance of this new control approach is examined in terms of the lifetime benefit and energy sacrificed as a result of operating off the MPPT curve.

Chapter 2. **Literature Review**

The following chapter sets out the context of the current work. The main concepts in wind power reliability followed by a focus on their power converters are introduced. Next, thermal modelling techniques for power electronic applications are discussed before outlining some of the various approaches to lifetime modelling for power semiconductor devices. Finally modelling of the doubly fed induction machine is discussed.

The current work stands at the border of three fields of research (DFIG modelling, power electronics and thermal modelling) and thus this literature review encompasses a survey of the state-of-the art in these fields as well as in the intersection of the three. This review allows a suitable opportunity for novel study to be identified within the field and the boundaries of it to be set. The literature was continually revisited throughout the research process and writing of this thesis so as to maintain awareness of the room for novel insight within the chosen research domain.

2.1. Reliability in Wind Power

2.1.1. Reliability Data

Wind power generation requires the installation of large numbers of turbines at often remote locations. As such understanding the reliability issues affecting wind turbines is an important area of research in the renewables area. The reliability of a wind turbine may be characterised by various parameters including, mean time to failure (MTTF), mean time to repair (MTTR), commercial and technical availability (A), failure rate (λ) and downtime (μ). Of these the most important are the failure rate and downtime, which in combination give a measure of the time the turbine is operable and when applied separately to subassemblies, illuminate which parts of the turbine are the least reliable and the most difficult to fix.

Real wind farm reliability data is difficult to obtain as companies seek to protect their competitive edge in the market place. However some grouped datasets have been made available and methods for extracting the reliability information from grouped survey data have been proposed [9]. Tavner et al [9] analysed data from German and Danish turbines (collected as part of the Windstats surveys). The data is in two parts; Windstats Germany (WSD) which contains over 2000 WTs of

various types and with an average age over 14 years and Windstats Denmark (WSDK) with over 4000 WTs of including larger WTs and with an average age less than 3 years.

A third survey (performed by the Schleswig Holstein LandWirtschaftsKammer [21]) was used as the dataset for a study relating to different wind turbine concepts [22]. This dataset was smaller with around 640 WTs including large turbines of average age 15 years with a wide range of configurations.

Data from the Wissenschaftliches Mess und Evaluierungsprogramm (WMEP) study was used for a reliability study in [12]. This included 1435 turbines, over 95% of which were smaller machines (<560kW) although some larger machines were included. Data was collected from 1998 until 2000. The age of the WTs was not specified. Much older information is available from the US experience in the mid-1980s from the data collected by the Electric Power Research Institute (EPRI) though this data represents the early days of wind power when the prototype large American WTs had extremely high failure rates.

The Reliawind project developed a generic wind turbine taxonomy so that meaningful comparison could be made between failure rates of subassemblies of turbines of different design. Conditions were imposed upon the data permissible in the study, to try to ensure that results were comparable. These took the form of conditions limiting the variability of the turbine type and environment such that turbines with less than 2 years' operating service or from sites with less than 15 WTs in the farm were excluded. To ensure the sampled WTs reflected the current technology a minimum standard was set requiring the power rating be higher than 850kW and the WT be variable speed and pitch regulated. Older topologies were excluded [23].

A number of reports were published based on data from the Continuous Reliability Enhancement for Wind (CREW) database developed by Sandia National Laboratories [24]. The data collected from 800-900 WTs and amounting to 1.3-1.4GW of generation capacity represents 2.7% of the installed large WTs and 2.4% of the US installed wind capacity in the US. WTs in the sample are of at least 1MW size and from farms with at least 10 turbines. They include three manufacturers and a total of six WT models. Hence this survey includes a narrow range of designs which are all large enough to reflect the scale of a modern WT [25].

These grouped dataset are useful in providing the general reliability overview of WTs, though some represent older machines that are less relevant. Contemporary reliability data from the main manufacturers of WTs would be preferable as it would not only provide recent data but also data

that reflected longer spans of operation of WTs so the different stages of reliability could be clearly observed. For the current work a large set of recent data from DFIG WTs containing converter failure rates would be the ideal. Given the competitive nature of the WT industry this data is commercially sensitive and is very hard to obtain. The grouped datasets are the best option and do provide enough data to gauge the broader reliability issues affecting WTs.

2.1.2. Main subassembly reliability in wind turbines

The modern Wind Turbine combines technology from a range of mature engineering fields where there is considerable design and reliability experience. The mechanical engineering involved in constructing and operating large gearboxes is well developed as too is the structural engineering needed to fabricate tubular steel towers. Blade design and operation has the combined experience from aviation and turbine engineering to draw upon. Megawatt rated generators have supplied power for a hundred years and even the device technology in the power electronics converter is cutting edge rather than bleeding edge [26]. The elements separately presented would indicate high reliability, though experience has shown that the loading experienced in this application has significant impact upon the expected lifetime of these components.

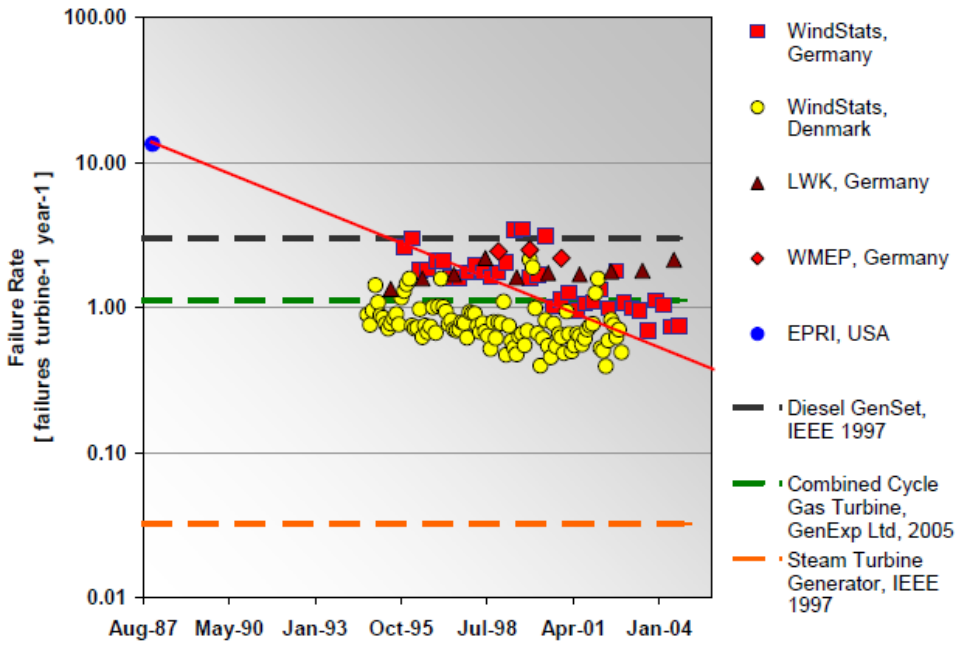

Figure 2-1 Wind Turbine Failure frequencies [22]

From Figure 2-1 comparison can be made between WT failure rates and those in other types of generator. It is apparent that the steam turbine in particular continues to have a significant reliability advantage over the WT.

2.1.3. The Gearbox

WT gearboxes often fall short of the 20 year design lifetime, requiring significant repair effort well in advance of the intended lifetime [27]. Gearbox reliability is likely to improve as more experience is gained of the dynamic loading experienced within a turbine drive train, though newer, heavier gearboxes required by larger machines may have different maintenance and reliability needs. The need for extremely high gearbox ratios and the wide variation in loading and speed means that reliability prediction and thus the prevention of failures is difficult [28]. Ribrant and Bertling observed that a decrease in gearbox failure was accompanied by an increase in downtime per failure [29]. This is possibly due to gearboxes becoming larger thus more difficult to repair/replace, as a result of the move towards ever increasing WT size.

A gearbox failure in a WT will have a significant impact upon energy yield due to the long repair times associated with such a large piece of equipment. Removal of the gearbox from the WT drivetrain by introduction of direct drive machines should improve reliability. This however, is not necessarily the case. Tavner [22] showed that the early failure frequency of direct drive generators is higher than geared machines and suggested this was due to the number of coils in the machine. The gearbox was also shown to have the lowest failure rates of the subassemblies analysed.

2.1.4. The Generator

Electrical generators in wind power have exhibited a higher failure rate when compared to similarly sized machines used in other industries [30, 31]. Though the generator is one of the more reliable subassemblies of a WT when the downtime is taken into account the availability is still unacceptably low [21, 32].

2.1.5. The Converter

Tavner et al discovered that an increase in WT failure rate between two sets of WT data (WindStats Denmark and WindStats Germany) was considered to be a result of the electrical control or system subassemblies as opposed to mechanical subsystems [9]. Further it was found that an increase in complexity in WTs could be blamed for an increase in observed early failure rate of WTs.

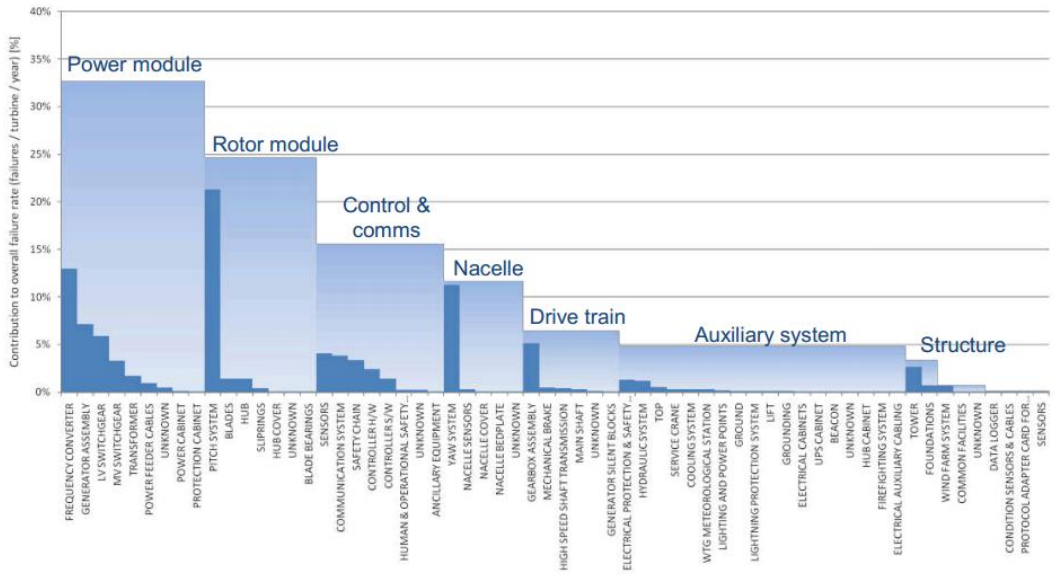

Figure 2-2 Normalised Wind Turbine failure rate by subassembly [33]

The significance of the electrical subassemblies' failure rates is apparent from the Reliawind results shown in Figure 2-2. The electrical failures are grouped under the heading "Power Module". Within this category the failure rates of the individual subsystems are shown and it is clear that the converter dominates with a failure rate only surpassed by that of the pitch system.

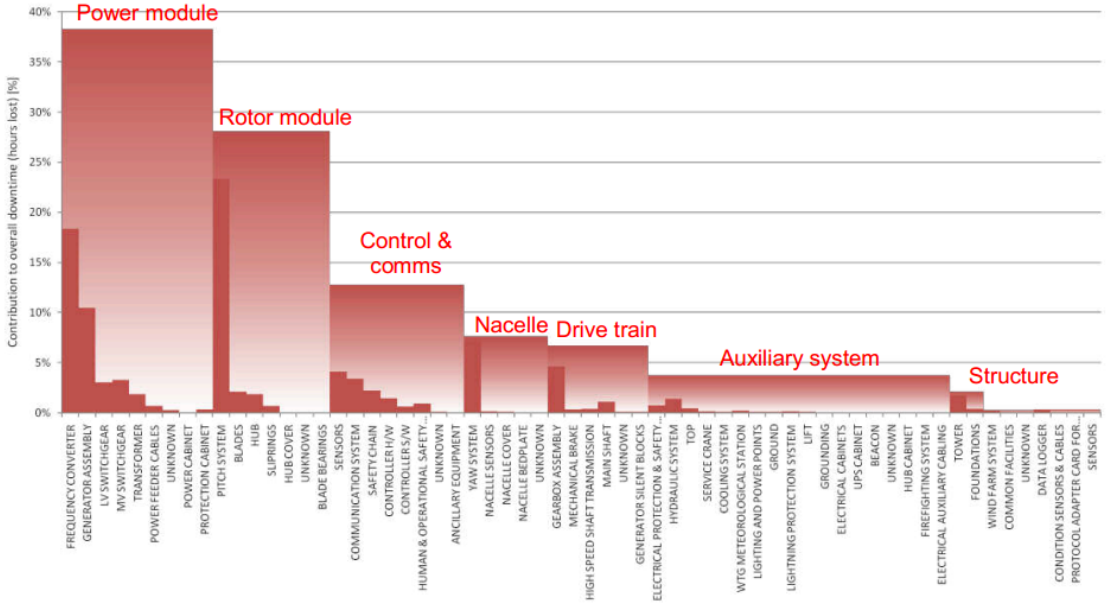

Figure 2-3 Normalised Wind Turbine downtime by subassembly [33]

The contribution of subassembly failures to the overall WT downtime follows a similar pattern (Figure 2-3). The converter being relatively easy to repair/replace means that the significance of this failure in terms of downtime is not as impressive as its contribution to the overall failure rate;

it remains however the second most significant after the pitch system in terms of subassembly contribution to the overall system downtime.

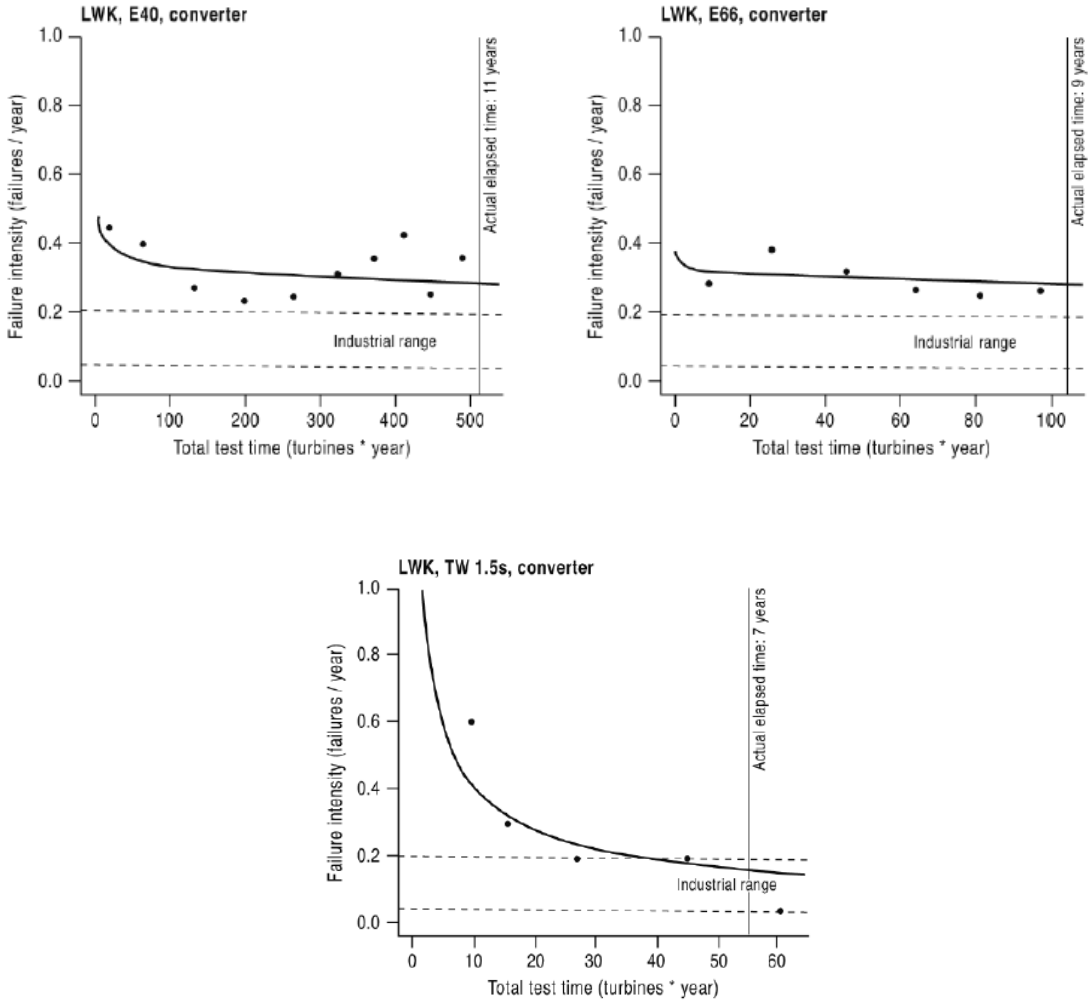

Figure 2-4 Converter failure rate in WT and other industrial application [34]

Figure 2-4 shows how WT converter failure rates compare with the failure rates of power converters in general (the dashed lines show the expected failure rates for converters taken from [35]; the data was anonymised but was from an important converter manufacturer and in [34] was taken as the industrial standard) . Though the failure rate reduces with time, the rate is still higher than the standard achieved in other industries.

Tavner [36] investigated further and found that the power electronic converters of both direct drive and geared drive turbines had higher failure rates throughout their operation than in applications

in other industries. Removing the gearbox to create DD WT designs eliminates one source of failure but is paid for by an increased aggregate failure in the converter and other electrical systems, whose reliability is observed to be less in DD WTs [37].

It is suggested that the move towards larger WT designs will place greater strain on subsystems like the converter as higher power levels and power cycling are experienced by the semiconductor devices. Increased experience with the loading scenarios in a WT may help to mitigate this.

The reliability of the converter in turn depends on the reliability of its component parts. Of these, the power semiconductor devices are considered the least reliable and the main stresses placed upon these are, environmental, transients and heavy loading [13].

Adaptive control of the dc-link voltage may be used to improve converter reliability. In [38, 39] it was shown that by controlling the dc-link voltage with reference to the operating point the dc-link voltage could be reduced from its maximum value at all operating points other than a maximum speed. Device losses are reduced and thus too the failure rate. The Cosmic Radiation-Induced Failure Mechanism is also mitigated due to the lower dc voltage.

2.2. Power Electronics

2.2.1. Thermal modelling for Power Electronics

Power converters are expensive and so replacing or repairing damaged components represents a significant financial inconvenience. The downtime incurred by the device or infrastructure to which the converter is attached will also have associated costs, which may even outweigh the replacement costs. Savings are made if the IGBTs and free wheel diodes, making up the converter, are sized correctly and thus operated close to their maximum temperature ratings. Above such an upper temperature limit, damage will be incurred by the module. Cycling of device temperature can also cause failures such as wire bond lift off [40].

Modelling of the converter allows greater control over testing and insight into junction temperature and temperature swings that cannot be measured directly on an experimental test rig. Ciappa et al [41] outlined a model calibrated using experimental data from accelerated testing for the prediction of IGBT lifetime when subjected to cyclic loading. The model only accounted for bond wire lift-off and did not factor in modern preventative measures built into IGBTs to prevent lift off of bond wire. Hui et al [42] produced an electro-thermal model for a three phase inverter which calculated IGBT temperature from an electrical mission profile. By separating switching and conduction losses a

model was developed that was applicable to converter applications where AC output frequency is variable, such as in wind power. Wei et al [43] outlined a method for junction temperature prediction especially under the low frequency/dc condition. Good prediction accuracy was possible at the dc condition when the chip to chip impedance was considered if the chips were physically close. For chips separated by a distance greater than two widths, including the chip-to-chip thermal impedance does not have any significant effect upon improving temperature prediction.

Cova et al [44] used a matrix of stress cycles with different values of ΔT_j and T_j to analyse their effect on the power cycling capability of an IGBT. They found that the T_{jmax} had a lower effect upon the device as long as a critical upper limit was not reached.

Wei et al [45] analysed the MTTF for semiconductor devices in adjustable speed drives (ASD) and found that the most stressful operating condition for a standard ASD was at the low frequency high torque condition. Increased silicon chip size or IGBT module rating can increase the MTTF significantly however, decreasing the heat sink thermal resistance only resulted in a slight improvement in MTTF.

2.2.2. The Lifetime model

Two types of lifetime model are used to predict the lifetime of power semiconductor devices. These are analytical and physical lifetime models.

For physical lifetime models knowledge of the number of cycles or indeed their amplitude is not required in order to predict life expectancy but prior knowledge of failure and deformation mechanisms is necessary. Physical modelling is based upon stress/strain knowledge that is gained either through experimentation or by simulation. For solder joint failures physical modelling can be further subdivided into four classes, stress, strain, energy and damage based models [16, 17]. Energy based models are the most comprehensive and have the ability to capture test conditions with the most accuracy [16, 46]. One such model is outlined by Ciappa et al [47]. The stress-stain response of a bimetallic interface to an arbitrary temperature profile is determined and the extrapolated stress-stain curve used to assess the accumulated energy in the module. The end of life of a device occurs when the level of accumulated deformation work reaches a critical level. This approach assumed that the only plastic deformation mechanism resulting in thermal damage was creep. Kovačević et al [17] improved upon this by including elastic, plastic and creep deformation. Stress-strain curves were determined by modelling the response of the solder to different temperature profiles. Then the total deformation energy which causes failure of the device was calculated.

Lifetime models for power semiconductor devices are used to give an estimation of the likely lifetime of such a device by paying heed to the various types of stress acting upon the device. Sources of stress upon the device vary in their intensity and their impact upon lifetime depending on the application and include, current, voltage, temperature, vibration, humidity and cosmic radiation level [16]. Analytical models express device lifetime in terms of temperate cycling parameters such as amplitude, duration, frequency, mean temperature, dwell time, maximum temperature and minimum temperature [17]. Interpreting a complex thermal mission profile in terms of these parameters requires a cycle counting technique such as peak counting, level crossing counting or rainflow counting. Three peak counting techniques (rising edge, half-cycle and maximum edge) and rainflow counting were analysed by Mainka et al [48]. The rainflow algorithm performed the best and has been used in other studies of power semiconductor device lifetimes [49, 50]. For steady state testing however a sophisticated cycling counting algorithm is not required and simple counting of the oscillations swill suffice.

For current device technology, lifetime studies have been carried out. Bayerer et al [51] analysed a large number of power cycling results from different IGBT module generations and performed multiple linear regression with respect to several variables including mean device temperature and temperature cycle magnitude to enable an empirical model of the number of cycles to failure to be established. This model was used to estimate the number of cycles to failure for 1200V-IGBT4 modules.

Held et al developed a fast cycling test method which allowed the number of cycles to failure of an IGBT to be plotted against temperature. From these results a behavioural model of cycles to failure in terms of the mean junction temperature and temperature cycle magnitude was developed [52].

2.2.3. Wind Power Application

The lifetime of semiconductor components of a converter will depend upon the environment and the particular application. The stresses experienced by a converter within a wind turbine will differ from other industrial converter applications due to the variability of the load profile. Operating frequency and power level will vary considerably and continuously, reflecting the Van der Hoven spectrum of the wind variation. Indeed the lack of a comprehensive mission profiles for evaluating converter lifetimes in wind turbine applications has been identified as a potential hurdle in ascertaining valid lifetime estimations [53].

The complex nature of the wind turbine loading may be examined by analysing the power losses and temperature excursion occurring at different operating points. Baygildina [54] quantified the

difference between IGBT and diode losses at different wind speeds, showing that at lower speeds a more even sharing of losses between the two devices occurs. The thermal dynamics of the converter devices is largely unaffected by the turbulent component of the wind.

Xie et al showed that wind turbine power converter reliability was related to the wind speed [55]. The relationship was similar to that between the WT power and wind speed. Generator rated wind speed will affect the failure rate of the converter and a seasonal variation in reliability was also outlined.

Converter types

The type of wind turbine will affect the loading experienced by the converter. The main choice is between the fully rated converter and the partially rated one used in DFIG WTs. The loading per device will also be dependent upon the type of converter used. Work has been done in understanding the operational differences between converter types insofar as this affects the device temperatures and lifetimes.

Ma et al examined the loss distribution within three different back to back converter architectures within a 10MW fully rated WT. The power loss characteristic and temperature profile of the devices were found to vary significantly [56]. Three level converters had good thermal performance on the grid side but poor performance on the generator side. A five level back to back converter displayed the best thermal performance. Arifujjaman et al analysed the reliability of four types of converter in fully rated WT application and found the use of an intermediated boost converter offered the highest reliability [57]. The machine side converter was found to be the least reliable component of the converter in all four architectures examined. Holtsmark et al compared the performance of matrix and back-to-back converters [58]. The matrix converter was shown to be significantly more efficient, with this advantage increasing as wind speed reduced from rated. Thermal fluctuations were however lower in the case of the back to back converter.

Pittini et al [59] conducted thermal analysis of the Grid Side Converter (GSC) in a Permanent Magnet Synchronous Generator (PMSG) WT. They found the worst operating point in stress upon GSC was at rated power, as might be expected seeing as the frequency is constant. Lower power and lower frequency operating conditions were found to cause less stress.

Control scheme

The particular control scheme used for DFIG WT power control has an important effect upon thermal cycling within the converter. MPPT causes significant thermal cycling due to the fact that

power from the generator and thus though the converter is maximised. Two other control methods were compared in terms of their impact upon device temperature cycling [60]. Constant Power Mode and Constant Torque Control (CTM) are both viable alternatives to MPPT which offer a lower yield in energy from the WT but were shown to cause reduced thermal cycling. Of the three control modes, CTM was shown to cause the least thermal cycling.

Wei et al outlined a method to analyse DFIG lifetime results under three control scenarios; minimal stator losses, minimal rotor losses and minimal overall losses. The lifetime of the converter is maximised by use of the minimal rotor losses control method. The lifetime of the devices for continuous steady state operation at a range of wind speeds was determined [61]. The minimal rotor losses control method gave the longest lifetimes, although this might entail an increase in the rating of the rotor side converter to allow it to supply the commanded reactive power. Only continual operation at fixed speeds was considered, and thus consideration of the ageing effect of the stochastic wind upon the DFIG converter in MPPT mode was avoided.

2.3. Low frequency temperature cycling

One of the peculiarities of the DFIG system is that lower frequencies occur, not at the low wind speed and thus low power condition (as with the fully fed system) but rather at a medium wind speed condition where current through the converter is no longer minimal.

Bartram et al modelled IGBT temperatures and verified simulation results by experiment. A load condition not found in traction applications, where high current occurs at low frequency was identified [62]. Larger temperature cycle amplitudes occurred at low frequency causing more damage. However, in any set time period the longer cycles will of course be fewer and thus the most damaging frequency is not necessarily the lowest.

Bruns examined the differences in device power losses and junction temperatures arising from the use of an MPPT variable speed controller and a controller that fixed the speed at the synchronous operating point [63]. Comparing the losses at operating points at which the generator power is the same for both control methods the losses in the synchronous controller are higher for power values on the MPPT control curve that correspond to speeds above synchronous speed and marginally lower below it. This is due to the approximate inverse proportionality of rotor current with speed, when power is held constant. Unequal loading of power devices at synchronous speed in the worst case results in the full rotor current across one leg of the inverter whilst the other two carry half. This can result in the devices on one leg of the inverter experiencing a significantly greater thermal

load than on the other legs. It was suggested that the unequal loading could be mitigated by controlling the speed of the turbine with a small slip, dependant on the thermal time constant.

Lei simulated the thermal response of devices within the Rotor Side Converter (RSC) noting the large thermal cycling at very low frequency and suggested that a critical speed range around synchronous speed could be defined and operation within it avoided by pitching the blades or controlling the torque [64].

The effect of operating at synchronous speed is also felt on the rotor windings [65]. The unsymmetrical copper losses at synchronous speed caused an overtemperature rise of 86% which limited the maximum current at the operating point.

2.4. Thermal Management and Loss Mitigation

In energy generation applications, power converters may be operated at high power levels for significant time periods and thus losses will be high. In renewable energy devices power levels will vary stochastically. By controlling these losses, device temperature may be controlled and thus damage prevented. More significantly, the device output may be maximised by using a dynamic model to predict how long higher power levels may be maintained without resulting in overtemperature. These losses depend upon the electrical and ambient conditions (i.e. voltage, current and temperature) as well as electrothemal characteristics of the semiconductor device itself.

There are two methods of loss control arising from the two electrothermal loss mechanisms operating. Switching loss is curtailed by lowering the switching frequency whilst conduction loss is managed by varying the current. These loss manipulation techniques were used in an on-line strategy to avoid overtemperature and power cycling failures [40, 66]

Blasko et al developed a thermal management strategy to reduce the thermal stress suffered by the inverter [67]. The device temperatures were estimated and if the temperature of any of the devices reached a critical level then the pulse width modulation (PWM) switching frequency was reduced or the PWM method altered. If switching losses were still high when the minimum switching frequency was reached then the current was reduced so as to keep the temperature of the hottest device below a critical level. The management strategy was most useful at low frequency.

Murdock et al proposed a thermal management method which included a shutdown mechanism to be used when the curbing of switching losses by changing PWM frequency and limiting current were together unable to reduce the device temperature below the critical limit [66]. By controlling the thermal operating performance of the module, optimal utilization of the semiconductor die side was possible and mean and cyclical thermal stress reduced.

Wei et al [68] proposed a method to limit the switching frequency based on the junction temperature cycling amplitude of the inverter IGBT. When the temperature variation was high the switching frequency was reduced. The MTTF was increased dramatically for operation when the commanded switching frequency was high and at low speed and high current conditions; though a higher converter rating might be required to carry the increased reactive current.

The stressing effects of thermal cycling may be mitigated by controlling the reactive power to smooth out the thermal stress on the IGBTs. This approach was proposed for improving the reliability of a multi megawatt WT [69]. Active power was transferred as expected to the grid whilst reactive power could be circulated between parallelised converters to reduce the thermal effects of power fluctuations. This approach would limit the damage done by the stochastic nature of the wind through large power and hence current fluctuations but it was not adapted to mitigate damage done by the thermal cycling arising at constant power operation from the oscillating current and hence power loss in output from the converters. Other studies also made use of the reactive power control to mitigate thermal cycling. Ma showed that circulating reactive power between WTs within a wind farm, could be used to mitigate thermal cycling [70]. During the minima of wind gusts, reactive current may be increased to help smooth temperature cycling in the most stressed devices without causing unacceptable stress in other devices or the converters of parallelised wind turbines.

Reactive power circulation between GSC and RSC may be used to reduce thermal cycling in either converter [71]. Under constant wind conditions reactive power injection can be used to mitigate thermal cycling by adding increased thermal loading in both converters. During wind gust reactive power circulation may be used to significantly reduce thermal cycling in the GSC whilst having little impact on the RSC.

Parallelisation of converters also provides the opportunity to selectively switch off devices to increase lifetime. In [72] Birk outlined a method for sharing real and reactive power between multiple parallelised converters within a WT which may be switched in or out such that the thermal cycling and the number of operational hours for the devices is minimised. At lower wind speeds the

losses ranged from 20 – 80kW, with all converters switched on. By selectively switching on inverters when needed the power losses could be reduced across this range by around 10kW. It was stated that this corresponded to as much as 0.2% increased annual energy yield.

There are three approaches detailed above, broadly speaking. These involve controlling, switching frequency, circulating reactive power between converters or sharing power between multiple converters.

The switching loss control approach in [66] involved a complex controller, in as much, as it applied different mitigation strategies depending on the wind speed. The control approach in [68] was less complex and had demonstrated good lifetime improvement, although both of these did not investigate the application of the control technique in a WT.

The reactive power circulation approaches were investigated within the context of WT systems. The one used in [71] had the advantage of being able to mitigate temperature cycling in both varying wind and constant wind speed conditions, whereas [69, 70] targeted the varying wind conditions.

The power sharing approach used in [72] not only reduced the number of operational hours for the converters but had the secondary benefit of enhancing production from the WT. It has also proven itself to the degree that it is utilised by Gamesa in their G10x 4.5MW WT.

There is need for more work to mitigate thermal cycling induced at constant wind speeds. A more simple, method for thermal management, involves adapting cooling techniques to reduce thermal loading of devices. Zhou et al compared the different cooling methods used in the converter and determined that although a liquid cooling system was able to achieve lower mean junction temperature the temperature fluctuations were of similar magnitude [73]. Whilst Meysenc [74] examined the relationship between cooling effectiveness and thermal inertia. An increase in cooling effectiveness reduces the mean temperature however it also has the effect of decreasing the inertia and hence increasing the thermal cycling about the mean. Adaptive cooling may also be used to reduce temperature cycling by varying the thermal impedance within the cooling system. This was achieved in [75] with considerable effectiveness at very low frequency (less than 0.5Hz); above approximately 1Hz the mitigation of thermal cycling amplitudes was reduced significantly. Again trade-off control of thermal cycling and mean temperature was observed insofar as an increase in mean temperature was observed when the control system was used.

2.5. Modelling implementation

There has been considerable research done in examining the operation of the doubly fed induction machine in wind energy applications. Early experimental work was carried out by Pena, who examined vector control of the doubly fed induction machine for wind energy generation in two papers which looked at a grid connected WT DFIG system [76] and also at the system feeding an isolated load [77].

Simulation of DFIG WTs is an established field and much work has been done in modelling the DFIG control model. Abad [78] and Krause [79] together, provide a comprehensive summary of DFIG control modelling and a detailed outlining of the machine equations for modelling the induction machine. From these a complete a mathematical model of a DFIG WT may be established.

Different aspects of the control approach have been examined in detail. Petersson et al [80] examined the use of grid flux oriented control, as opposed to stator flux orientation. The grid flux alignment allowed the DFIG system to produce as much reactive power as necessary without affecting the stability of the system. Cañas-Carretón et al [81] investigated three methods of determining the rotor reference voltage comparing whether the computational time and accuracy were improved by the addition of rotor current and cross coupling terms to the PI controller. Ekanayake [82] developed a model that was applicable to single and double cage generators and also investigated the effects of DFIG control on wind farm stability. Finally some studies have provided verification of simulated results. Tapia et al [83] developed a complete model of a DFIG WT and presented real results from a WT as verification of the model.

2.6. Conclusion

Reliability in a wind turbine may be analysed in terms of the component subassemblies which constitute the full turbine design. Some components exhibit a more significant failure potential and may require considerable commitment of resources to remedy making for a longer downtime. The power electronic converter has displayed a high failure rate in several turbine studies and despite a more modest downtime occurring for each failure the overall contribution to the total turbine yearly downtime for this subassembly is high.

Thermal modelling of power electronics can allow the junction temperature of semiconductor devices to be determined and thus the lifetimes under different loading conditions and ambient environments predicted. Within wind power applications the converter type, WT type and the

particular control scheme all have a baring upon the temperatures and temperature cycling a device junction is likely to experience. The time spent operating at particularly damaging operating points is also significant in determining device lifetime. Operation at low frequencies causes large magnitude temperature cycles and in the DFIG system in particular these low frequencies occur at non minimal currents. Thus lifetimes are effected.

Several approaches have been investigated that aim to mitigate the damage accrued in a device due to thermo mechanical stressing. These included varying switching patterns to control device loss, controlling reactive power to smooth out temperature variation. Active cooling techniques and variation of the converter thermal impedance have also been examined as strategies for controlling the temperature profile experience by devices.

Modelling of DFIG WTs is an established research field and much work has been done in using such models to investigate aspects of operation of this type of WT. The next chapter will discuss the development of a DFIG WT electrical model coupled to a thermal model of the power electronic converter. This will be used to investigate low frequency of the converter in as much as it has effect upon the temperature cycling and ultimately the lifetime of the converter.

Chapter 3. **Modelling the Doubly Fed Induction Machine**

The following chapter will discuss the modelling approach used to produce a mathematical representation of a DFIG WT. The model can be broken into six model components

- a behavioural model of the turbine rotor blade assembly
- a model of the WT controller
- a full electrical model of the DFIG and power electronic converter
- a power loss model calculating the switching, conduction and total losses in the converter
- a thermal model of the modules and heat sink within the converter
- a lifetime calculation

Validating simulation results is necessary to provide a real world check upon modelling results. Modelling the complex system of a DFIG WT necessarily involves some simplification. This may take the form of a simplifying assumption adopted during model construction by the researcher (i.e. the decision to leave out a specific element or relationship) and also may be inherent in the adoption of a particular modelling technique or mathematical formulisation. The choice of step size or solver used by Simulink will also affect the validity of the results obtained by the model.

It should be noted that most of the Simulink or PLECS modelling blocks used form part of a standard set of modelling tools used by electrical engineer. These therefore may be understood to make up a heavily tested and much relied upon modelling environment, which may in fact be used to verify experimental datasets. In the present work, however, the experimental results are used to give extra weight to the conclusion arrived at after analysis of simulation data.

3.1. Model Overview

Extra detail increases model fidelity but slows down simulation. A careful balance must be maintained between the speed of simulation and the level of detail included. Some approximations are necessary in the model (in the mechanical, electrical, power loss and thermal model). Careful consideration must be made as to the sensitivity of the model predictions to the inclusion or emission of a parameter's dependency on, for example, temperature (or indeed any other factor). Simplifying assumptions may be required to limit the size of the model, its detail or indeed the simulation time. In the WT mechanical model it was not considered vital to implement a full

aerodynamic model of the rotor blades, or the drive train for that matter. The focus in the current study is on the thermal response of the electrical system. Much insight can be gained by considering steady state conditions and so the dynamic response, the WT rotor aerodynamics and drive train mechanical detail can be overlooked, for example. In the case of the rotor, a behavioural model based on empirical formulation of the rotors torque response is preferred. Assuming such a response allows considerable saving in computing power to be made.

The six model components are grouped into three main parts: the WT-Electrical Model, the Power Loss-Thermal Model and the Lifetime calculation. The modelling is carried out in the Matlab/Simulink environment, with the electrical system and thermal circuit being modelled using the PLECS blockset whilst all other modelling is carried out in Simulink. The model structure and breakdown by simulation software is shown in Figure 3-1.

Mathworks' numerical computing environment Matlab and its graphical block diagramming tool, Simulink, have found widespread use in engineering. They have become standard tools in numerical modelling across a wide range of engineering disciplines including electrical engineering. Simulink has been used in modelling and analysis of DFIG control and electrical systems to great effect. The software provides a quick and user friendly platform for electrical simulation and has a wide range of toolboxes reducing the need to build custom model subsystems for common functions. PLECS [84] provides a simple and fast toolbox for power electronic simulation and has proved useful in simulating DFIG WT systems [85-87].

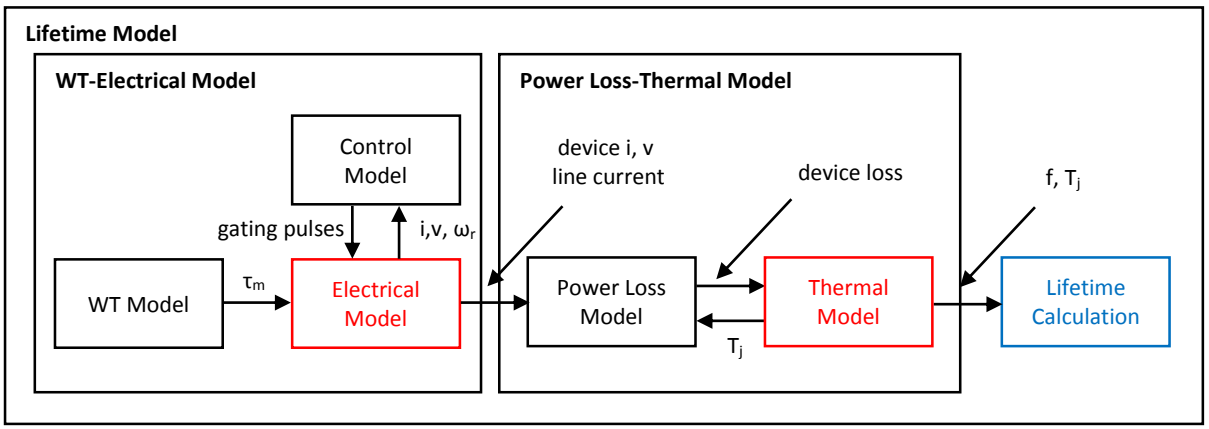

Colour denotes software used. Black: Simulink, Red: PLECS Blockset, Blue: Matlab Script

Figure 3-1 Lifetime Model outline.

To examine the effect of one particular operating point and thus the fundamental frequency of electric current flowing in the converter, the model is run to produce steady state results. A constant wind is fed to the WT Model and the WT-Electrical Model is run until steady state is reached. There is an initial unsteady period due to the fact that the WT is not run up to speed but rather started, on load. The initial WT speed is a close estimate of the speed at the intended operating point. Once steady state is achieved, the current and voltages for each device for exactly one fundamental cycle are saved. The Power Loss-Thermal Model takes as its inputs these electrical variables from the WT-Electrical Model and so to run the former for say 1 min requires 1 min of steady state input data from the latter. So as to avoid lengthy simulation times, only one cycle of electrical data is saved and this is then looped in the Power Loss-Thermal Model.

To sample exactly one fundamental cycle of data requires the accurate triggering of the subsystem responsible for saving the device voltages and currents. Such triggering, in turn, requires the fundamental frequency of current flowing in both grid and rotor side converters. For the rotor side converter, the rotor current, suitably filtered is used to trigger the data saving; the zero crossing point of the current is used as the triggering instant. The grid side current has a high proportion of noise, most notably at operating points close to synchronous speed, thus the reference voltage used by the controller is used to trigger the grid side data saving.

This electrical data is looped in the Power Loss-Thermal Model simulating the WT operating at a fixed operating point. The power loss is calculated and the temperature of the device determined in the Thermal Model. At this stage there is a feedback loop in which the device temperature is fed to the Power Loss Model where the loss is updated with reference to its dependence on temperature. In separating the electrical and thermal models the feedback mechanism whereby the device temperature modifies the current is severed. A hotter device will suffer greater power loss and this would influence the current flowing in said device. The effect of this upon the WT would be extremely small given that firstly, the sensitivity of this model to this temperature feedback is low and secondly the WT controller itself would operate to maintain a stable operating point.

The WT-Electrical Model is run first producing a data file containing the current and voltages for each device for exactly one fundamental cycle. This data file becomes the starting point for the thermal model, wherein it is looped and input to the power loss model where instantaneous power loss is found. In the power loss model the initial temperatures of the thermal capacitances are initially set at 40°C. The average power loss is calculated and this in turn is fed into a simplified thermal model (with capacitances removed) which allows calculation of the temperatures of the

thermal capacitances. These temperatures are then fed back into the power loss model and the above repeated in a loop four times (which is enough to reach steady state for the initial temperatures of the thermal capacitances). With the initial values now established the full Power Loss-Thermal model can be run.

3.2. Review of parameters for DFIG WT model

Sizing the components within the simulation can be done with reference to previous academic published work, and by some basic understanding of systems involved (e.g. the inductive choke may be sized to reduced harmonic distortion to an acceptable level). Machine electrical parameters are found from previous academic work and can be scaled to suit the size of the machine under study. A review of manufacturers' brochures and product technical information allows a check on sizing of parameters (blade length, gearbox ratios). A full technical specification of any one turbine is unavailable, however, by combining parameters from similar WTs a comprehensive parameterised description of a representative turbine of most sizes can be built up. In this way a model is established that is not based upon any one manufacturer's WT but rather is an amalgamation of several. The design still remains close to most designs of its type and size. Cross-checking parameters with those in real designs is important as for instance, mechanical components like the rotor and gearbox could be sized according to the desired power required at the high speed shaft (this being the product of the blade torque τm and the gear box ratio). In this way various combinations of blade length and gearbox ratios could be selected which give an acceptable high speed shaft torque but may not give realistic speed range of the WT; i.e. there may be multiple sizing criteria for each of the parameters and so confirmation with reference to real parameters prevents values being selected that satisfy most criteria but not all.

3.3. Wind Turbine

The wind turbine modelled is a 2.5MW DFIG. WTs of this size are very common and are currently in production by various manufacturers; some of which are listed in Table 3-1.

Table 3-1 List of manufacturers producing medium sized DFIG WTs.

Manufacturer	Generator size* (MW)	Blade Length (m)	Rotor Diameter (m)	Gearbox ratio
Vestas	2.6	49	100	†
Gamesa	2.5	56	114	†
Gamesa	2.0	47.5	97	1:106.8
Nordex	2.5	†	90/100	†
Alstom	2.7	53.2	100	†
REpower	2 and 3	48.9	100	1:129.6
Sinovel	3	55	113.3	1:114.3
Simulation	*2.5*	*40*	*80*	*1:103*

* maximum generator electric power when operated as DFIG

† denotes, value not specified in manufacturer's literature

The model requires careful selection of parameters to give a representative layout and power rating. The power output from the WT will depend on the rotor diameter, gearbox ratio and also on the c_p-lambda characteristic of the blades. The c_p-lambda expression used is that given in [88] as representative formulisation for a variable speed WT, as is stated in equation 3-1and 3-2.

$$c_p(\lambda_i, \theta) = 0.73\left(\frac{151}{\lambda_i} - 0.58\theta - 0.002\theta^{2.14} - 13.2\right) exp^{\frac{-18.4}{\lambda_i}} \quad 3\text{-}1$$

$$\lambda_i = \left[\left(\frac{1}{\lambda - 0.02\theta}\right) - \left(\frac{-0.003}{\theta^3 + 1}\right)\right]^{-1} \quad 3\text{-}2$$

The power curves for the WT are determined by equation 3-3.

$$P_{wt} = \frac{\rho}{2} A_{wt} c_p(\lambda, \theta) v_w^3 \quad 3\text{-}3$$

The behavioural model for the 2.5MW WT is based upon the above expression for mechanical power produced by the rotor blades of a WT. The WT controller will, of course, attempt to track the maximum value of c_p at all times but the behavioural model nevertheless requires a full calculation of the instantaneous value of c_p from which the mechanical power is determined. The blade length, and gearbox ratio are selected with reference to the standard sizes for a 2.5MW WT, and are tuned so that the electrical power, P_e = 2.5MW.

This simplified model of the rotor blade characteristic does not include features such as the effect of the rotor hub, tower shadow or an incorrect yaw angle as the WT tries to track the wind direction. The behavioural model merely gives a suitable response of the turbine mechanical power as the wind varies with time. This provides sufficient detail for the current study which is concerned mainly with the comparative aging effects upon the two converters. There will be damping in the rotor assembly and drive train which will in any case act to mitigate some of these more detailed aerodynamic and mechanical effects.

The WT gearbox is modelled as a simple ratio; a more detailed mechanical model being considered unnecessary. The effects upon the electrical power flow, of any mechanical inertia from a full model of the gearbox would be felt by both rotor and grid side converters. We can assume that this effect would be similar at both converters and is unlikely to affect any comparison between the converter lifetimes.

3.4. The Electrical Model

The electrical model comprises three main components: the Induction Machine, the power electronic converter and the grid. These are all modelled in PLECS blockset for Simulink. The power grid dynamics are of no concern to the present work and so the grid is modelled as a voltage source.

3.4.1. DFIG Layout

The induction machine and converter together form the doubly fed induction machine (DFIM). The normal operation of an induction machine would require one electrical connection be made to the stator of the machine and this would be the only electrical connection. A doubly fed induction machine requires that a *wound-rotor* induction machine has an electrical connection made to its rotor as well as to its stator. The rotor is connected via a power converter which controls the frequency and magnitude of the voltage fed to it.

The general layout of a DFIG WT is outlined in Figure 3-2.

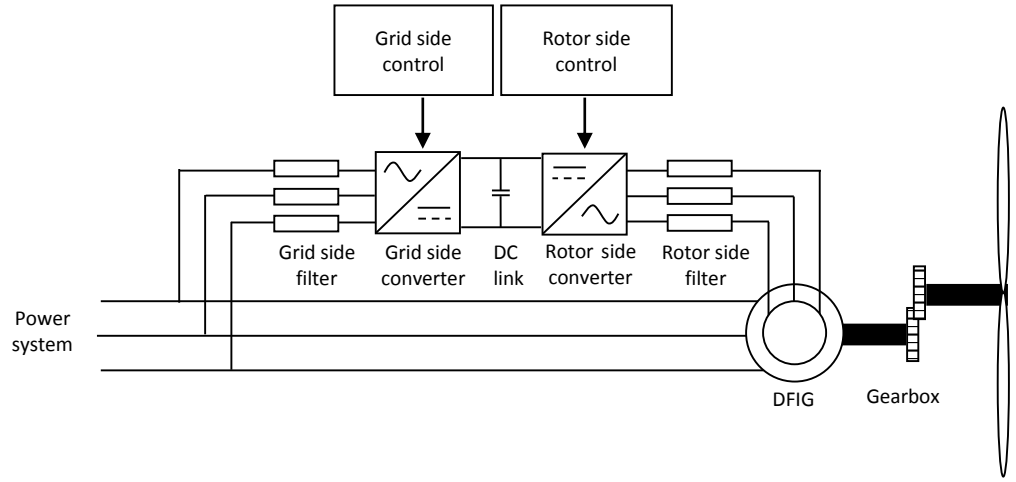

Figure 3-2 Doubly Fed Induction Machine Wind Turbine

3.4.2. Stator-to-Rotor Turns Ratio

The Induction Machines used in doubly fed applications normally have a low stator to rotor turns ratio allowing for lower currents in the rotor circuit and thus in the converter. This, in turn, means that the converter can have a lower rating, thus reducing cost. This transformer action will also have the effect of increasing the voltage on the rotor side. A turns ratio of $\frac{N_s}{N_r} = \frac{1}{3}$ is selected. This gives a maximum rotor voltage which can be estimated from the turns ratio, the maximum slip and the stator voltage.

The estimation requires firstly that the magnetic flux be considered. This has two components: the magnetising flux and the leakage flux. The former will dominate as electric machines are designed to minimize the leakage flux. The stator voltage is chosen to balance the back EMF and the voltage drop across the leakage flux plus the voltage drop across the stator resistance. The drop across $R_s + Z_{ls}$ will be much smaller than E_s and so it may be said that:

$$E_s \approx V_s \tag{3-4}$$

The situation is similar on the rotor side, where again the voltage drop across the resistance and leakage inductance will be small in comparison to the EMF and so

$$E_r^R \approx V_r^R \tag{3-5}$$

The EMFs are related by the turns ratio and the slip

$$E_r^R = \frac{sN_r}{N_s} E_s \qquad 3\text{-}6$$

And so combining 3-4 with 3-5and 3-6, gives

$$V_r^R \approx \frac{sN_r}{N_s} V_s \qquad 3\text{-}7$$

Thus the maximum rotor voltage occurs at the maximum value of slip, giving,

$$V_r^R \approx \frac{s_{max}N_r}{N_s} V_s \approx 0.9V_s \qquad 3\text{-}8$$

In modelling the DFIG all the rotor parameters are referred to the stator side. The rotor and stator variables are related by an *effective turns ratio* that accounts for the geometry of the winding as well as the ratio of their turns. In most cases and more specifically in wind energy applications this effective turns ratio may be approximated by the simple turns ratio [78]; this approach is adopted in the current work. Referred variables are normally denoted by a ', but for simplicity this is omitted and thus all rotor quantities should be read as variables referred to the stator side unless specifically otherwise indicated as real rotor value with an ^{R}.

In modelling the DFIG in Simulink the built-in induction machine block is used. This accepts parameters that are referred to the stator side. There is, however, no means by which the turns ratio can be set internally in this block. The voltage fed to the rotor must also be referred to the stator. This is done by connecting an ideal transformer to the rotor winding with the stator-to-rotor turns ratio, see Figure 3-3.

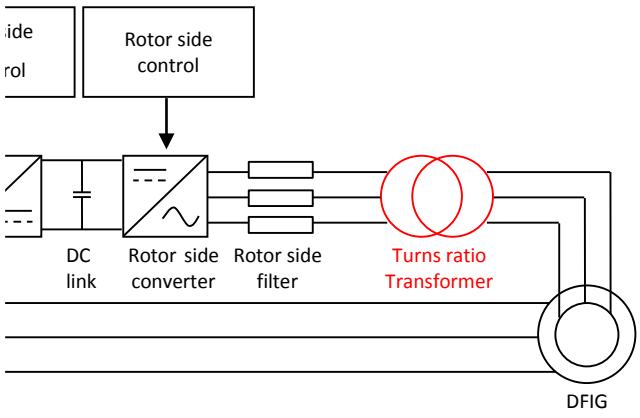

Figure 3-3 Turns Ratio Transformer

3.4.3. The Equivalent Circuit

The induction machine may be idealized by reducing it to two sets of windings, (Figure 3-4). These windings are characterised by a resistance and an impedance. The frequency of current in these two sets of windings is different.

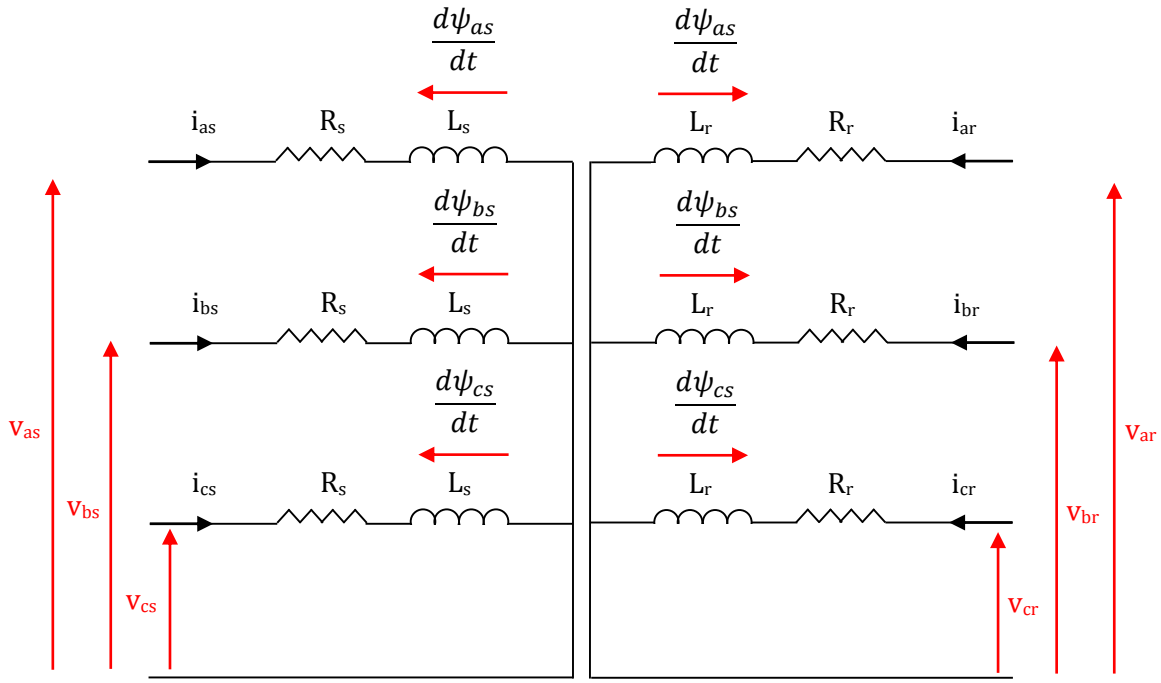

Figure 3-4 DFIG Equivalent Circuit

From this simplified model the following equations may be set up.

$$v_{as}(t) = R_s i_{as}(t) + \frac{d\psi_{as}(t)}{dt} \quad 3\text{-}9$$

$$v_{bs}(t) = R_s i_{bs}(t) + \frac{d\psi_{bs}(t)}{dt} \quad 3\text{-}10$$

$$v_{cs}(t) = R_s i_{cs}(t) + \frac{d\psi_{cs}(t)}{dt} \quad 3\text{-}11$$

$$v_{ar}(t) = R_s i_{ar}(t) + \frac{d\psi_{ar}(t)}{dt} \quad 3\text{-}12$$

$$v_{br}(t) = R_s i_{br}(t) + \frac{d\psi_{br}(t)}{dt} \quad 3\text{-}13$$

$$v_{cr}(t) = R_s i_{cr}(t) + \frac{d\psi_{cr}(t)}{dt} \quad 3\text{-}14$$

The above voltage equations can be considered the instantaneous magnitudes of a rotating space vector. This vector rotates at the system frequency; ω_s for the stator equations and ω_r for the rotor (these are the relevant electrical frequencies of the current flowing in the windings). The three phases, a,b and c are displaced by an electrical angle of 2π/3. In space vector representation the three phase axes are thus similarly spatially displaced. Projecting the phase components by the relevant multiple of 2π/3 (0, 1 and 2 for a, b and c respectively) and adding the results gives the space vector forms of the voltage equations.

Thus

$$v_s^s = \frac{2}{3}v_{as}(t) + v_{bs}(t)\frac{2}{3}e^{j\frac{2\pi}{3}} + v_{cs}(t)\frac{2}{3}e^{j\frac{4\pi}{3}} \quad 3\text{-}15$$

$$v_r^s = \frac{2}{3}v_{ar}(t) + v_{br}(t)\frac{2}{3}e^{j\frac{2\pi}{3}} + v_{cr}(t)\frac{2}{3}e^{j\frac{4\pi}{3}} \quad 3\text{-}16$$

The 2/3 constant is introduced to scale the space vector so that its peak amplitude is equal to the peak amplitude of the of the scalar phase components. Simplifying gives:

$$\underline{v_s^s} = R_s\underline{i_s^s}(t) + \frac{d\underline{\psi_s^s}}{dt} \quad 3\text{-}17$$

$$\underline{v_r^s} = R_r\underline{i_r^s}(t) + \frac{d\underline{\psi_r^s}}{dt} \quad 3\text{-}18$$

The magnetic flux linkage depends not only upon the current in the windings but also on the inductance in which it is flowing. This is split into the magnetising and leakage components.

$$\underline{\psi_s^s} = L_{ls}\underline{i_s^s} + L_m\underline{i_s^s} + L_m\underline{i_r^s} = L_s\underline{i_s^s} + L_m\underline{i_r^s} \quad 3\text{-}19$$

$$\underline{\psi_r^r} = L_{lr}\underline{i_r^r} + L_m\underline{i_r^r} + L_m\underline{i_s^r} = L_r\underline{i_r^r} + L_m\underline{i_s^r} \quad 3\text{-}20$$

Where

$$L_s = L_{ls} + L_m \quad 3\text{-}21$$

$$L_r = L_{lr} + L_m \quad 3\text{-}22$$

Equations 3-17 - 3-21 may be referred to a synchronously rotating frame by multiplying by $e^{-j\theta_m}$ (see [78] for a full explanation of the transformation), giving:

$$\underline{v_s^e} = R_s \underline{i_s^e} + \frac{d\underline{\psi_s^e}}{dt} + j\omega_s \underline{\psi_s^e} \quad 3\text{-}23$$

$$\underline{v_r^e} = R_r \underline{i_r^e} + \frac{d\underline{\psi_r^e}}{dt} + j(\omega_s - \omega_m)\underline{\psi_r^e}$$

$$= R_r \underline{i_r^e} + \frac{d\underline{\psi_r^e}}{dt} + j\omega_r \underline{\psi_r^e} \quad 3\text{-}24$$

$$\underline{\psi_s^e} = L_s \underline{i_s^e} + L_m \underline{i_r^e} \quad 3\text{-}25$$

$$\underline{\psi_r^e} = L_r \underline{i_r^e} + L_m \underline{i_s^e} \quad 3\text{-}26$$

From these equations, the equivalent circuit for a DFIG, in the synchronously rotating reference frame can be constructed, (Figure 3-5). The core losses are accounted for by the inclusion of the resistance (R_m) in the magnetising branch but these being low are normally ignored and indeed Simulink's induction machine block does not include R_m.

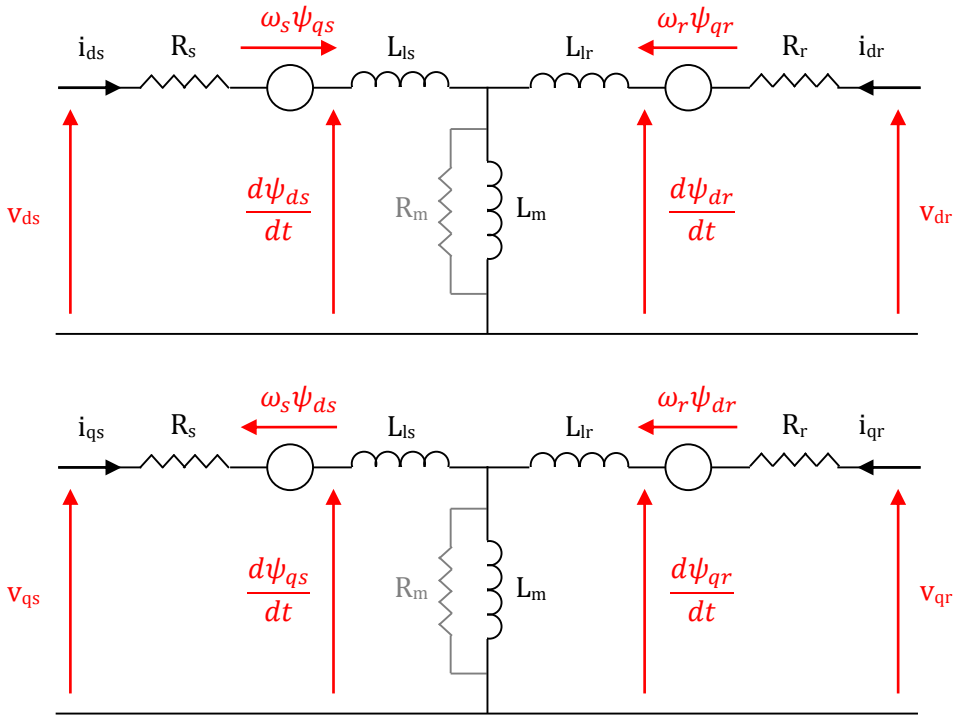

Figure 3-5 Equivalent circuit of DFIG in dq (synchronous) reference frame. R_m included for illustrative purposes only.

3.5. The Control Model

Control of the inverters requires the transformation of electrical parameters into the dq reference frame so that current components may be used to perform independent control of machine

variables such as T_e, P and Q. Such a vector control approach is commonly used in the control of machine drives.

3.5.1. Rotor Side Control Model

Control is achieved with reference to the analogy of DC motor control where the electromagnetic torque is controlled by varying the armature current, with the field current being responsible for maintaining the magnetic field.

$$T_e = K_t \psi_g I_a \quad 3\text{-}27$$

$$T_e = K_t' I_a I_f \quad 3\text{-}28$$

The two currents are decoupled and so the torque is easily controlled by controlling one current. This form of control can be achieved for other machine types, if the electrical variables are projected onto a synchronous reference frame and resolved into orthogonal components. For the time being the rotor leakage inductance is neglected to simplify the explanation. In Figure 3-6 the flux linkage has been aligned along the d-axis. If R_s is assumed zero, it follows then that the stator voltage will be along the q-axis.

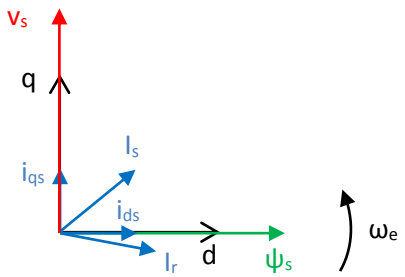

Figure 3-6 Rotor side phasor diagram, for DFIG with generator convention, P_s>0, Q_s>0 and R_s=0

If the current is resolved into d and q components then we see that i_q is the component in phase with v_s and i_d the component out of phase with it. Thus I_q may be used to control the active power and thus the torque

$$P_s = i_{qs} v_s \quad 3\text{-}29$$

$$\tau = \frac{i_{qs} v_s}{\omega_s} \quad 3\text{-}30$$

Likewise I_d can be used to control the reactive power.

$$Q_s = i_{ds} v_s \tag{3-31}$$

In actual fact the stator resistance is non-zero and so the angle between the stator voltage and the stator flux linkage is slightly removed from 90 degrees, (Figure 3-7).

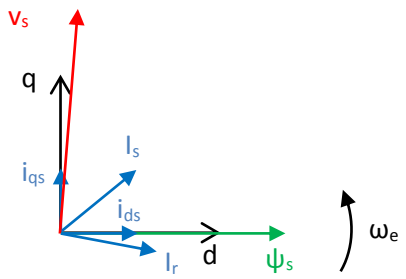

Figure 3-7 Rotor side phasor diagram, for DFIG with generator convention, P_s>0, Q_s>0 and R_s>0

For the power equations it is now necessary to find the d and q components of v_s. And with a non-zero R_s the torque equation no longer holds as the copper losses must be taken into account.

$$P_s = i_{qs} v_{qs} \tag{3-32}$$

$$\tau \approx \frac{i_{qs} v_{qs}}{\omega_s} \tag{3-33}$$

$$Q_s = i_{ds} v_{qs} \tag{3-34}$$

An alternative alignment places the q axis along the stator voltage phasor. These two orientations are known as stator flux alignment and stator voltage alignment (or grid flux orientation, where the grid flux is a virtual flux that induces the grid voltage [89]). Other reference frames for control are possible [80, 90].

Using one of these forms of alignment allows the machine equations to be simplified. Separating equation 3-25 into its orthogonal components and examining Figure 3-7, gives

$$\psi_{ds}^e = L_s i_{ds}^e + L_m i_{dr}^e = \psi_s^e \tag{3-35}$$

$$\psi_{qs}^e = L_s i_{qs}^e + L_m i_{qr}^e = 0 \tag{3-36}$$

Rearranging gives,

$$i_{ds}^e = \frac{\psi_s^e}{L_s} - \frac{L_m i_{dr}^e}{L_s} \tag{3-37}$$

$$i_{qs}^{e} = -\frac{L_m}{L_s} i_{qr}^{e} \quad 3\text{-}38$$

Likewise with the voltage equations

$$v_{ds}^{e} = R_s i_{ds}^{e} + \frac{d\psi_{ds}^{e}}{dt} + j\omega_s \psi_{ds}^{e} \approx 0 \quad 3\text{-}39$$

$$v_{qs}^{e} = R_s \underline{i}_{qs}^{e} + \frac{d\psi_{qs}^{e}}{dt} + j\omega_s \psi_{qs}^{e} = \hat{v}_g \approx \omega_s \psi_s \quad 3\text{-}40$$

By substituting equations 3-39 and 3-40 into 3-32 and 3-34 the power equations may be rewritten

$$P_s \approx -\hat{v}_g \frac{L_m}{L_s} i_{qr}^{e} \quad 3\text{-}41$$

$$Q_s \approx \frac{\hat{v}_g{}^2}{L_s \omega_s} - \hat{v}_g \frac{L_m i_{dr}^{e}}{L_s} \quad 3\text{-}42$$

In controlling the WT the torque is normally used as the control variable. The equation for the electromagnetic torque produced by the DFIG in terms of the machine variables may be derived [79].

$$T_e = \frac{3}{2} p \frac{L_m}{L_s} \left(\psi_{qs} i_{dr} - \psi_{ds} i_{qr} \right) \quad 3\text{-}43$$

$$T_e = \frac{3}{2} p \frac{L_m}{L_s} \frac{\hat{v}_g}{\omega_s} \underline{i}_{qr} \quad 3\text{-}44$$

Re-arranging

$$\underline{i}_{qr} = \frac{2}{3p} \frac{L_s}{L_m} \frac{\omega_s}{\hat{v}_g} T_e \quad 3\text{-}45$$

Equation 3-45 is used to calculate the reference value for i_{qr} from the reference torque. This in turn is set with reference to a predefined MPPT control algorithm.

$$T_{ref} = k\omega_m{}^2 \quad 3\text{-}46$$

The value of k is set by the maximum mechanical power desired from the turbine.

$$k = \frac{P_{max}}{\omega_{max}{}^3} \quad 3\text{-}47$$

The maximum rotational speed for a DFIG is normally set to around 30% above the synchronous speed, see section 3.6.1. In the present work the max speed is set to be exactly 30% above synchronous. Thus, equation 3-47 may be rewritten.

$$k = \frac{P_{max}}{(1.3\omega_s)^3} \qquad 3\text{-}48$$

The control algorithm may now be set based upon just two parameters: the maximum power and the synchronous speed. Figure 3-8 shows the control algorithm for the WT.

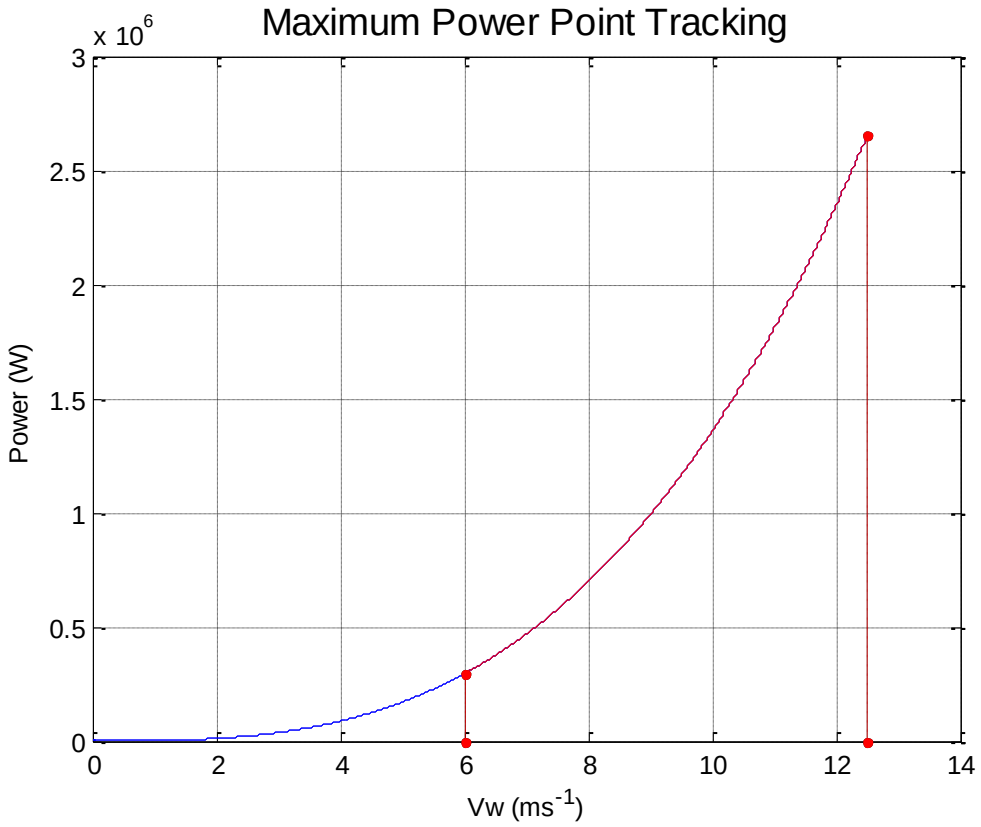

Note red denotes operational speed range as dictated by the converter

Figure 3-8 Power curve for WT at various wind speeds

The mechanical power is shown (Figure 3-8). The maximum power is slightly in excess of the 2.5MW desired as the maximum electrical power, to allow for losses. A mechanical power of 2.63MW is chosen, with an efficiency of 0.957 (due to windage and electrical losses) and a blade length chosen to be a whole number of metres (R=40m) this gives a maximum electrical power of approximately 2.511MW.

Along with the reference value for i_{qr} set by equation 3-45, a current reference for the d-axis component is also needed so that a reference value for i_r can be formed by the summation of the two components. The value of this i_{dr} is set so that the reactive power supplied to the rotor is minimized. The rotor reactive power is found by,

$$Q_r = i_{dr} v_{qr} \tag{3-49}$$

$$i_{dr\_ref} = 0 \Rightarrow Q_{r\_ref} = 0 \tag{3-50}$$

By minimising the rotor reactive power, this allows the converter size to be reduced. As the converter does not have to carry any reactive current, then the semiconductor components can have a lower rating, which ultimately reduces the cost of the converter. The reactive power is thus supplied to the stator, and from equation 3-42,

$$Q_s \approx \frac{\hat{v}_g{}^2}{L_s \omega_s} - \hat{v}_g \frac{L_m i_{dr}^e}{L_s} \tag{3-51}$$

$$i_{dr\_ref} = 0 \Rightarrow Q_s \approx \frac{\hat{v}_g{}^2}{L_s \omega_s} \tag{3-52}$$

The PI Controller

To control the rotor current the machine equations must first be determined. By combining equations 3-25 and 3-26 the following equation for the rotor flux is obtained,

$$\psi_{dr}^e = \left[L_r + \frac{L_m{}^2}{L_r} \right] i_{dr}^e + \frac{\psi_{ds}^e}{L_s} \tag{3-53}$$

$$\psi_{qr}^e = \left[L_r + \frac{L_m{}^2}{L_r} \right] i_{qr}^e + \frac{\psi_{qs}^e}{L_s} = \left[L_r + \frac{L_m{}^2}{L_r} \right] i_{qr}^e \tag{3-54}$$

Combining these with equation 3-24 gives,

$$v_{dr}^e = R_r i_{dr}^e + \sigma L_r \frac{d i_{dr}^e}{dt} + \frac{L_m}{L_s} \frac{d \psi_{ds}^e}{dt} + \omega_r \sigma L_r i_{qr}^e \tag{3-55}$$

$$v_{qr}^e = R_r i_{qr}^e + \sigma L_r \frac{d i_{qr}^e}{dt} + \omega_r \frac{L_m}{L_s} \frac{d \psi_{ds}^e}{dt} + \omega_r \sigma L_r i_{dr}^e \tag{3-56}$$

Some assumptions may be made to simplify the above. Firstly assuming a constant grid voltage implies that the stator flux will be constant, thus

$$\frac{d \psi_{ds}^e}{dt} = 0 \tag{3-57}$$

Also, in steady state conditions,

$$\frac{d i_{dr}^e}{dt} = 0 \tag{3-58}$$

And recalling the equation that relates the grid voltage to the stator flux, equation 3-40, gives

$$v_{dr}^{e} = R_r i_{dr}^{e} + \sigma L_r \frac{di_{dr}^{e}}{dt} - \omega_r \sigma L_r i_{qr}^{e} \quad 3\text{-}59$$

$$v_{qr}^{e} = R_r i_{qr}^{e} + \sigma L_r \frac{di_{qr}^{e}}{dt} + \omega_r \sigma L_r i_{dr}^{e} + \omega_r \frac{L_m}{L_s} \frac{\hat{v}_g}{\omega_s} \quad 3\text{-}60$$

These equations allow the reference voltage components to be calculated which ultimately set the converter output voltage. Figure 3-9 and Figure 3-10 show the control schemes for the rotor side controller.

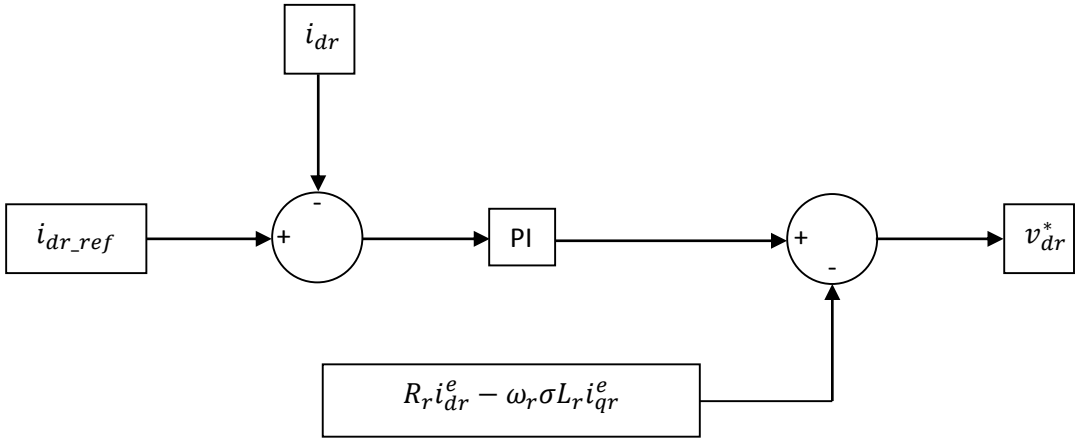

Figure 3-9 Rotor side d-axis controller

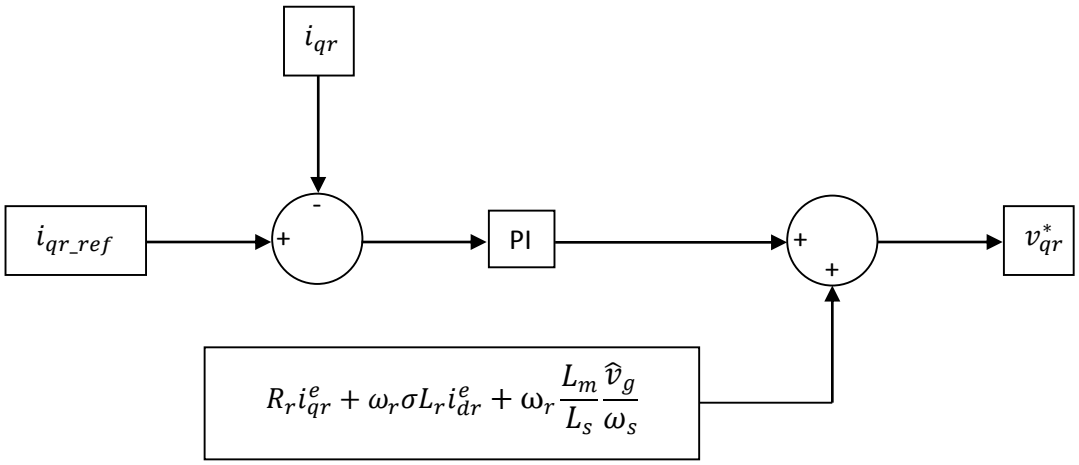

Figure 3-10 Rotor side q-axis controller

The current components are controlled using a PI controller with the cross coupling and rotor current terms fed forward. The dq components of v_r are transformed back to the phase voltages,

v_{ar}, v_{br}, v_{cr}. This requires knowledge of the stator flux angle and rotor angle. The former may be determined by integrating the back emf, the latter from the mechanical rotor speed. Figure 11 shows the phasor diagram for the DFIG, with the angles relevant to the transformation shown.

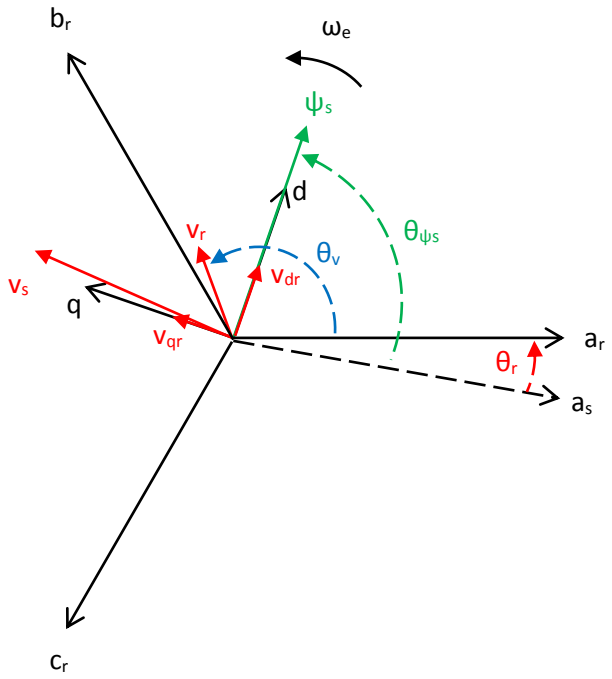

Figure 3-11 Phasor diagram for rotor side variables

$$v_{ar} = v_{dr}\cos(\theta_{\psi_s} - \theta_r) + v_{qr}\cos\left(\frac{\pi}{2} + \theta_{\psi_s} - \theta_r\right) \quad 3\text{-}61$$

$$v_{br} = v_{dr}\cos\left(\theta_{\psi_s} - \theta_r - \frac{2\pi}{3}\right) + v_{qr}\cos\left(\frac{\pi}{2} + \theta_{\psi_s} - \theta_r - \frac{2\pi}{3}\right) \quad 3\text{-}62$$

$$v_{cr} = v_{dr}\cos\left(\theta_{\psi_s} - \theta_r - \frac{4\pi}{3}\right) + v_{qr}\cos\left(\frac{\pi}{2} + \theta_{\psi_s} - \theta_r - \frac{4\pi}{3}\right) \quad 3\text{-}63$$

The transformation is achieved via equations 3-61-3-63. The resulting v_r is fed as reference to the rotor side converter.

3.5.2. Grid Side Control Model

The function of the grid-side controller is to maintain the dc link voltage at a set value. The grid side control variables are also transformed into a dq frame in a similar way to the rotor variables. This time the d-axis is aligned with the supply voltage, i.e. the state voltage. Figure 3-12 shows the stator voltage alignment commonly used in grid side converter control.

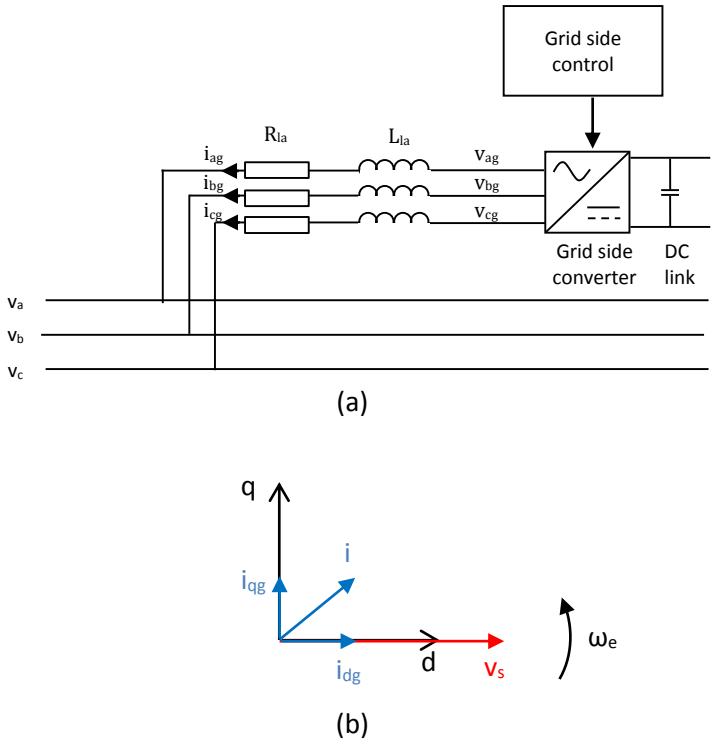

Figure 3-12 (a) Grid side controller layout and (b) grid side phasor diagram, for DFIG with generator convention.

The line voltage may be expressed as follows.

$$\underline{v_a} = R_l \underline{i_{ag}} + L_l \frac{d\underline{i_{ag}}}{dt} + \underline{v_{ag}} \tag{3-64}$$

Transforming to the dq reference frame gives.

$$v_d^e = R_l i_{dg}^e + L_l \frac{di_{dg}^e}{dt} - \omega_r \sigma L_r i_{qr}^e + v_{dg}^e \tag{3-65}$$

$$v_q^e = R_l i_{qg}^e + L_l \frac{di_{qg}^e}{dt} + \omega_r \sigma L_r i_{dr}^e + v_{qg}^e \tag{3-66}$$

The power equations are again found by the product of the voltage and current components in and out of phase for real and reactive power respectively.

$$P_{gsc} = v_{dg}^e i_{dg}^e + v_{qg}^e i_{qg}^e \tag{3-67}$$

$$Q_{gsc} = v_{dg}^e i_{qg}^e + v_{qg}^e i_{dg}^e \tag{3-68}$$

As a consequence of the stator voltage alignment v_{qs}=0 thus the second term in the real power equation is zero. Equating the power received by the grid from the converter to the power at the dc link, the following equation is obtained.

$$v_{dc} i_{os} = 3 v_{dg} i_{dg} \quad 3\text{-}69$$

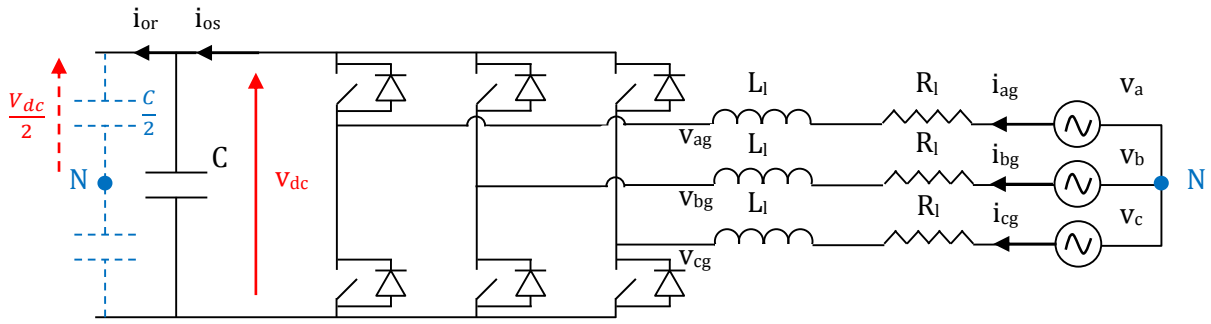

Figure 3-13 Standard Grid side converter and grid connection

By inspection of Figure 3-13 and neglecting the voltage drop across the line impedance and losses in the converter it may be shown that,

$$v_a = \frac{\hat{v}_a}{\sqrt{2}} = \frac{v_{dc}}{2\sqrt{2}} \quad 3\text{-}70$$

And as v_d is scaled to have the same peak value as v_a and taking account of the modulation index, m,

$$v_{dg} = \frac{v_{dc} m}{2\sqrt{2}} \quad 3\text{-}71$$

Combining equations and 3-69 and 3-71 and gives,

$$i_{os} = \frac{3}{2\sqrt{2}} m i_{dg} \quad 3\text{-}72$$

Finally the charge on the dc-link capacitor is,

$$C_{dc} V_{dc} = (i_{os} - i_{or}) t \quad 3\text{-}73$$

$$\frac{dV_{dc}}{dx} = \frac{3}{2\sqrt{2} C_{dc}} m i_{dg} - \frac{i_{or}}{C_{dc}} \quad 3\text{-}74$$

Thus the dc-link voltage may be controlled by i_{dg}, i.e. in response to changes in the rotor power, which causes the dc-link voltage to rise and fall.

From equation 3-68 and recalling that v_q=0 it is clear that,

$$Q_{gsc} = v_{dg}^e i_{qg}^e \quad 3\text{-}75$$

Recalling 3-71 gives,

$$Q_{gsc} = \frac{v_{dc} m}{2\sqrt{2}} i_{qg}^{e} \qquad 3\text{-}76$$

Thus the reactive power output from the grid side converter may be controlled by controlling i_{qg}. The reference for the q-axis current is set to zero as the reactive power from the converter is minimised.

The PI Controller

Figure 3-14 and Figure 3-15 show control schemes for the grid side controller. The dc-link reference voltage is 1400V. The reference for the d-axis current is set via a PI controller from the error in the dc-link voltage. With the addition of the feed forward terms, v_{dg} is determined.

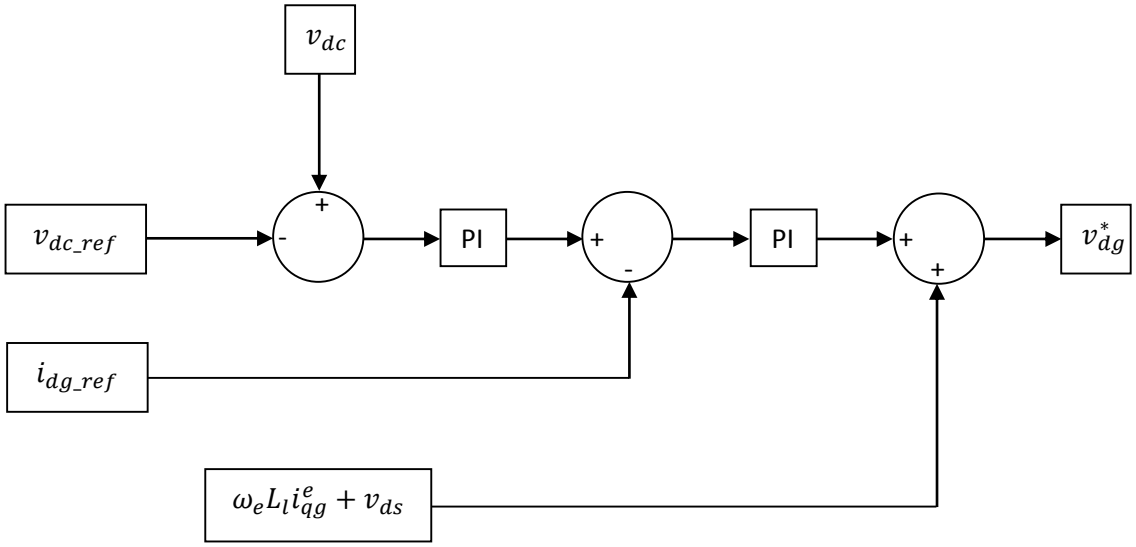

Figure 3-14 Grid side d-axis controller

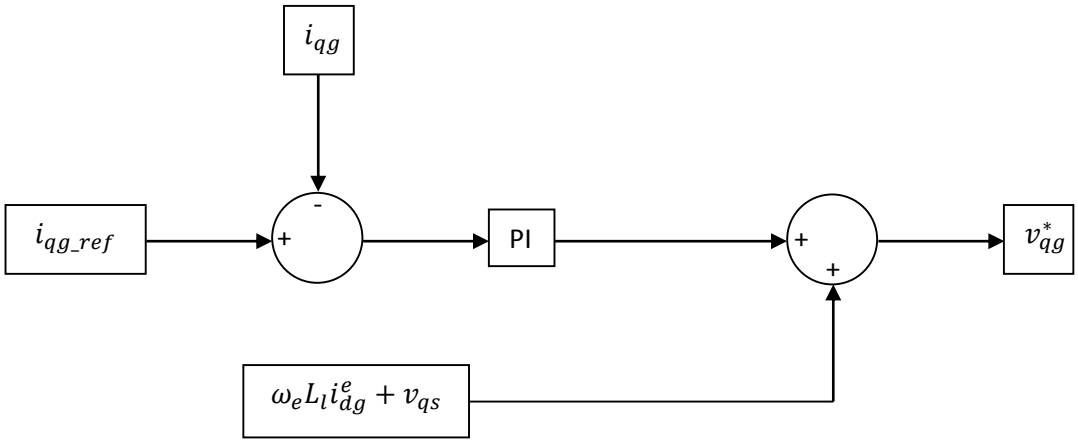

Figure 3-15 Grid side q-axis controller

The dq components of v_g are transformed back to the phase voltages, v_{ag}, v_{bg}, v_{cg}. This requires knowledge of the stator voltage angle, which is easily determined from the stator phase voltages. Figure 3-16 shows the phasor diagram for the DFIG, with the angles relevant to the transformation shown.

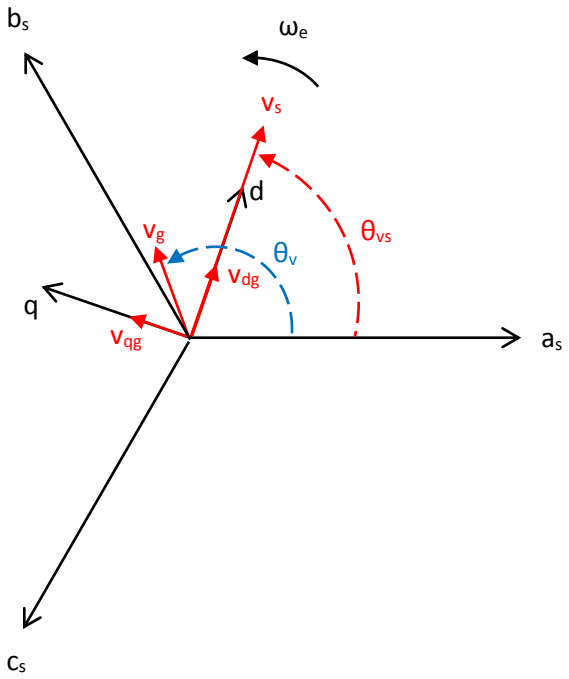

Figure 3-16 Phasor diagram for grid side variables

$$v_{ag} = v_{dg}\cos(\theta_{vg} - \theta_{vs}) + v_{qg}\cos\left(\frac{\pi}{2} + \theta_{vg} - \theta_{vs}\right) \quad 3\text{-}77$$

$$v_{bg} = v_{dg}\cos\left(\theta_{vg} - \theta_{vs} - \frac{2\pi}{3}\right) + v_{qg}\cos\left(\frac{\pi}{2} + \theta_{vg} - \theta_{vs} - \frac{2\pi}{3}\right) \quad 3\text{-}78$$

$$v_{cg} = v_{dg}\cos\left(\theta_{vg} - \theta_{vs} - \frac{4\pi}{3}\right) + v_{qg}\cos\left(\frac{\pi}{2} + \theta_{vg} - \theta_{vs} - \frac{4\pi}{3}\right) \quad 3\text{-}79$$

The transformation is achieved via equations 3-77-3-79. The resulting v_g is fed as reference to the grid side converter.

3.6. The Converter

The converter is modelled using PLECS blockset within Simulink. The converter architecture and device characteristics are based upon one of Semikron's, SKiiP 3 power converters. The SKiiP 2013 GB172-4DL V3 [91] (see Appendix) is a 2-pack integrated intelligent power systems, with suitable voltage, current and power ratings for the present work. The converter is composed of four modules each comprising an upper and lower IGBT-diode pair. The modules are connected in parallel, so that a higher rating of the overall device may be achieved using lower rated constituents. This results in a single phase converter, made up of 16 semiconductor components: eight IGBTS and eight diodes. Three of these converters are modelled, one for each phase.

The gating signals for each of the IGBTS are synthesised by scaling the reference voltages by half the dc-link voltage and comparing to a triangle wave with a frequency equal to the desired switching frequency and with unity amplitude. The switching frequency is chosen to be 2.5kHz. Figure 3-17 shows the layout of the grid-side and rotor-side converter assembly, or back-to-back converter.

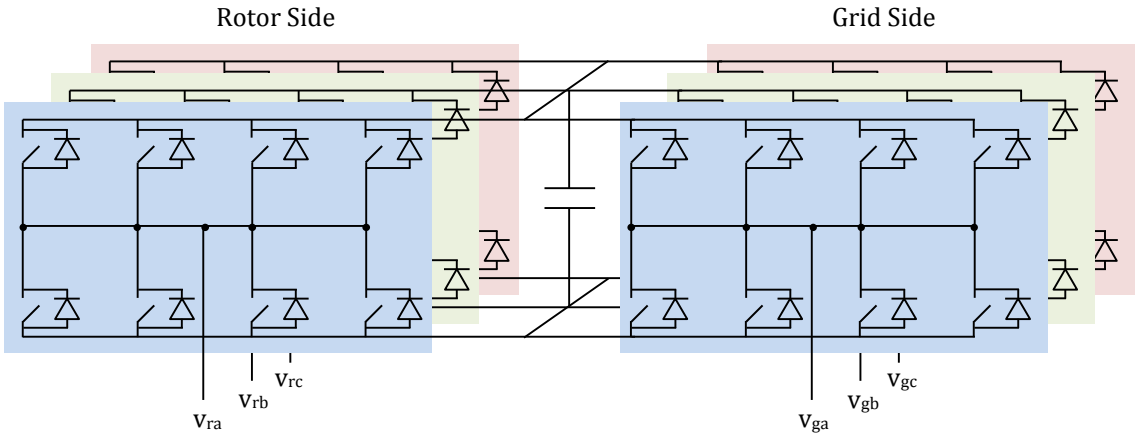

Figure 3-17 Back-to-back converter

The 4 half bridges act identically and could be represented by one larger half bridge. The converter is, however, modelled in its entirety to give opportunity for greater detail in the thermal model. Though, for example, the top row of devices will dissipate the same amount of heat, the temperatures resulting within the converter will depend also upon the architecture of the half bridges and how they are positioned on the heat sink together with the thermal characteristics of the materials. The dc link capacitance is modelled as a single lumped capacitance as there is no advantage to be gained in modelling the individual racks of capacitors that each converter would have.

3.6.1. Speed Range

The converter operates ultimately to control the speed, as mentioned above. The speed range must be set so that the operating frequency range of the rotor side converter is known; the grid side converter will operate at the grid frequency. The speed range of DFIG WTs varies but is generally close to the ± 30% of the synchronous speed. The speed range is limited by the power rating of the converter. Figure 3-18 shows the rotor power plotted against the wind speed; the power is zero at synchronous speed and positive (to the rotor) and negative (from the rotor) above and below this respectively.

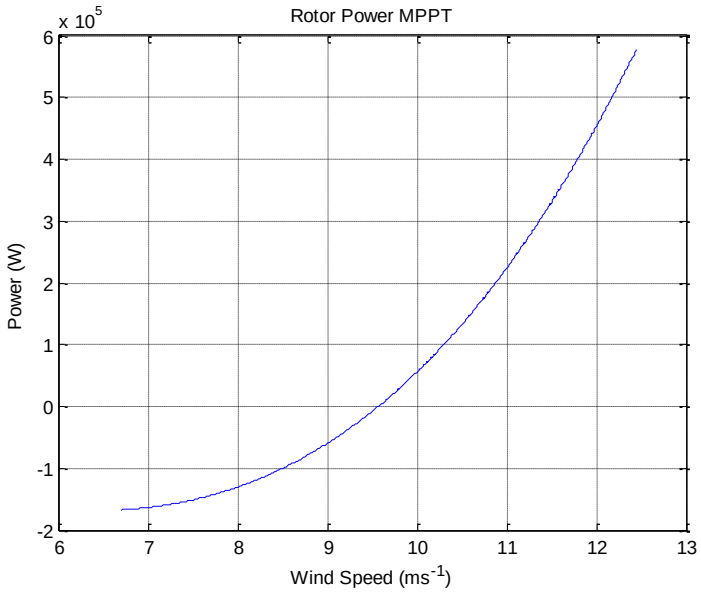

Figure 3-18 Rotor Power vs Wind Speed

At both supersynchronous and subsynchronous speeds both converters will carry real power from or to the rotor respectively. The rotor will carry less power at a slip of 0.3 (subsynchronous) than at

-0.3 (supersynchronous) and often the subsynchronous frequency range will therefore be greater than the supersynchronous range. However, for the current work the frequency range is symmetrical about synchronous speed as the phenomena under investigation are frequency related and examination of these may require analysis at similar values positive and negative slip.

3.7. Power Loss Model

For the power loss model, a review of academic literature and manufacturers' datasheets was required. Parameters for a detailed power loss model are difficult to find and often unavailable. Some loss parameters are scaled with reference to current, voltage or temperature or all three; the relationship as to how these losses scale is given in the form of 2D plots (often two plots on the same axes, one at max Tj and one at Tj=25°C); linear interpolation is assumed to determine loss parameters at temperatures between these two.

This is the case for conduction loss. Switching loss temperature dependency information is often not included in the datasheets. Manufacturers give an approximating formula that accounts for the temperature dependency.

For steady state tests one fundamental cycle of electrical data is saved upon completion of the Electrical Simulation. This can then be looped in the Power Loss Model and used to generate the loss data. By doing this the electrical data saved is limited. Dynamic tests, however, require a longer period of electrical data to be sampled.

The Power Loss-Thermal Model, thus, takes as inputs the IGBT and diode current as well as the rotor and grid phase current and the dc-link voltage. The manufacturer's datasheet gives power loss values at set currents, voltages and temperatures. The Power Loss Model determines the loss from each device by scaling the relevant datasheet loss parameter by the device voltage and current.

The two mechanisms by which power is lost as heat from the semiconductor devices are known as the conduction losses and switching losses.

3.7.2. Conduction Loss

IGBT

Determination of the IGBT condition loss requires knowledge of the IGBT collector-emitter voltage.

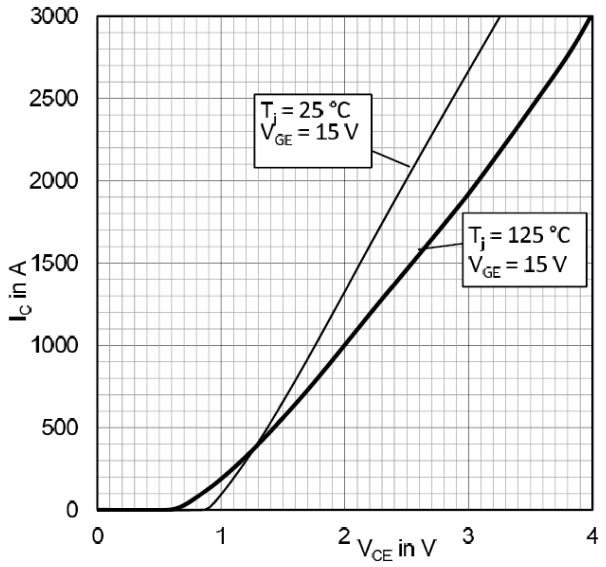

Figure 3-19 Datasheet IGBT output characteristic [91]

The datasheet gives a graphical representation of the current dependency of the v_{ce} and an indication of the temperature dependency by showing plots at 25°C and 125°C, (Figure 3-19). If the device current is known at either of the plotted temperatures then the v_{ce} may be trivially extracted from the plotted relationship. The temperature must also be accounted for in the determination of v_{ce}.

$$v_{ce}(i_c, T) = v_{ce0}(i_c, T) + i_c r_{ce}(i_c, T) \qquad 3\text{-}80$$

The plots were used to create a function for v_{ce} in terms of i_c and T (3-80). The value of the x-axis intercept (v_{ce0} collector-emitter threshold voltage) is found by linear interpolation between the 2 plotted values and the gradient (r_{ce} on-state bulk resistance) is similarly found by interpolating the gradient between those plotted.

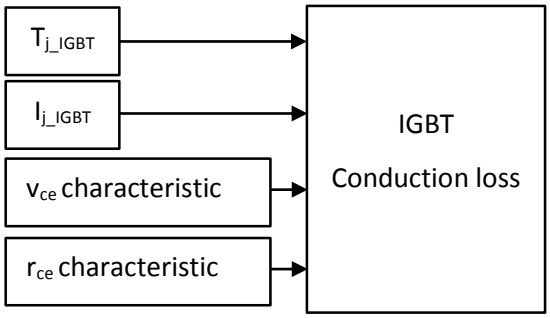

Figure 3-20 Block diagram for IGBT Conduction Loss calculation

The conduction loss is then determined by multiplying v_{ce} by the device current, thus giving the power loss from a single device at each calculation step in the simulation (3-81). The block diagram for the conduction loss calculation is show in Figure 3-20

$$P_{loss\ conduction} = i_c v_{ce} \tag{3-81}$$

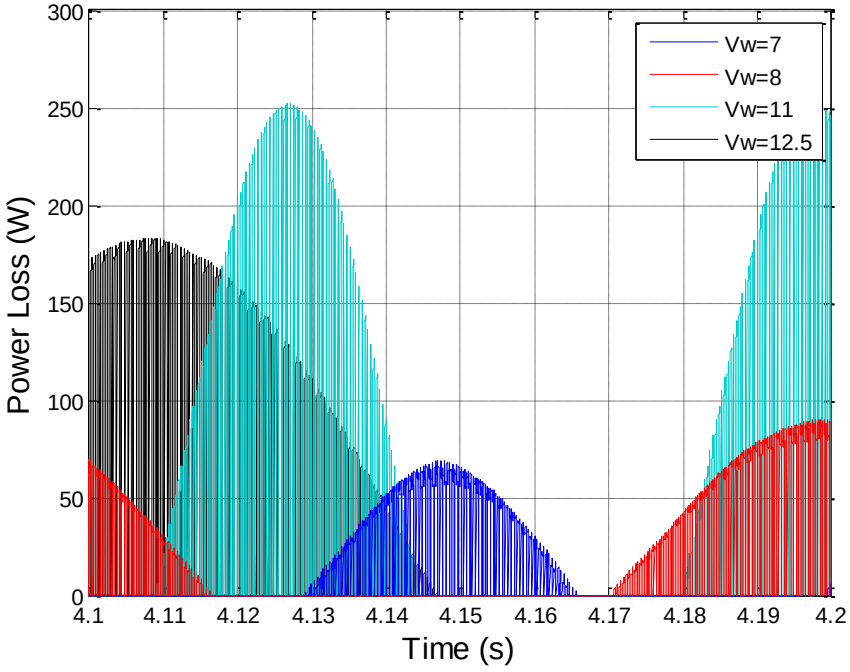

Figure 3-21 Rotor side IGBT conduction losses

The device conduction loss as shown in Figure 3-21 takes the form of pulses at the switching frequency modulated by the fundamental rotor frequency. The device junction temperature, as calculated in the Thermal Model (downstream from the Power Loss Model), is fed back to the conduction loss model so that as well as being scaled by the current flowing in the device the loss is also continually updated by the temperature.

Diode

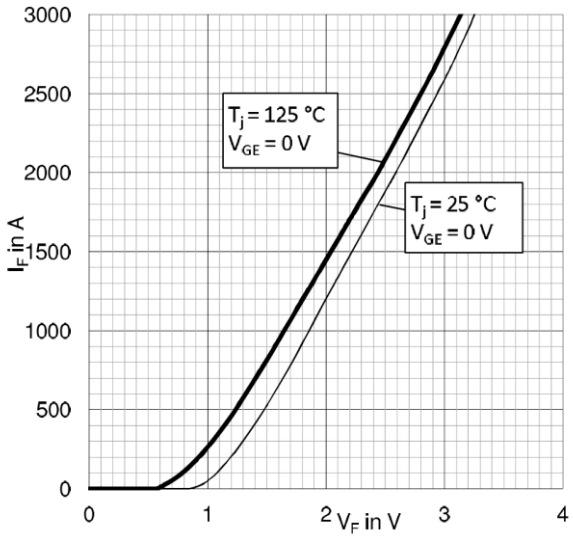

Figure 3-22 Datasheet diode output characteristic [91]

The conduction loss for the diode is found in the same way using the datasheet plot of the forward current, i_f, against the forward voltage, v_f (Figure 3-22).

$$v_f(i_f, T) = v_{f0}(i_c, T) + i_f r_f(i_f, T) \quad 3\text{-}82$$

$$P_{loss\ conduction} = i_f v_f \quad 3\text{-}83$$

The forward voltage is calculated as per equation 3-81 and the switching power loss determined using equation 3-83.

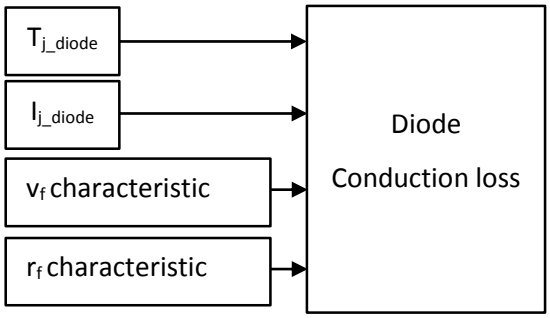

Figure 3-23 Block diagram for Diode Conduction Loss calculation

The block diagram for the conduction loss calculation is show in Figure 3 23.

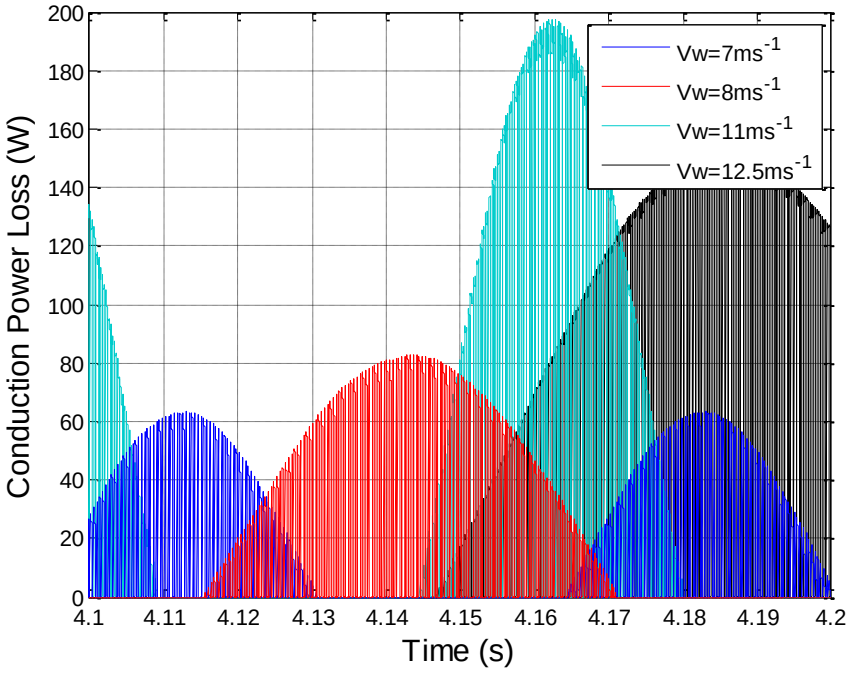

Figure 3-24 Rotor side diode conduction losses

The resulting device losses at different wind speeds are show in Figure 3-24.

3.7.3. Switching Loss

During the switching of any device the current will rise/fall as the voltage falls/rises thus there will be a short but finite period when energy is lost. In PLECS the switches are modelled as ideal switches. The switching loss is found by scaling the datasheet loss parameter by the device current

and voltage. To accurately model the switching losses the power loss (E_{on+off} for the IGBT and E_{rr} for the diode) would need to be present for a very short time (a few hundred ns). This would result in very long simulation times. Instead the switching loss energy is spread across the time period between switching instances. This loss in fidelity may be permitted as the cost to the precision of the device temperature will be minimal. As the thermal time constant is much larger, whether the switching loss pulse time length is the order of a few hundred nanoseconds or a few hundred microseconds will not affect the temperature cycling to any noticeable degree which will be at most approximately 15Hz.

$$P_{sw\_IGBT}\left(T_j\right) = P_{sw\_T_{ref}}\left(1 + TC_{Esw}\left(T_j - T_{ref}\right)\right) \quad 3\text{-}84$$

$$P_{sw\_diode}\left(T_j\right) = P_{sw\_T_{ref}}\left(1 + TC_{Err}\left(T_j - T_{ref}\right)\right) \quad 3\text{-}85$$

The temperature dependency of the switching loss is accounted for by inclusion of a temperature correction factor in the loss calculation, which is taken from [92]. The value of E_{on+off} and E_{rr} are given at a specified temperature (T_{ref}) this value is modified as per equations 3-84 and 3-85 to give the temperature dependant value of device switching loss.

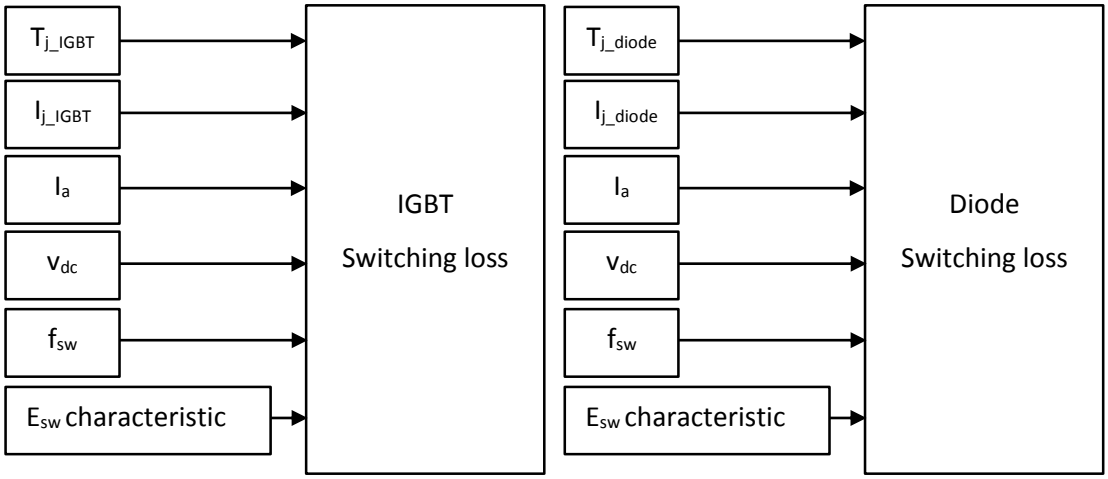

Figure 3-25 Block diagram for IGBT and Diode Switching Loss calculation

The block diagram for the conduction loss calculation is show in Figure 3-25.

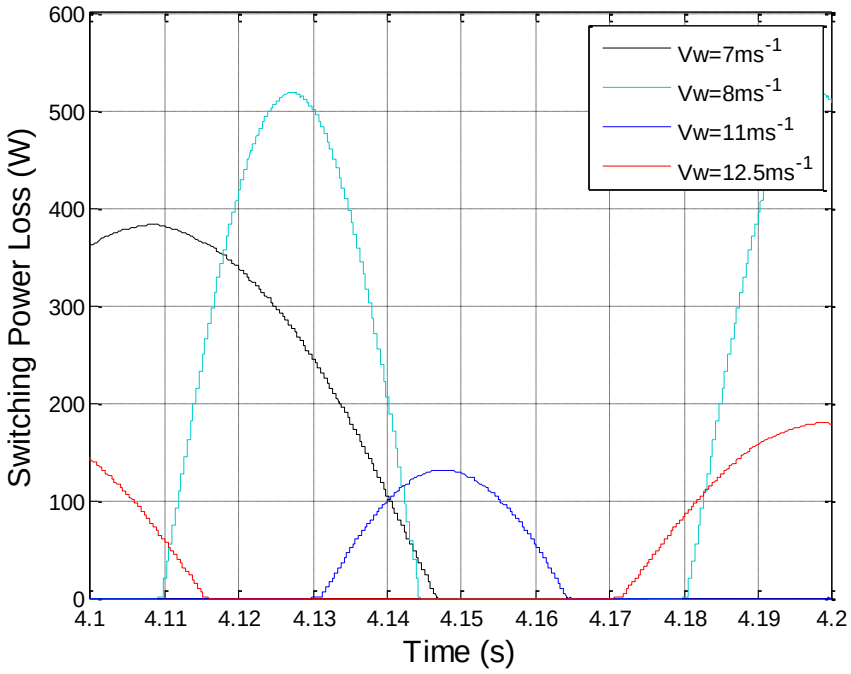

Figure 3-26 Rotor side IGBT switching losses

The device switching losses would in fact be narrow pulses, though, due to the simplification mentioned above appear as a continual loss modulated by the fundamental frequency of the device current (Figure 3-26).

3.7.4. Other Mechanisms of Temperature Feedback

We have T dependency in the loss model but no feedback to the actual current flowing in the converter. The actual current flowing would affect the WT so would have other effects not taken into account by merely scaling the loss to reflect.

As outlined above the device power losses are updated by temperature feedback. This provides an important level of detail, in that the losses will change in response to the changing temperature at the junction. The junction temperature will also affect the current flowing in the device and thus the operating point of the WT. The significance of this mechanism was felt to be too small to merit inclusion. Any change to the operating point would be extremely small given the likely magnitude of any current change due to a temperature swing, and the damping supplied by the drive train and rotor inertia would render it negligible.

3.8. Thermal Model

The thermal model is constructed with reference to the thermal parameters from the datasheet. These specify junction-to-reference (j-r) and reference-to-ambient (r-a) thermal impedances. The reference point is the position on the module at which a thermocouple is attached for temperature monitoring purposes. This is positioned somewhere on the casing of the device. The thermal parameters are given as thermal resistances and time constants which may be used to build up a Foster type thermal network model. Datasheet thermal parameters appear in Foster form as they are extracted easily from the thermal impedance characteristic plot. The Foster parameters are converted to Cauer type parameters, which have physical meaning and allow a network to be built by cascading sections of the complete junction-to-ambient thermal model

Within each of the converter's half bridges there are the thermal paths for two IGBTs and two diodes. These meet at the interface between the casing and heat sink. There will be some heat transfer between the adjacent devices within the half bridge via the module casing and this is allowed for in the model by joining the thermal circuit for the 4 devices per half bridge at the heat sink.

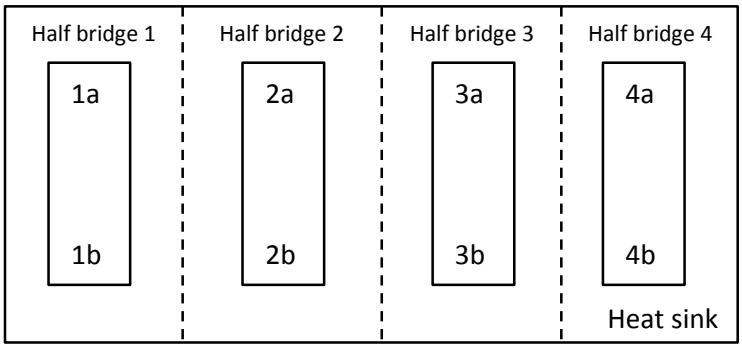

Figure 3-27 Converter layout

Further, each half bridge is thermally connected to the adjacent bridges via the heat sink, see Figure 3-27. The flow of heat between the half bridges is driven by the difference in temperature between them. As each half bridge carries an identical electrical current then there should be little or no temperature differential between them. The heat flow between upper and lower IGBT-diode pairs on the same half bridge is accounted for as mentioned above, however there will be a temperature differential between upper and lower device pairs on adjacent half bridges. The thermal path between such pairs is via the heat sink from where there is an extremely low resistance path to the

ambient. Clearly this path will dominate the dissipation of heat and for this reason the half bridge to half bridge heat transfer is neglected in the model.

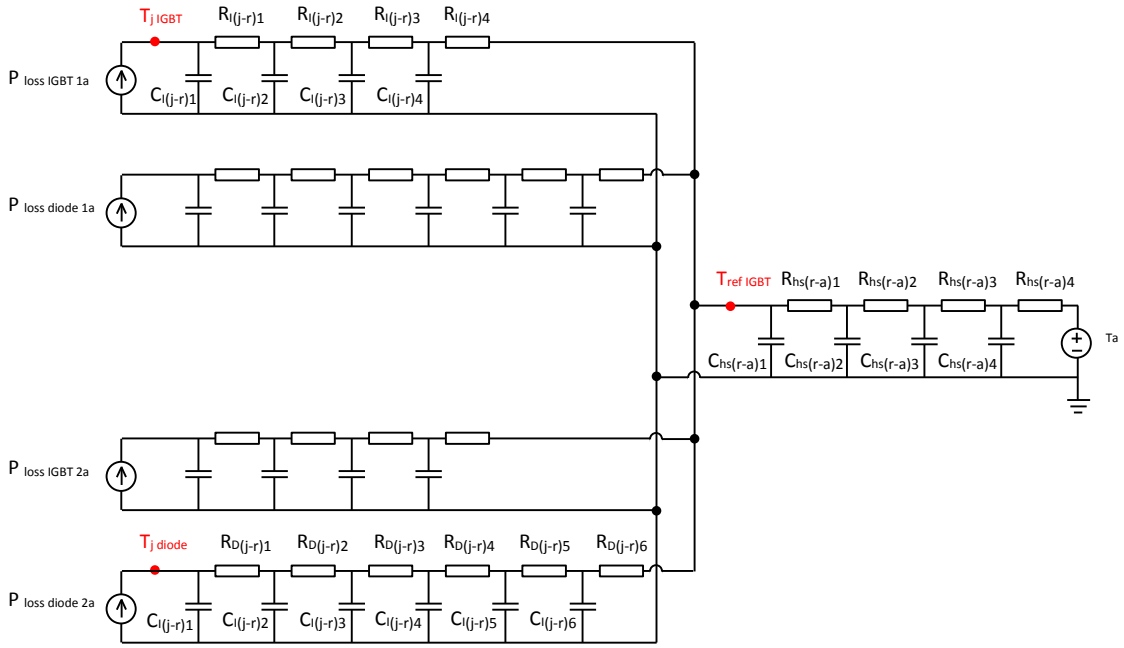

Figure 3-28 Thermal network model for one half bridge of the converter

This simplifies the thermal circuit as it may now be represented by dividing the heat sink into four and modelling just one of the half bridges, (Figure 3-28). This approach is verified experimentally by use of an inverter test rig, see Chapter 4.

Of course there are three single phase converters in both rotor and grid side converters though these are not thermally connected. Only one single phase converter need be included in the thermal model as the only difference between the three phases in terms of their temperature characteristic will be the phase difference, which will have no effect on the converter lifetime.

3.9. Steady state tests

There are two possible means by which temperature cycling can occur within the power electronic converter. In both, power loss variation causes the junction temperature to vary. Firstly, variation in the loss arises by virtue of the fact that the power itself is oscillating as a result of the ac current flowing. And secondly, variation in the wind will cause power variation.

Dynamic loading on the electrical system arises when the WT rotor responds to a change in the wind intensity or direction. Such wind variation occurs at a range of frequencies governed by multiple factors but is likely to include the turbulent, diurnal and synoptic components of the Van der Hoven spectrum (0, Figure 1-2). The impact of some of these variations will be somewhat mitigated by damping in the rotor and dive train.

The thermal cycling that can be attributed to ac power loss cycling will occur in both converters at all operating points save for at the synchronous speed. At this operating point the power flow across the back to back converter system is zero. P_r and P_{gsc} are thus zero. Q_r and Q_{gsc} are controlled at all times to be zero. Thus at synchronous speed the power in both converters should be zero. However, power loss is still present as there is current flowing.

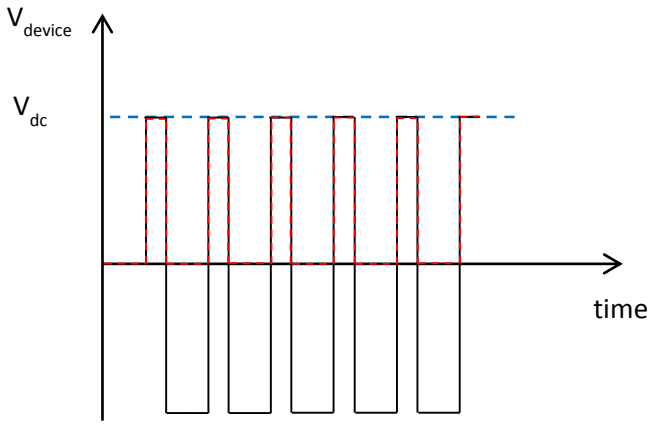

Red: device voltage, Black: Line to line output voltage

Figure 3-29 Output voltage from converter and device voltage

The real power is zero as the fundamental component of the voltage, v_{r_fund} is zero, however the instantaneous voltage switches from $\pm v_{dc}$ to 0 with a duty cycle dependant on the magnitude of the dc voltage, see Figure 3-29. This means that the device junction still acts as a source of power loss at synchronous speed, even though P_r=0.

Thus there is power loss at all operating points and this loss is related to the total power flowing in the converter and also its frequency. Each operating point will have a different effect on the lifetime of the converter. In order to examine the effect upon converter lifetime that the various regions of the operating curve have, it is necessary to run steady state tests.

3.10.Initial Temperature of C_{th}

The thermal simulation may take considerable time to reach steady state. The simulation's progress toward steady state may be expedited if the temperature of the thermal capacitances is initially set to a value close to that which will be reached at steady state. The thermal time constant is larger than the mechanical or electrical time constants and so this will be the main factor in the time taken to reach steady state. Further as the electrical and thermal components of the simulation are separate (the models are run consecutively) electrical and mechanical steady state are already assumed as the starting point for the thermal simulation. The electrical model is run for a time period of 40s which is long enough for steady state to be achieved for all but the run of the simulation at $Vw=9.755ms^{-1}$ which corresponded to a frequency of 0.0373Hz.This required approximately 80s.

If the initial value of the thermal capacitances can be set close to their values at steady state then steady state will be achieved more quickly.

Two factors contribute to the time constant of the thermal model; the thermal capacitances present in the model and the dependency of the power loss on temperature. Before steady state can be deemed to have been achieved both of these must have settled to steady values. The power loss in fact reaches a quasi-steady state containing an average and oscillatory component; the average value reaches a constant value whilst the oscillatory component's amplitude will also reach an unchanging value.

The method chosen to determine the initial C_{th} temperatures ($C_{th\_initial\_temp}$) involves an iterative approach in which

Step 1: the thermal model is run without the heat sink thermal capacitance

Step 2: the average power loss for each device is calculated

Step 3: the average power loss is fed into thermal model with all the C_{th} removed from both device and heat sink circuits

Removing the heat sink C_{th} in step 1 reduces the time constant of the system and so the response of the power loss to the change in junction temperature is quicker. This allows the power loss to approach steady state more swiftly. The average power loss is then determined by integrating the power loss for each device over one cycle and averaging over time. This is fed into the thermal model in step 3 which has all the C_{th} removed. Determining the temperatures at the nodes between the R_{th} gives the values for each of the $C_{th\_initial\_temp}$ in the circuit. These $C_{th\_initial\_temp}$ values are then

input into the thermal model in step 1 and the process repeated. This iterative approach allows the $C_{th\_initial\_temp}$ values at steady state to be determined without the need to run the full simulation for an extended period.

This process of setting these initial parameters using the steady state average power loss value allows the mean temperature component of the quasi steady state to be established. The temperature quasi steady state also includes an oscillating component. These temperature oscillations do not take much time to reach steady state so the full model only needs to run for 2-3s to reach the full thermal quasi-steady state for most of the runs with the exception of the runs closest to synchronous speed which require 30-40s. Indeed the main factor determining the simulation time for the full thermal simulation is the frequency of the temperature cycling (which in the steady state tests is directly related to the wind speed). The lower the frequency the longer the time required to simulated one complete cycle of the temperature oscillation; and several cycles are needed to ensure we have a stable temperature oscillation. With the initial temperatures of the thermal capacitances established and the full thermal model ran, the temperatures of the IGBTs and diodes are available with which to determine the device lifetimes.

3.11.Lifetime calculation

Once the temperature profile of the device is determined the effect on lifetime of a particular operating point can be calculated. This is done by reference to an empirical relationship derived in [52]. This relationship was derived from a study of older but similar devices to those under consideration in the present work.

Lifetime modelling uses empirical formulisation based on experimental data. Any empirical formula is likely to reflect the characteristics of the specific device(s) used in the particular study from which the formula was derived. The study may also outline limitations which restrict the extent to which the formula may be applied with confidence: for example the LESIT results outlined in [26] were not validated for temperature swings of magnitude less than 30K. By examining multiple lifetime formula, however, some confidence may be gained as to the general aging trend obeyed by devices of the type in question.

Semiconductor device technology is evolving all the time and new packaging or device architecture is likely to have lifetime impacts. It is useful thus to perform some calibration of the lifetime model with regard to some known device lifetime expectation, of the device in question. In so doing some confidence may be obtained that the predictions made by the lifetime model across the board are

of the correct scale, for the device type at hand. However, as the current work is primarily involved in a comparative assessment of the grid and rotor side converter device lifetimes this was deemed not necessary, and left as an option for future work.

Equations 3-86 and 3-87 give the number of cycles to failure (N_f) and the device lifetime, respectively.

$$N_f = A\Delta T_j^{\alpha} e^{\left(\frac{Q}{RT_m}\right)} \quad 3\text{-}86$$

Where: A=640, α=-5, Q=7.8x10^4 J.mol^{-1}, R=8.314 J.mol^{-1}K^{-1}

$$lifetime = \frac{N_f}{freq_{T_j} \times 365 \times 24 \times 3600} \quad 3\text{-}87$$

3.12.Summary

This chapter has outlined the make-up of the Simulink/PLECS model of a 2.5MW DFIG. The model is split into three main parts: the WT-Electrical Model, the Power Loss-Thermal Model and the Lifetime calculation. A behavioural model of the WT rotor is coupled to a full electrical model of the DFIG and its converter. The electrical results from running this model are then fed as input to the Power Loss model where device losses are determined by scaling datasheet power loss parameters, with respect to instantaneous values of voltage and current. These losses allow the temperature profile for each device to be calculated and from the mean temperature and magnitude of temperature oscillation the lifetime of the device can be determined.

The model may be used to carry out steady state tests to examine the influence that the operating point and more specifically the frequency of current, have on the lifetime of the semiconductor devices that make up the converter.

Chapter 4. Inverter Temperature Cycling Test Rig

4.1. Justification

To verify the temperature results obtained by simulation a simple inverter test rig may be used. With a small inverter and a controllable power supply the loading of the inverter may be controlled so that the device losses are sufficient to cause reasonable thermal excursion. A simple controller which allows the inverter output frequency to be set to specified values will allow steady state tests to be run for a range of frequencies. In this chapter the design of such a rig and the results that were obtained are presented.

4.2. Test Rig Configuration

The test rig comprised of a DC power supply, an inverter, an inductor and a controllable resistive load bank.

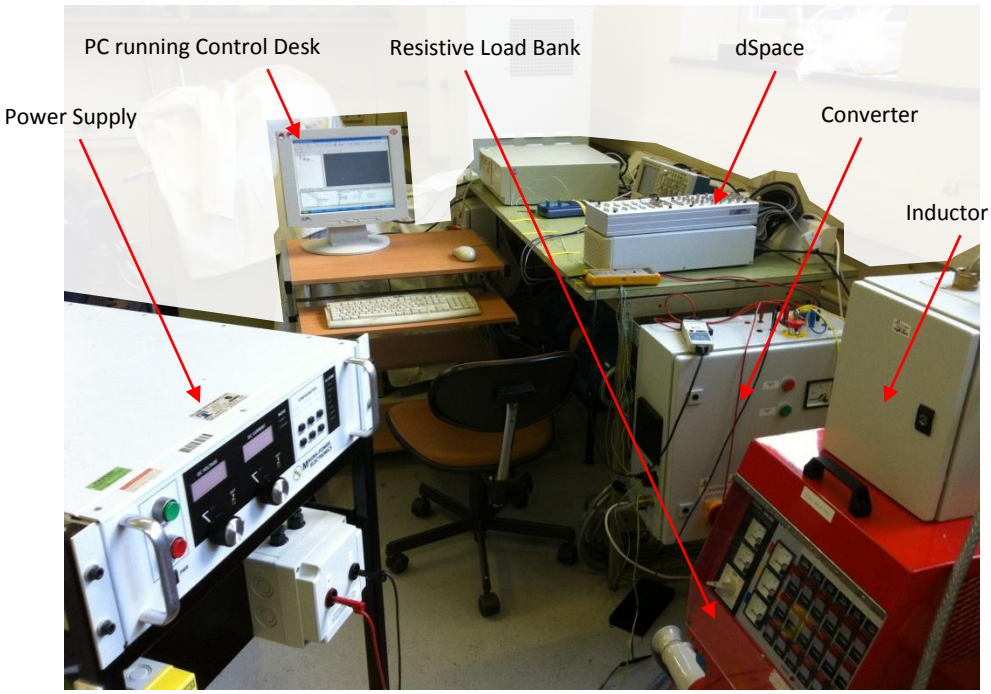

Figure 4-1 Inverter Test Rig

Figure 4-1 shows the layout of the test rig. The DC power supply feeds a three phase inverter which is controlled via dSpace by a PC running control desk software.

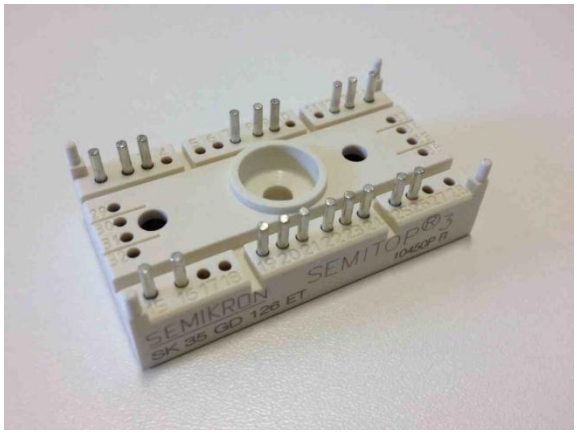

(a) SK35GD126ET module (top)

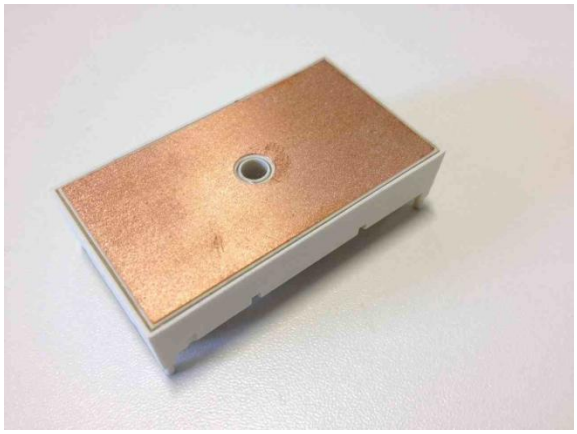

(b) SK35GD126ET module (base)

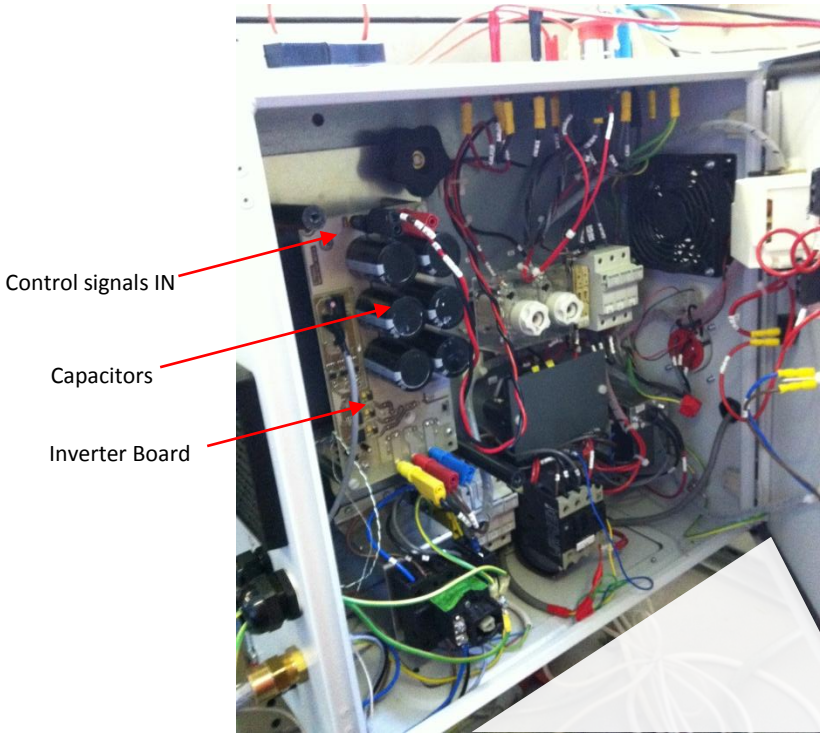

(c)

Figure 4-2 Inverter cabinet

A Semikron SK35GD126ET module (Figure 4-2(a)) was mounted on a PCB together with six capacitors and the ancillary control circuitry. This module was a three phase inverter module with six IGBT-diode pairs and thus had a slightly different architecture to the single phase inverters comprising eight IGBT-diode pairs used in simulation. The module was attached to the opposite side of the PCB to the capacitors and thus was not visible in Figure 4-2. It was mounted on an aluminium heat sink, being there affixed by thermally conductive paste. The cooling fan shown in

Figure 4-2 which circulated fresh air over the heat sink, remained switched off for the present work so that temperature cycles remain undamped and so that steady state could be reached more swiftly.

Temperature measurements were required and hence two type K thermocouples were mounted in the vicinity of the module to allow measurement of the casing temperature and the ambient air temperature around the module. The casing temperature was measured by drilling through the heat sink so that a thermocouple could be placed at the casing-sink boundary. Ambient air temperature was measured by placing a thermocouple behind the module and heat sink, approximately 2cm from the heat sink surface. A TC-08 Thermocouple Data Logger with PicoLog data acquisition software [93] was used to collect the temperature data from the thermocouples.

A dc voltage of 300V was supplied to the inverter and the three output phases were connected to a load comprising a 50mH inductor and a variable resistance load. The controller was modelled in Simulink using ControlDesk as the real-time software environment to provide the gating signals to the module via dSPACE. Temperature samples were gathered at a maximum rate of 66Hz, and as the maximum output frequency examined was 0.5Hz thus this sampling rate provided sufficient resolution to allow observation of thermal cycling.

4.3. The Test

The output frequency of the inverter was set via ControlDesk and remains unchanged for the duration of each test. The power supply voltage was set to 300.2V and the inverter switched on. The variable resistance load bank was set to its minimum value (5.6 Ω per phase) to maximise the current flowing in the converter and thus the power lost as heat.

The dc side current flowing was around 1.8A for all of the tests. By holding the voltage and current constant the only variable that may influence the loss was the frequency. This was varied between each test run through a range from 0.001 to 0.5 Hz (0.001, 0.002, 0.005, 0.01, 0.05, 0.1, 0.5). The temperature of the casing and the ambient temperature (that being the temperature of the air around the inverter) was recorded. The first test was run for an extended period (3000s) to allow the thermal quasi steady state to be approached. The temperature variation could be said to be characterised by a quasi steady state which has two components – the mean temperature and the oscillating component. Successive test runs were carried out whilst the devices were still hot, (ie the mean temperature was still close to steady state).

4.4. Results

Initially an output frequency for the inverter of 0.01Hz was set and the power supply and inverter turned on and allowed to run for 50 minutes. This was long enough for the quasi steady state to be approached. It is the general character of the thermal response that is of interest and thus it not considered necessary to wait until the full quasi steady state was achieved.

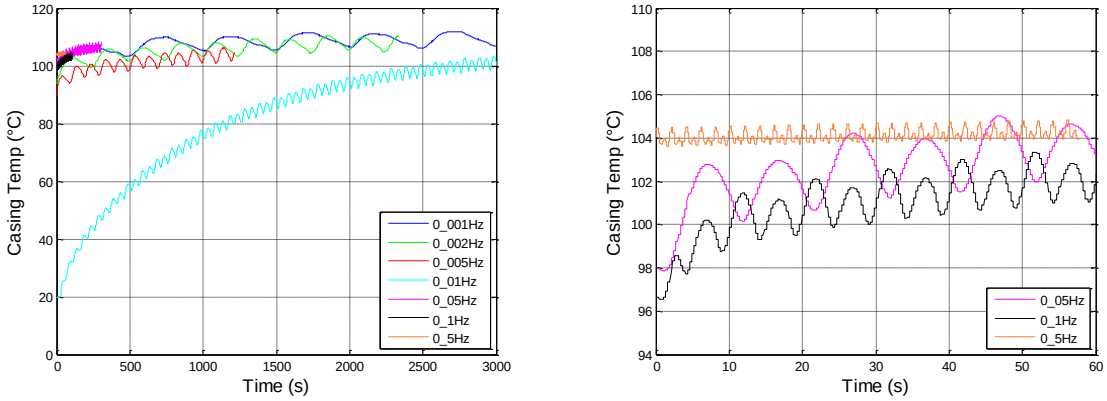

(a) all test runs **(b) high frequencies only**

Figure 4-3 Module Casing temperature vs time

In Figure 4-3 it can be seen that the oscillating component of the temperature has reached steady state, even though the mean temperature is still not quite yet at steady state. Figure 4-3(a) shows the complete set of test runs, however some are difficult to see due to their higher frequency. These are shown in Figure 4-3(b) which has a shorter scale on the x-axis. The frequencies used in the legend to identify each plot are the electrical frequencies set within the controller. The actual frequencies of the temperature variation are found to be double those of the electrical frequency. This indicates that the temperature being measured is being driven by the power loss from one leg of the module.

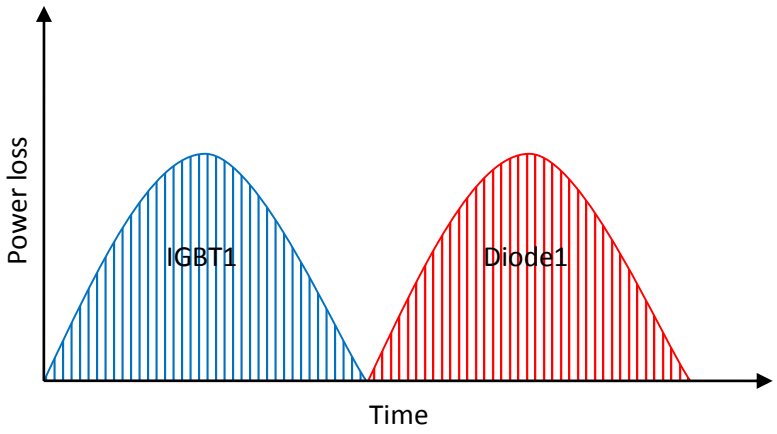

(a) Upper IGBT diode pair

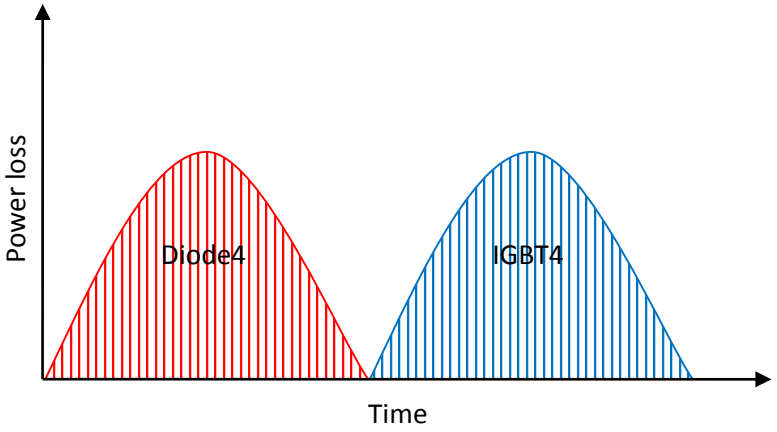

(b) Lower IGBT diode pair

Figure 4-4 Power loss in one inverter leg

The power loss from a single IGBT is in the form of pulsed power losses modulated by the sinusoidal variation of the current but with the second half of each period zero (Figure 4-4 (a)). During the half of the period with zero IGBT loss the anti-parallel diode conducts and so provides a source of loss. The IGBT and diode combined loss oscillates at a frequency that is double that of the line current. With the pair of devices being positioned in close proximity to one another the heat loss from the two will propagate to the same area of the module casing and thus result in a temperature oscillation with a frequency at double the electrical frequency. The complimentary IGBT-diode pair on the same leg of the module will output loss at the same rate but with the IGBT and diode half cycles reversed – that is, the upper IGBT will conduct in the same half cycle as the lower diode and vice versa (Figure 4-4 (b)). The loss from the lower pair could also be contributing to the temperature oscillation measured though this would not affect the frequency. The other two legs

will produce loss that is of the same frequency but shifted in phase. The heat from these other two legs will propagate to the casing in the same manner however this cannot be influencing the temperature measured to any great extent. If all three legs contributed equally to the measured temperature oscillation then the frequency would be six times the electrical frequency, as this would be the frequency of the total loss. The flow of heat, as would be expected, is dominated by the path from the junction to the casing and out through the heat sink. This path will have been designed to have low thermal resistance so the module can function without easily overheating. Thus the lateral flow of heat along the casing will be less and the flow from each module leg will be dominated by the flow directly to the ambient via the heat sink. So it may be said with confidence that the temperature measured has a frequency that is dominated by the loss from a single leg.

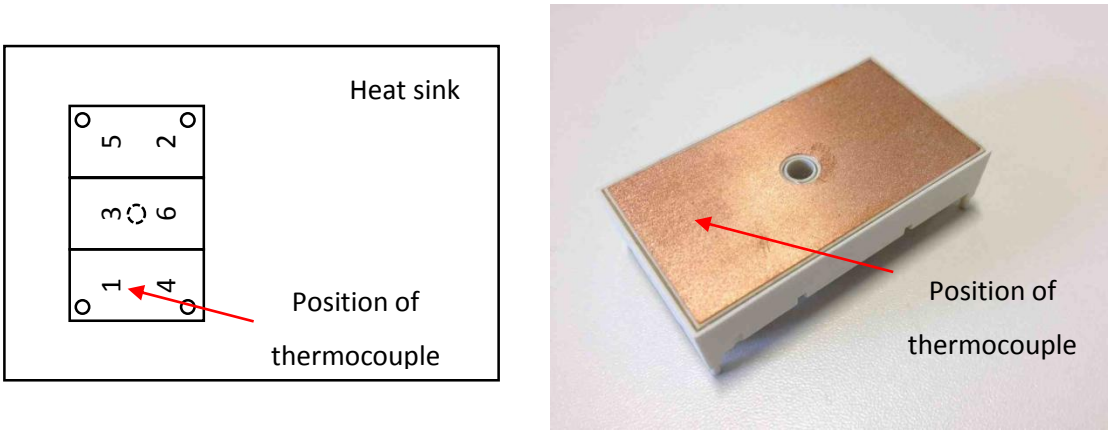

(a) Module schematic **(b) Module**

Figure 4-5 Position of thermocouple on module base plate

The thermocouple is positioned closer to one end of the module, approximately in the middle of the bottom third of the device base plate (Figure 4-5). The temperature measured here is thus a result of power loss from device pairs 1 and 4.

The temperature oscillation frequency determined by simulation was at a frequency equal to that of the electrical frequency. However this was the junction temperature which is not directly measurable in the real world. The junction temperature in the test rig may also oscillate at the same frequency as the current if the main flow of heat is from junction to casing rather than between junctions of neighbouring devices. Though this cannot be measured it does depend upon the relative magnitudes of the junction-junction and junction-casing thermal resistances. If the former

is significantly larger than the dominant heat flow will be from junction to casing and thus the temperature oscillation frequency at a single junction will be dominated by that junction's power loss.

The thermal model in the simulation is structured so that all the device junctions are joined via the casing. Thus the only path for heat to flow from one junction to the other is via the casing and heat arriving at the casing will find an easier path through the heat sink which has low thermal resistance. The internal structure of the module was not verified before constructing the thermal model, however the test rig results indicate that there are no low resistance junction-junction paths for heat flow, thus verifying the assumption in the simulation.

Though the temperature oscillation frequency at the junction is not directly verified by the test rig results, with the above explanation the two sets of results are compatible. The frequency of temperature oscillation at the casing is still directly proportional to the electrical frequency.

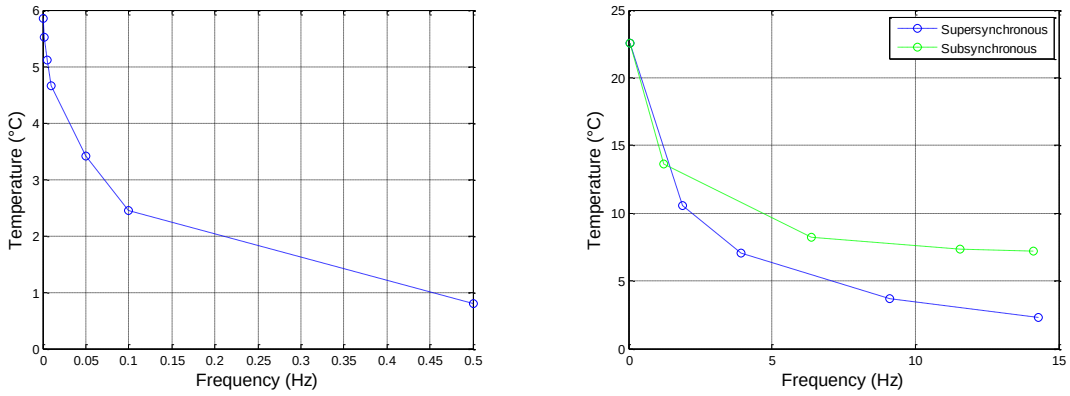

(a) Test rig **(b) Simulation**

Figure 4-6 Temperature cycle magnitude vs Frequency

The magnitude of the temperature cycles also follows a similar pattern to that found from simulation (Figure 4-6), though the limited sampling rate restricts the frequency range of the experimental results. As f=0Hz is approached the temperature cycle magnitude becomes very sensitive to frequency. The temperature cycle magnitudes are significantly smaller than those simulated because the current is considerably smaller (1.8A for the test rig and over 550A in simulation). Also, junction temperature cycle magnitudes (simulation) are compared with casing temperature cycle magnitudes (test rig), the former of which should be larger. As the power loss emanates from the junction the temperature will be highest there as will be the temperature

cycling magnitudes. While these experimental results do not validate the model, they do show the same phenomenon.

4.5. Summary

The test rig results show temperature oscillations can be measured at the casing and are driven by the closest leg or IGBT-diode pair of the module. The heat flow from the rest of the module largely flows in the direction of the heat sink rather than from junction to junction within the module or across the module base plate. This assumption was made during construction of the simulation thermal model and so is verified by the test rig results. The variation in temperature cycle magnitude also follows the same form in the results from the test rig as were found in simulation.

The temperature results found through simulation follow the same variation in frequency and cycle magnitude as those observed through experiment, verifying that the thermal modelling approach is correct and giving confidence that the simulation result are valid.

Chapter 5. Doubly Fed Induction Generator Test Rig

5.1. Justification

The aim of experimental testing was to verify the temperature response obtained from simulation and to facilitate a fuller understanding of the control model Together with results from the Inverter Test Rig (Chapter 4) this should give us a picture of the thermal response of the IGBTs and diodes within a converter.

5.2. Test Rig Configuration

The main rig components were pre-existing as part of the University of Durham, Condition Monitoring Test Rig [94].

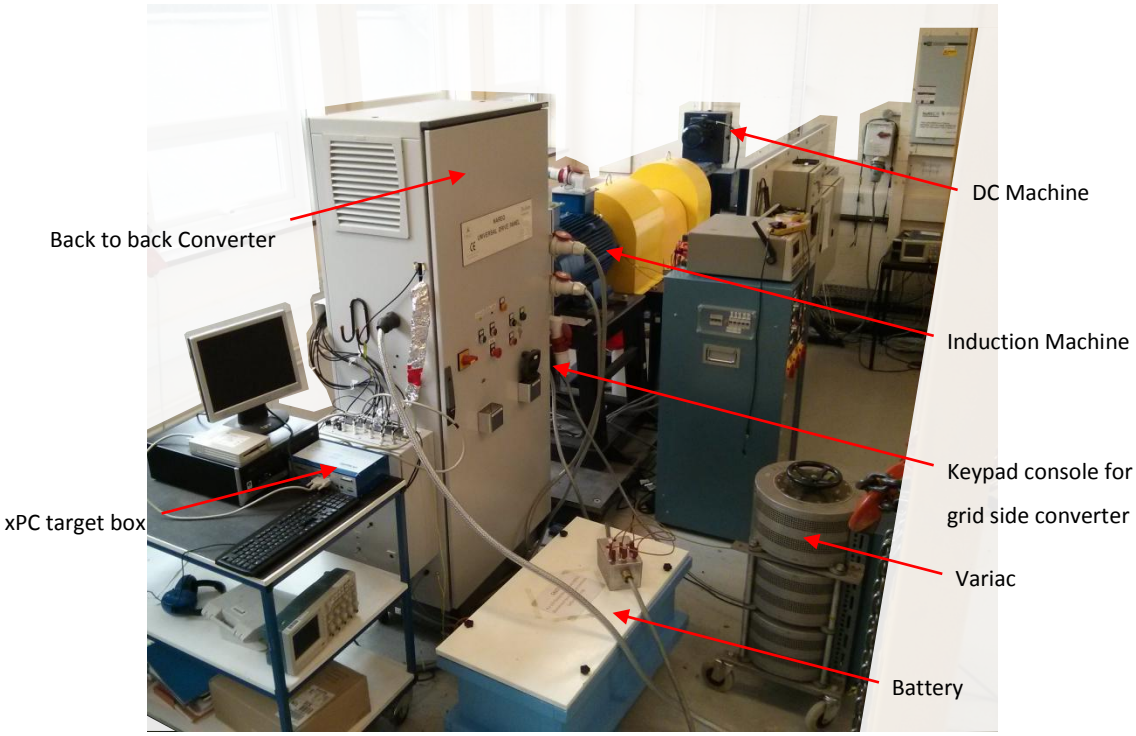

Figure 5-1 DFIG Test Rig

Figure 5-1 shows the test rig which comprised a DC motor and controllable drive unit, an induction machine and various sensory equipment allowing electrical and mechanical variables to be

observed. The induction machine is normally operated with the rotor shorted and is driven by a DC motor, which takes the role of the blades, supplying the torque to the drive train. The DC motor may be operated in two modes - speed control and torque control. These effectively allow the DC motor to operate as a speed source or torque source, neither of which correctly mimics the behaviour of a real WT rotor which, of course, behaves as a power source. For the purposes of the current work, speed control operation was acceptable as the tests were run at steady state, ie constant speed.

The test rig generator was a wound rotor singly fed induction machine, however the current study concerns the doubly fed induction generator operation. Hence some reconfiguration of the test rig was required before testing could begin. In essence all that was required to facilitate DFIG operation was the addition of an electrical connection via a converter to the rotor. To this end, a back-to-back converter unit was commissioned, from Fountain Designs Ltd.

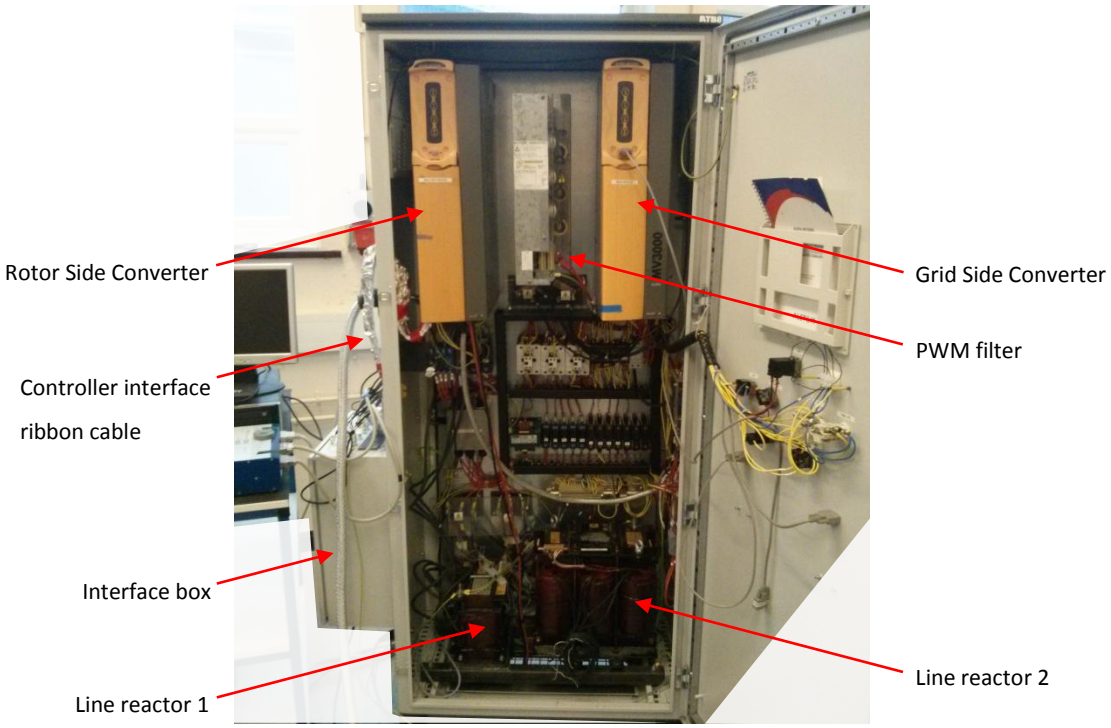

Figure 5-2 Converter cabinet

The converter uses two ALPSA MV3000 MicroCrucible Bidirectional Converters (Figure 5-2). Two line reactors (538µH and 1.749mH) and 3-phase PWM filter are coupled to the grid side converter

to supress any harmonic content fed into the mains, due to the high frequency switching occurring in the devices. The filter is air cooled to prevent over-heating.

The DC drive is controlled via the Labview platform which also allows data to be captured from the voltmeters and currents probes attached to DC motor. xPC target box (Matlab's real time target machine) is used along with Matlab Simulink to control the rotor side converter and allow measurement of electrical variables at the induction machine.

The test rig, including also a battery pack and variac which are used to allow operation of the rig at lower voltages (Figure 5-2).

5.3. The ALPSA MV3000 Converter

The two converter units are slightly different configurations of the MV3000 (rotor side MV3058A4A1 and grid side MV3071J5A1) but house the same Semikron SKiiP3 intelligent power module (SKiiP 132GD120-3DK0176) integrated intelligent power semiconductor subsystem. This, in turn, is comprised of three power modules mounted on an aluminium heat sink. Both rotor side and grid converters have an inbuilt controller which is accessed via a keypad interface. The parameters of both controllers may be tuned to suit the particular application.

When the grid side converter is in use, its built in controller is used to maintain a constant 600V at the dc link. The rotor side converter's controller is bypassed by detaching the ribbon cable from the SKiiP intelligent power module and replacing this connection with one to xPC target box via an interfacing PCB. This is done for two reasons. Firstly, the inbuilt controller is designed for the control of a fully fed induction machine as opposed to a doubly fed machine and secondly, having the flexibility to alter the control algorithm is extremely useful when setting up the test rig and confirming the systems is operating as expected.

5.4. xPC-Target

The machine control model is composed in Simulink. xPC-Target box is used as the real time target machine which is interfaced with the power module to provide the real time control of the machine by supplying the PWM gating signals to the devices. The sampling rate of the target machine is limited by the number of signals that are sampled. Thus the number of parameters measured and fed to xPC is kept to a minimum. The parameters required by the control model are, v_{abs}, v_{bcs}, i_{as}, i_{bs},

i_{cs}, i_{ar}, i_{br}, i_{cr} and θ_r (the angular position of the rotor); the dc-link voltage (v_{dc}) is also recorded to monitor the condition on the batteries. With these ten signals the sampling rate of xPC target box is reduced to 3210Hz. This is more than six times the maximum frequency that is measured (mains frequency, at 50Hz) and thus sampling rate is sufficient to reproduce the measured parameters with adequate fidelity.

The controller generates the reference voltage which is then converted to a duty ratio. From this, the gating signals are then produced via a specialised control card within xPC (Quartz-MM, PC/104 counter/timer and digital I/O module). The associated control block in Simulink allows the switching frequency to be set. This is set at 2kHz.

The PWM gating signals from the xPC target box are 0-5V, whereas the converter requires gating signals of 0-15V. An interfacing PCB is used to convert the three pulse trains output from xPC target box at the lower voltage into the six gating signals required by the converter at the necessary 15V. The doubling of the number of gating signals is achieved by the use of a NOT gate which inverts the three signals that will control the upper IGBTs in each leg, to produce the complementary gating signal required to fire the lower leg IGBTs

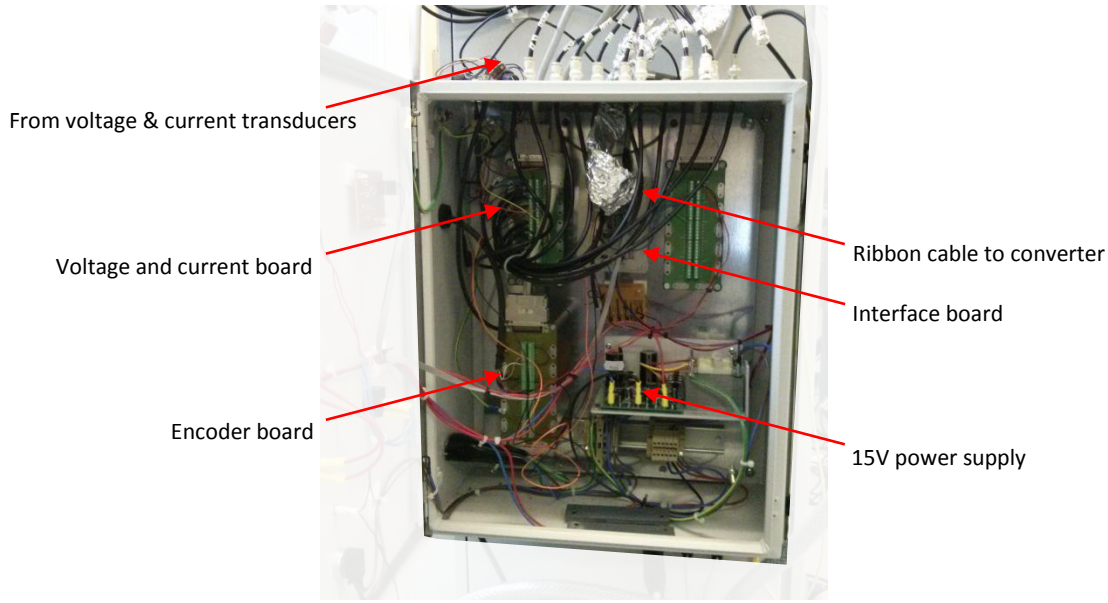

Figure 5-3 xPC interface cabinet

Figure 5-3 shows the ancillary circuitry required to allow operation of the controller via xPC target box. This includes the three I/O boards that allow signals to be fed into xPC target box output from the converter. The black coaxial cables entering the box at the top carry the signals from the current and voltage transducers to one of these boards (top left of Figure 5-3). The encoder signal requires

a separate board (bottom left) and a further board is used to output the gate signals (top right). The 15V power supply required for the gating signals is also included in this interface box.

5.5. Calibration of the Voltage and Current Transducers

Machine control requires that stator and rotor currents and stator voltages are measured. The voltage transducers are LEM, LV25-P type with an accuracy of ±0.8-1.6% depending on the signal size and if the measured voltage at 25°C. The current transducers are LEM, LA 100-P/SP13 with an accuracy of ±0.45-0.70% again dependant on the signal size and at 25°C. The transducers are all mounted on PCBs housing the ancillary components required for their operation as part of the test rig. These transducer cards all require calibration before use with the controller. Calibration is carried by measuring voltages and currents of known values and recording the transducer output.

Figure 5-4 Voltage and Current Transducers

An oscilloscope is used to measure the output from the transducer and these are plotted against the supplied voltage or current. The scale factors relating the actual transducer output with the real measured value are shown in Table 5-1.

Table 5-1 Scale factors for transducer measurement

Measured Parameter	Scale Factor
v_{abs}	-119.236
v_{bcs}	-119.876
i_{as}	10.010
i_{bs}	10.062
i_{cs}	10.014
i_{ar}	9.985
i_{br}	9.993
i_{cr}	10.018
v_{dc}	-119.236

Selected stator and rotor electrical parameters are also measured with current clamps and differential voltage probes so that during operation of the rig the electrical variables may be monitored.

5.6. Calibration of the Encoder

The angular position and speed of the rotor shaft are required by the controller in the calculation of the position of the stator flux and in the calculation of the d and q axis component of the rotor current (v_{dr} and v_{qr}).

Figure 5-5 Encoder mounted on generator rotor shaft

A Sick Stegmann DRS61 incremental encoder is used for this purpose (Figure 5-5). This has a resolution of 2^{15} sectors per rotation and can therefore provide very accurate positional information for the rotor shaft, and thus its rotational speed.

Again calibration is required. In this instance the process of mounting the encoder to the shaft means that there will be some angular offset between the zero position of the encoder and an orientation of the rotor shaft that is specified as its zero position. The latter is taken as when the rotor coils are aligned to the stator coils. It is necessary to obtain an accurate determination of this value as it will affect the position of the d-q reference frame onto which the electrical variables will be projected. The machine equations are simplified assuming stator flux orientation of the q-axis. An incorrect determination of the encoder offset invalidates the use of these equations.

The calibration may be achieved in several ways. The means employed in the current work involved supplying AC current to the stator (the mains voltage was stepped down using a variac) and capturing the line to line stator voltage and rotor induced voltage on an oscilloscope. The rotor shaft was rotated by hand and the phase difference between the two signals observed on the oscilloscope. When the traces are aligned the stator and rotor coils are also in alignment and the rotor is at the zero position. At this rotor orientation, the encoder signal is obtained via the real

time xPC target box scope and this is noted. The encoder angle may then be determined using equation 5-1

$$\theta_{\text{r offset}} = \frac{\text{encoder ouput}}{2^{15}} \times 2\pi \qquad 5\text{-}1$$

$$= \frac{12532}{2^{15}} \times 2\pi$$

$$= 2.403°$$

5.7. The Control Model

A doubly fed induction machine requires one controller for each converter. The grid side converter must maintain the dc link voltage whilst real power flows in either direction across the back-to-back converter assembly. Each MV3000 converter has a built-in controller that may be modified via a control panel. In the case of a mains bridge this is useful as the built-in controller can be set to operate in the required manner, with the desired dc voltage being set to the level required. It is also possible to set the built-in controller for one MV3000 unit to operate as machine controller, though this places limitations upon the control algorithm that can be specified to those pre-installed by the manufacturer. The control model from the simulation is used with the control gain beings suitably adapted. The measured stator currents and voltages are filtered to remove the slight dc offset present in these measurements. A high pass filter with a time constant of 0.25s is found to provide adequate noise reduction. A filter is also used after the integration is carried out in the calculation of the flux position. The integral operation will cause an offset if integration starts at any point other than a turning point. A high pass filter removes the dc offset here. The rotor current is quite noisy and so a low pass filter is used to remove some of the high frequency noise. The speed of the rotating flux is determined by taking the derivative of its position; the rotor speed is found in a similar way. The rotor position is reset every full revolution and so, like the flux position, has a saw tooth form. Taking the derivative of such a signal gives a large negative spike once every cycle. Filtering removes these. Some discontinuities are still present in the rotor speed signal possibly due to a manufacturing defect in the encoder. A rate limiter is added to the controller to cap the maximum gradient. Limiting the rate of change to less than 100rad.s^{-2} removes the remainder of the discontinuities.

5.8. Induction Machine

The induction machine is a 30kW, 4 pole, wound rotor machine built by MarelliMotori (E4F 225 M4 B3). The machine parameters are outlined below in Table 5-2.

Table 5-2 Induction Machine Parameters [94]

Parameter	Symbol	Value
Stator resistance	R_s	0.079Ω
Stator reactance	X_s	0.252Ω
Resistance representing core loss	R_m	131.9Ω
Stator magnetizing reactance	X_m	9.39Ω
Rotor resistance	R'_r	0.072Ω
Rotor reactance	X'_r	0.408Ω
Turns Ratio	N_{sr}	1.272

5.9. DC Drive Motor

The test rig is driven by a 54kW DC motor. The driving characteristic (speed or torque) is controlled by a Eurotherm variable speed drive. Control of the drive is possible via LabVIEW software, this also interfaces with the data acquisition instrumentation in the test rig which allows real time observation of stator currents and voltages associated with the DC machine as well as drive train vibration, and mechanical torque.

Driving profiles may be pre-set by the user in LabView giving the options of steady state and dynamic testing.

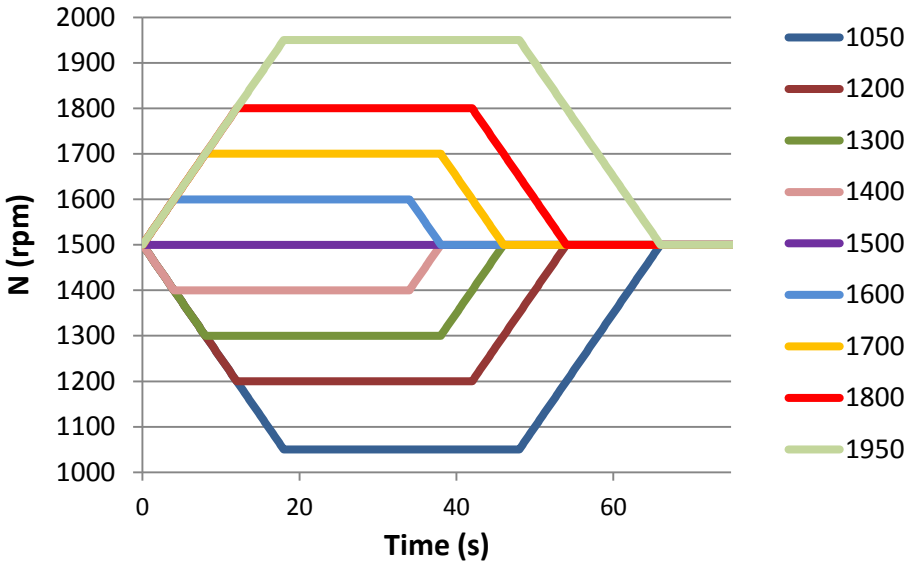

Figure 5-6 DC Motor Driving Profile

Steady state driving profiles at a range of rotational speeds are created (Figure 5-6). This allows the performance of the controller to be examined at a range of speeds that covers the ±30% of synchronous speed that is taken as representative of a standard DFIG operating range. Synchronisation of the DFIG is preferred at synchronous speed as at this condition the power flowing through the converter and in the rotor is at a minimum, though neither the mechanical torque produced nor total power is minimized at this speed so when synchronising there is a step change in both. This is not seen as a problem as the torque reference is set to a low level (15Nm) and the test rig is capable of running at considerably higher than this.

The DC variable speed drive may operate in two control modes; speed control and torque control. Neither of these control modes simulates what is actually happening in a WT. The DC motor plays the part of the rotor blades and thus should operate as a power source, so that a breaking torque applied by the DFIG will correspond to a rise in mechanical torque. For the purposes of steady state tests, speed control is suitable as it allows operation at a single speed, with the torque being set by the DFIG controller.

5.10.Low Voltage DFIG Rig

For safety reasons, it was decided that the test rig should be operated at a voltage lower than the rated 400V, certainly until the DFIG rig had been fully tested. This was achieved by replacing the

mains side converter with a battery pack consisting of four, 12V lead acid batteries (Figure 5-7). The dc link voltage was thus reduced from 600V to 48V. A lower rotor voltage implies that the stator side voltage must also be reduced and this was achieved by inserting a variac between the grid and the stator.

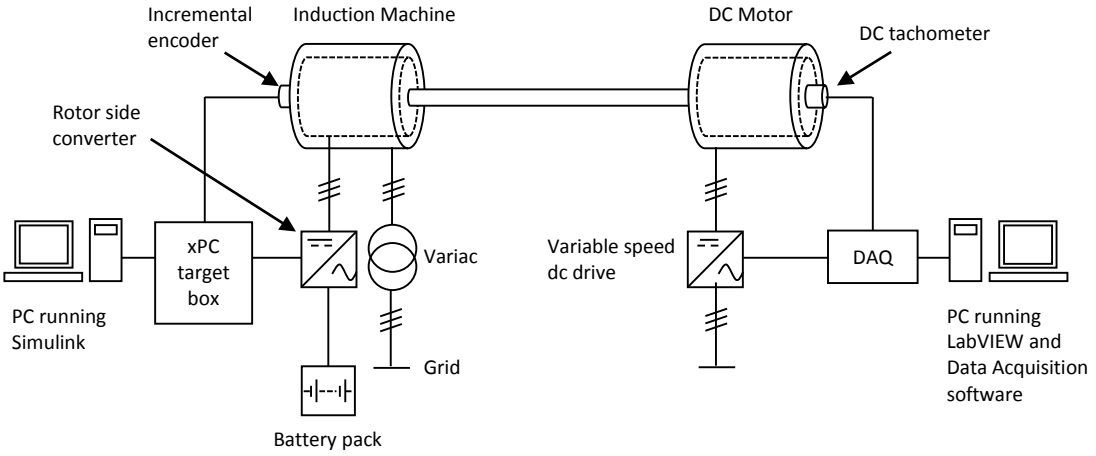

Figure 5-7 Doubly Fed Induction Generator Test Rig configured for low voltage operation

The stator voltage (V_s) required can be determined by firstly calculating V_r from the dc-link voltage.

$$V_r^R = \frac{m_a V_{dc}}{2\sqrt{2}} \qquad 5\text{-}2$$

Recalling equation 3-7 and rearranging,

$$V_s \approx \frac{N_s}{sN_r} V_r^R \qquad 5\text{-}3$$

And combining equations 5-2 and 5-3, gives,

$$V_s \approx \frac{N_s}{sN_r} \frac{m_a V_{rdc}}{2\sqrt{2}} \qquad 5\text{-}4$$

The modulation index at maximum slip (s=0.3) should be approximately 1 and this allows the stator voltage at this operating point to be calculated. The stator voltage will be of the same value at all values of slip and a suitable value for the stator voltage is arrived at.

$$V_s = 71.96V. \qquad 5\text{-}5$$

Hence the variac is set to step the grid voltage down from 240V to 72V, requiring a variac setting of 30% (240V x 30% =72V).

5.11.Results

The test rig was operated, in the low voltage configuration, for a range of steady speed tests. The DC motor accelerated up to synchronous speed at which point the control model was started by initialising xPC Target box. Due to the presence of filters in the control algorithm, some time is required to allow the phase lag to be overcome (15s). Once this has happened then the xPC interface board is switched on and the gating signals are sent to the converter. Hence the generator starts to produce torque. Connecting the generator at synchronous speed means that the rms rotor current is minimised, the machine torque would be minimised by starting at the lowest speed but at this operating point the rotor current would be quite high.

The DC motor was then accelerated up to a predetermined speed before remaining at constant speed for approximately one minute and then returning to synchronous speed (as per the driving profiles in Figure 5-1) at which point the generator could be disconnected by switching off the xPC interface board.

5.11.1. Current

The stator and rotor current should be related to one another by the turns ratio and so examining whether this is measured to be the case provides a good check on the fidelity of the observations.

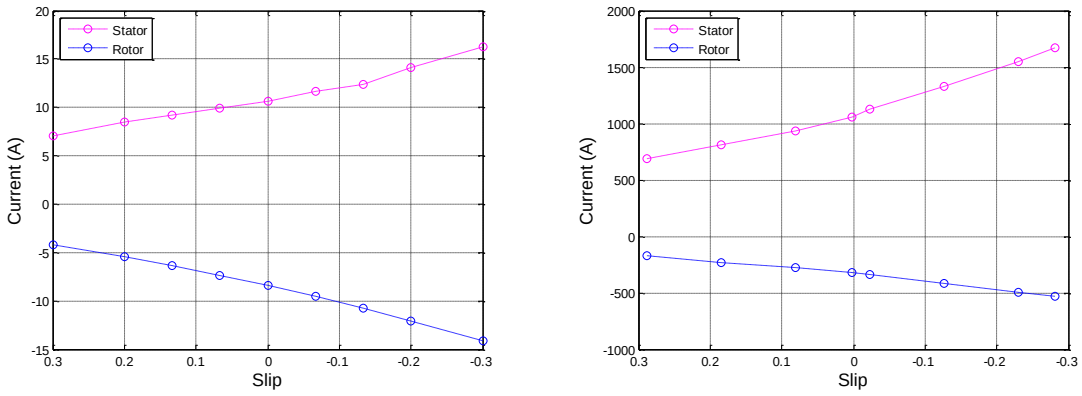

(a) Test Rig **(b) Simulation**

Figure 5-8 Stator and Rotor RMS Current

Figure 5-8 (a) shows the stator and rotor currents, obtained from testing. The ratio between the two currents varies a little with slip but has a mean value of 1.3324, which is close to the rotor to stator turns ratio (N_{sr} = 1.272). The discrepancy most likely emanates from the fact that measured current is quite noisy and so some filtering is necessary to extrapolate an average peak value.

Looking again at the simulated values of rotor and stator current (Figure 5-8 (b)) they are seen to follow a similar trend to the experimental data, though the turns ratio differs and thus so too does the ratio of rotor to stator current.

The q component of the rotor is used to control the machine torque with the d component being controlled to be zero to minimise reactive current.

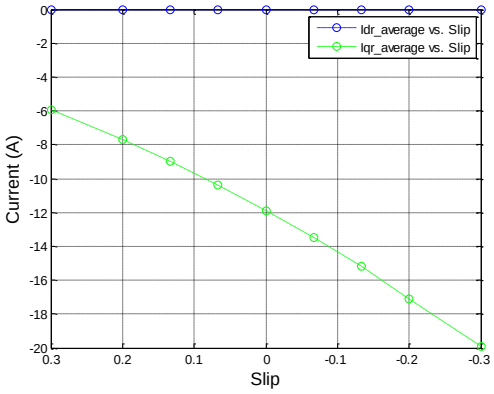

Figure 5-9 Idr and Iqr

Figure 5-9 shows the d and q rotor current components. The rotor d-current is very close to zero with a maximum value of 0.0065A. The rotor q current increases with speed as might be expected. The actual current torque relationship may be determined for the purposes of comparison.

Recall

$$\underline{i}_{qr} = \frac{2}{3p}\frac{L_s}{L_m}\frac{\omega_s}{\hat{v}_g}T_e \qquad 5\text{-}6$$

and

$$T_{ref} = k\omega_m{}^2 \qquad 5\text{-}7$$

and if T_{em} follows T_{ref}, then

$$\underline{i}_{qr} = \frac{2}{3p}\frac{L_s}{L_m}\frac{\omega_s}{\hat{v}_g}k\omega_m{}^2 \qquad 5\text{-}8$$

And so

$$\underline{i}_{qr} \propto \omega_m{}^2 \qquad 5\text{-}9$$

The q-axis current has a squared dependence on rotor speed and this is reflected in the shape of the i_{qr} curve in Figure 5-9. Using equation 3-45 and calculating the value of k based upon the measured P_{max} from $k = \frac{P_{max}}{(1.3\omega_s)^3}$ the theoretical profile of i_{qr} may be determined.

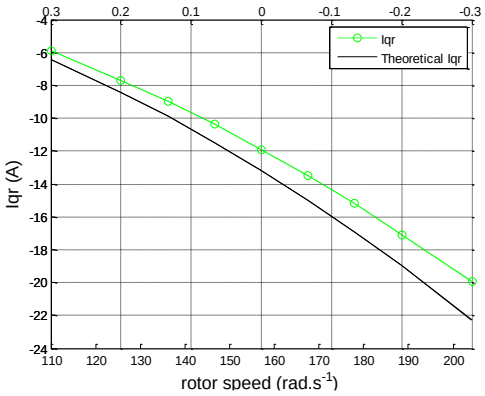

Figure 5-10 Measured and theoretical rotor q-axis current

From Figure 5-10 it may be seen that the measured q-axis current characteristic is quite close to that anticipated by the theory. The discrepancy here may be accounted for by the noise on the measured values of rotor current from which i_{qr} is extracted and also on the voltage and current measurements that are used to determine the instantaneous power, P_{max} and thus the theoretical i_{qr}.

5.11.2. Voltage

The rotor voltage variation with slip is approximated by recalling equation 3-7.

$$V_r^R \approx \frac{sN_r}{N_s} V_s \qquad 5\text{-}10$$

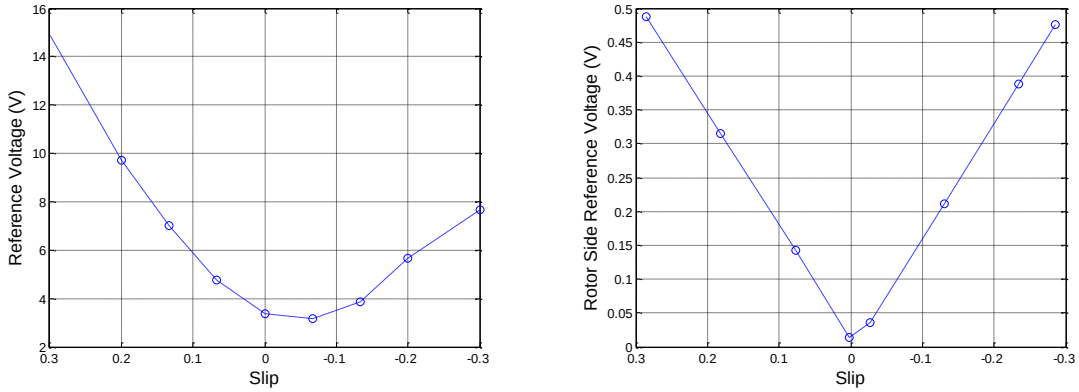

(a) Test Rig **(b) Simulation**

Figure 5-11 Rotor Reference Voltage

Figure 5-11 shows that the test rig reference voltage follows the general shape of the simulated results. It is noticeable that the test rig reference voltage does have its minimum at zero slip, as might be expected from equation 5-10. In actual fact it is the EMF that should be minimised at s=0, as $E_r = s\mathrm{E}_s$.

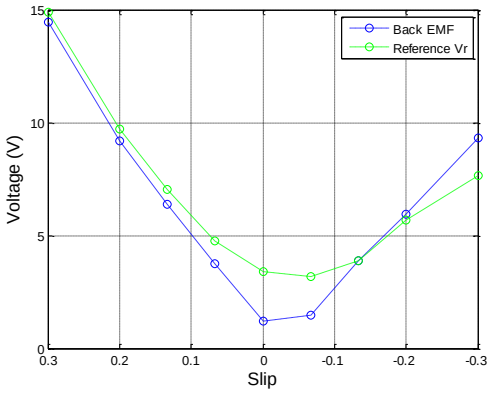

Figure 5-12 Rotor Reference Voltage and EMF

Figure 5-12 shows the rotor reference voltage and the back EMF. The EMF falls to a minimum at s=0. At true zero slip the EMF should be zero as there is no relative motion between the rotor and the magnetic field. This error most likely comes from two sources, the speed measurement and the current measurement.

The speed of the test rig is controlled by setting the DC Motor to drive at a certain selected rotational speed. In operating the test rig the speed is never perfectly constant however it was

measured via the encoder and found to be very close to synchronous speed (within five rpm). The oscillation about the true synchronous speed will of course induce some voltage in the rotor.

As for the current measurement, although this was filtered, there is still some noise present and this will have an effect on the determination of the reference voltage.

5.11.3. Power

With the current and voltage plots from the simulation having the same form as those produced from test rig experimental data, it is likely that the real and reactive power characteristics will also follow the trend with slip. The phase angle could however differ and thus it remains useful to plot the real and reactive power for the stator and rotor and make a comparison with the simulated data.

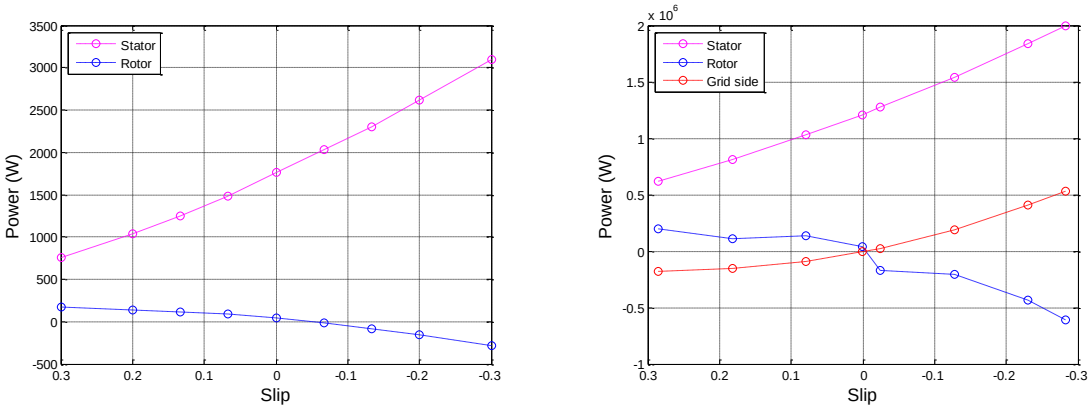

(a) Test Rig

(b) Simulation

Figure 5-13 Stator, Rotor and Grid Side Power

As expected the power flow in the test rig follows the control law set in the controller. The rotor power reverses direction at approximately zero slip. The grid side converter power is included in Figure 5-13 due to the fact this is easier to filter than the rotor power (being as the frequency is the same at all values of slip).

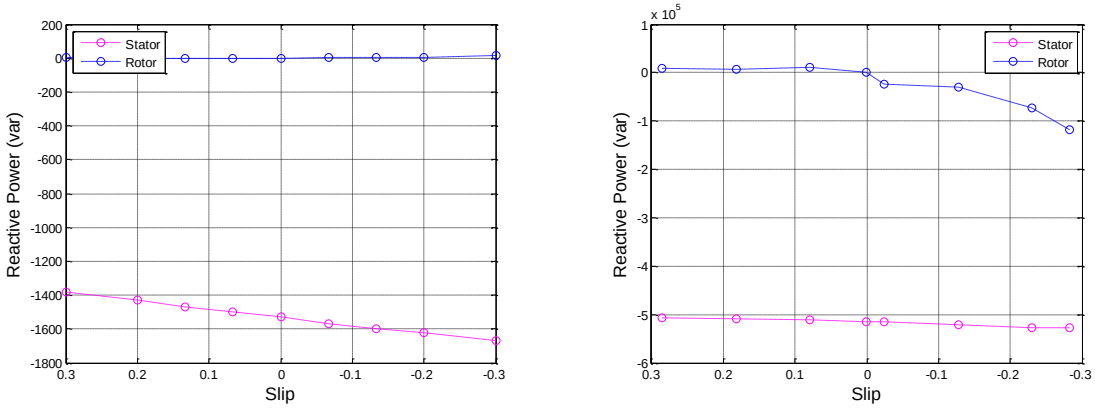

(a) Test Rig **(b) Simulation**

Figure 5-14 Stator and Rotor Reactive Power

The measured reactive power also showed the same variation with slip as was seen in the simulation results (Figure 5-14).

5.11.4. Temperature Results

The Semikron inverter modules have a built in temperature sensor whose output was fed to xPC target box. The temperature response was recorded but found to be unchanged throughout operation of the test rig. This indicates that the power level is not high enough to raise the temperature of the module. The low voltage set up (ensured by use of the battery pack as dc source for the rotor side converter and variac stepping down the grid voltage to the stator) means that the power flowing through the rotor side converter is significantly reduced from that which would be achieved by operating at mains voltage the corresponding rotor voltage. The max rotor power achieved is about 400W and as the rating of the rotor side converter is 30kW thus it can be said that the converter is very lightly loaded even at maximum power.

Verification of thermal results is not possible with the low power test rig setup. The test rig was reconfigured to run in full back-to-back operation so as to increase the operating power levels and thus the power loss in the converter. The test rig was operated at synchronous speed and then at s=-0.13. Again no temperature variation was observed. The converter was designed for use in a fully fed system as opposed to DFIG, and thus had a much higher rating than required by the current setup (ie the converter was rated to 30kW as was the generator and so the maximum power flow on the rotor side anticipated would be 0.3x30kW=9kW). Therefore, it is likely that the converter was still too lightly loaded to allow raising of the device temperatures.

5.12.Summary

Verification of the temperature results was not possible; however, the control model algorithm was verified. The experimental study allowed for a full understanding of the control model to be gained. Detailed effects are better revealed through experimental work. An understanding was gained of how the operating point changed with slip. Later analysis of simulation results depends on the knowledge and appreciation gained of the current and voltage variation with slip, most notably around the synchronous speed point.

With the control model verified and understood, temperature verification could be carried out on a basic inverter test rig, comprising a power source, inverter and load. This would allow greater control over experimentation as power levels could be controlled much more easily to levels which gave the appropriate heating.

Chapter 6. **Steady State Simulation MPPT**

The following chapter will present a discussion of the results of simulation of the DFIG WT under steady state wind conditions. Power loss and temperature results will be outlined and discussed for the quasi-steady state temperature characteristic that results from steady wind conditions. The lifetime implications are estimated based on an empirical formulisation and discussed.

6.1. Power Flow in the Machine

In the DFIG real power is, at all operating points, flowing from the stator to the grid. The rotor however may at times receive power from the grid whilst at other times act as a source of power.

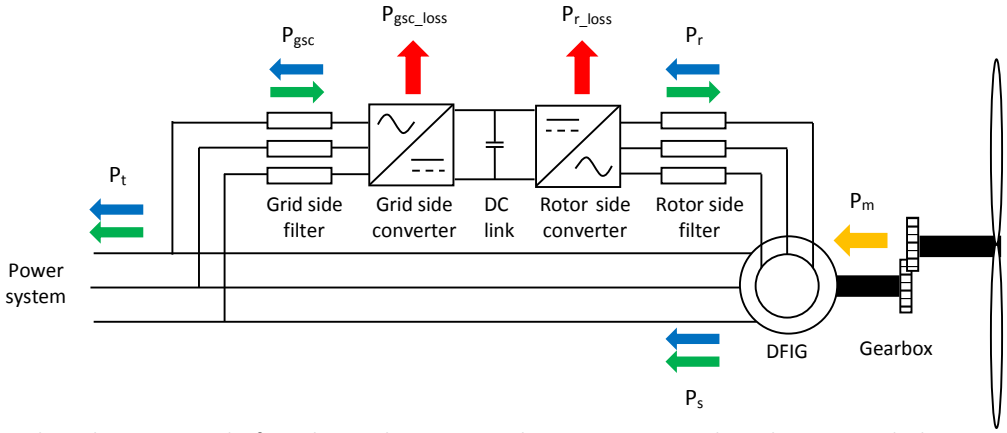

Colour denotes speed of machine relative to synchronous. Green: subsynchronous and Blue: supersynchronous

Figure 6-1 Power Flow Diagram for DFIG WT

As shown in Figure 6-1 the direction of power flowing through the back-to-back converter arrangement depends on whether the machine is operating in subsynchronous or supersynchronous mode. The loss, of course, occurs irrespective of the direction of power flow, but it is worth examining in detail the Power vs Wind Speed relationship for the real power flowing through the back-to-back converter arrangement. The Power vs rotor speed follows a cubic relationship modified by the slip (6-1).

$$P_r = k\omega_r^3 \div \left(\frac{1}{s} + 1\right) \qquad 6\text{-}1$$

and the Power vs Wind Speed relationship has a similar characteristic (6-2).

$$P_r = \frac{1}{2} c_{p\_max} \rho A V_w^3 \div \left(\frac{1}{s} + 1\right) \quad \text{6-2}$$

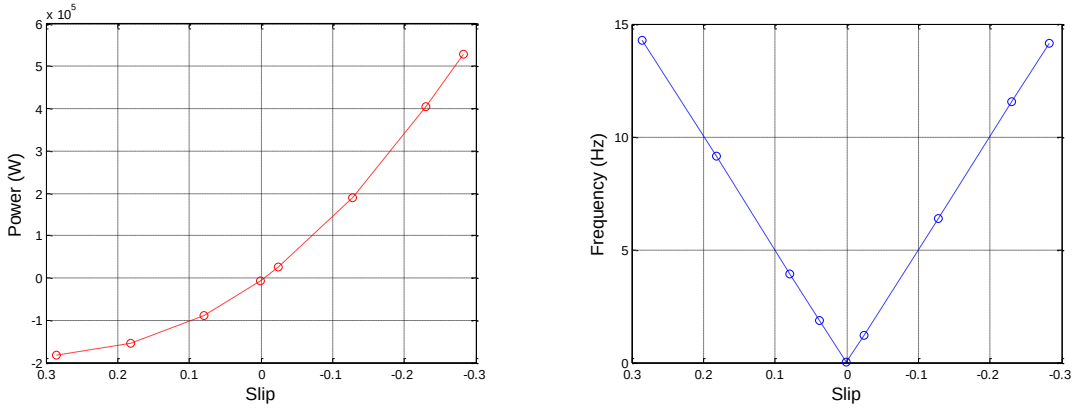

Figure 6-2 (a) Grid Side Converter Power vs Wind Speed and (b) Frequency vs Wind Speed

The Grid Side Converter Power P_{gsc} is shown in Figure 6-2(a). This is very close to the Rotor Power, the difference between the two being the converter power losses. P_{gsc} can be said to be the output from the rotor that actually is fed to the grid or is drawn from it.

The loss might be expected to exhibit a characteristic which has frequency dependence as well as a dependence on the power through the converter. One might suppose that the power loss would follow the same relationship as the real power flowing in the converter. This is not entirely true since there is a relationship between the two it is more accurate to say the loss follows the variation in current. Whilst the power drops off as synchronous speed is approached, the rotor current continues to rise with wind speed across the full range of speeds.

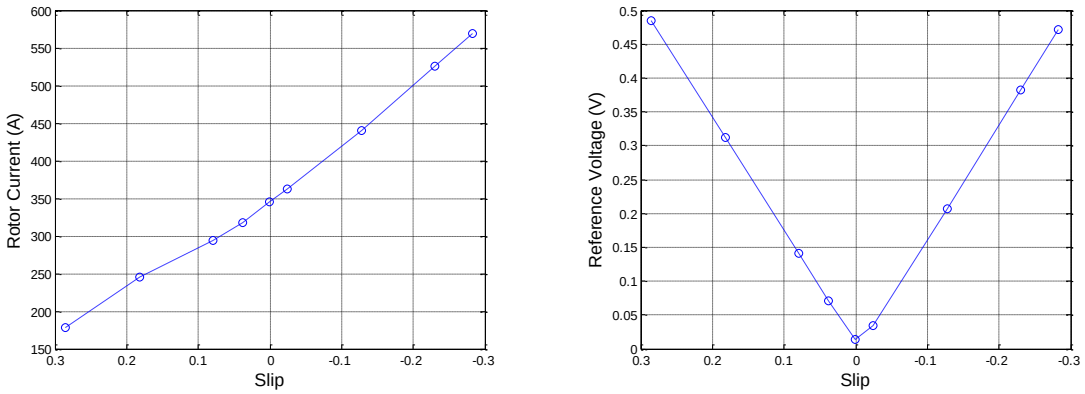

(a) (b)

Figure 6-3 (a) Rotor Current vs Slip (b) Rotor Reference Voltage vs Slip

This is shown in Figure 6-3, which also shows the reference voltage for the rotor side controller (the reference voltage is used to illustrate the point as the measured voltage is, of course, a PWM waveform, requiring filtering to ascertain the fundamental component). A consideration of the relationship between the power and speed provides some illumination of the idea that power is reducing to zero but with power loss remaining present.

$$P_r = sP_s \tag{6-3}$$

At synchronous speed, s=0

$$P_{r\_synch} = 0 \tag{6-4}$$

Rotor power at synchronous speed is zero

$$\omega_{max} = 1.3\omega_s \tag{6-5}$$

Total power

$$P_t = k\omega_r^3 \tag{6-6}$$

Recall equation 3-48

$$k = \frac{P_{t\_max}}{(1.3\omega_s)^3} \tag{6-7}$$

And thus

$$P_t = \frac{P_{t\_max}}{(1.3\omega_s)^3}\omega_r^3 \quad 6\text{-}8$$

$P_{t\_max} = 1.3P_{s\_max}$ and allowing that $\omega_r = \omega_s$ the total power at synchronous speed may be found

$$P_{t\_synch} = \frac{1.3P_{s\_max}}{(1.3\omega_s)^3}\omega_s^3 \quad 6\text{-}9$$

$$= \left(\frac{1}{1.3}\right)^2 P_{s\_max} \quad 6\text{-}10$$

$$= 0.5917P_{s\_max} \quad 6\text{-}11$$

So at synchronous speed the total power is 60% of the maximum stator power. And as the rotor power is zero here, then

$$P_{s\_synch} = 0.5917P_{s\_max} \quad 6\text{-}12$$

Examining the current at synchronous speed,

$$I_{s\_synch}V_{s\_synch} = 0.6I_{s\_max}V_{s\_max} \quad 6\text{-}13$$

As the stator voltage is constant then,

$$I_{s\_synch} = 0.6I_{s\_max} \quad 6\text{-}14$$

Mmf balance

$$I_{r\_synch} = 0.6I_{r\_max} \quad 6\text{-}15$$

Hence we see that whilst the rotor power has reduced to zero at synchronous speed the rotor current remains at 60% of its maximum value. It is the fundamental component of the voltage reducing to zero that is responsible for the rotor power being zero at synchronous speed. The instantaneous value of voltage however is non-zero. Instead the voltage across the devices is at all times switching between a close to zero state (when conducting) and a high state (when open/blocking). The magnitude of the fundamental component of voltage does affect the power

loss by changing the ON time for the switches but the actual voltage across the device is, of course, the instantaneous value.

A voltage across a device with current flowing therefore means that there is loss present. So loss is still expected even when the output power of the converter is zero. The converter, as would be expected, dissipates energy at all times it is operating. The loss and resulting temperature will have a characteristic that has dependency on current and operating frequency, both of these being functions of the operating point.

Contrastingly (as will be shown below) the power loss at the grid side converter does move toward zero at synchronous speed. In the case of the grid side converter, whilst the rms value of the voltage remains non-zero at all wind speeds, the rms current drops toward zero at zero slip.

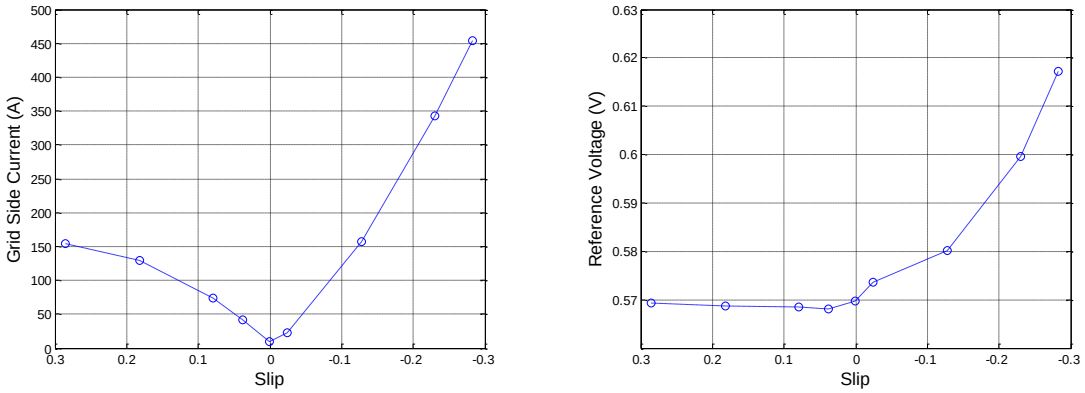

(a) **(b)**

Figure 6-4 (a) Grid Side Converter Current vs Slip (b) Grid Side Converter Reference Voltage vs Slip

The grid side current follows the variation of the real power being fed to or taken off the rotor. At synchronous speed the cross over point is reached whereby the power flow changes direction and at this point $Pr \approx 0$. The rotor current must at all times maintain the mmf balance and thus must increase as the stator current does.

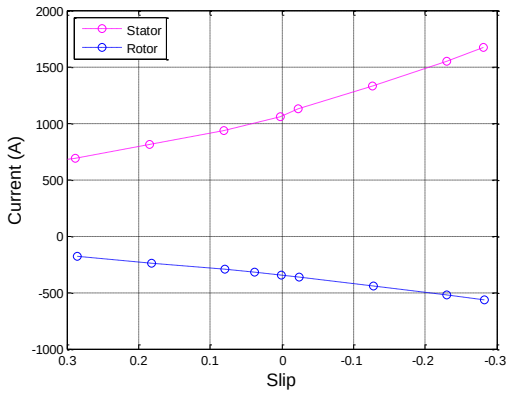

Figure 6-5 Stator and Rotor Current vs Slip

Figure 6-5 shows the rotor current has a magnitude that is equal to one third of the stator current, as is expected with a stator to rotor turns ratio of one third.

6.2. Power Loss Results

The temperature cycling at device level is driven by the power loss at the junction. The relative influence of switching loss and conduction loss depends on the operating point. A series of steady state simulations were run at a range of wind speeds spanning the range of operation of the converter.

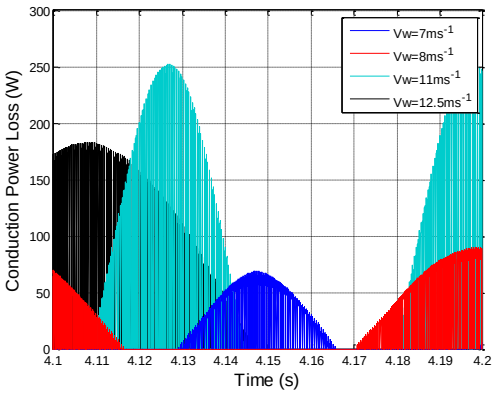

(a) IGBT Conduction Loss

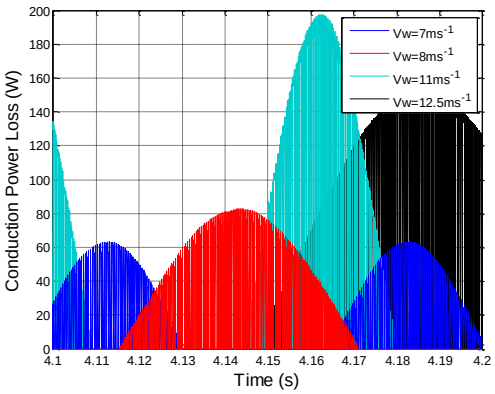

(b) Diode Conduction Loss

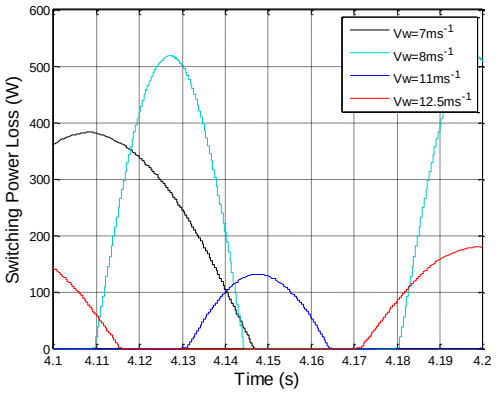

(c) IGBT Switching Loss

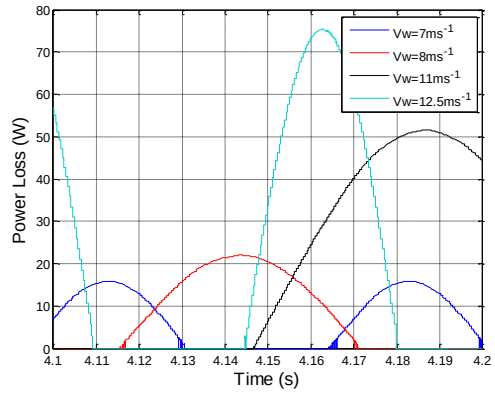

(d) Diode Switching Loss

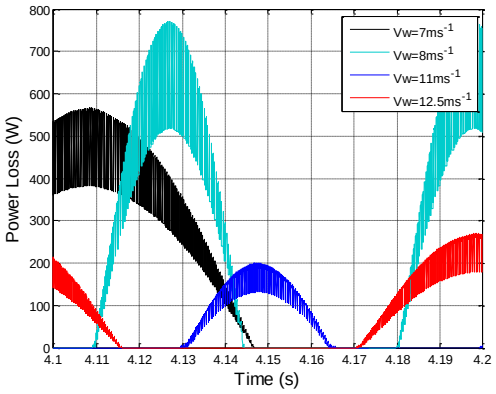

(e) IGBT Total Loss

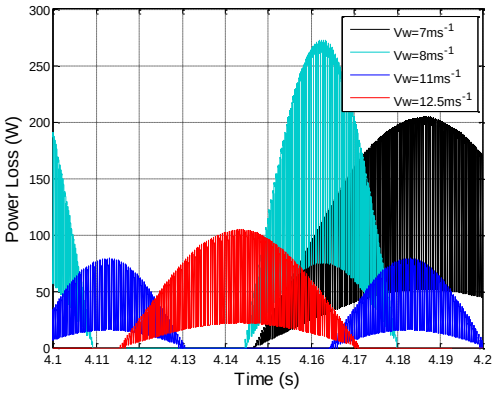

(f) Diode Total Loss

Figure 6-6 Rotor Side device power losses

Sample losses for the rotor side devices are shown in Figure 6-6 for subsynchronous (7 and 8ms^{-1}) and supersynchronous (11 and 12.5ms^{-1}) operation. The grid side losses are shown in Figure 6-7 (note the timescale on the x-axis is reduced for higher resolution).

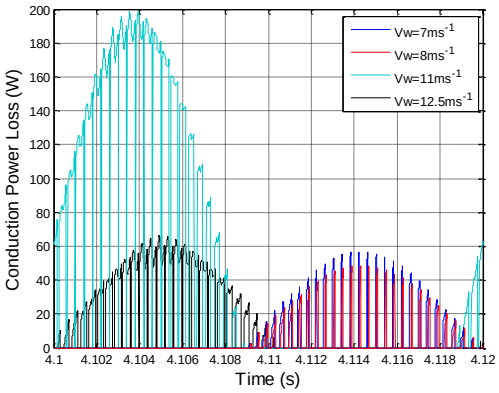

(a) IGBT Conduction Loss

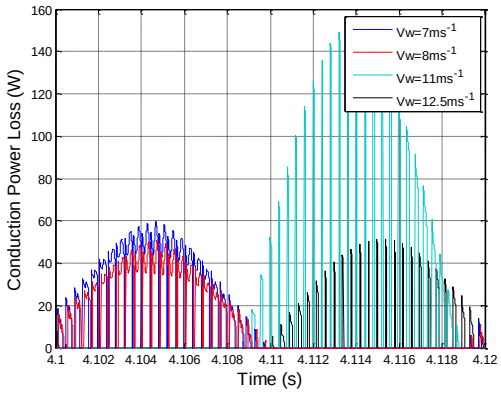

(b) Diode Conduction Loss

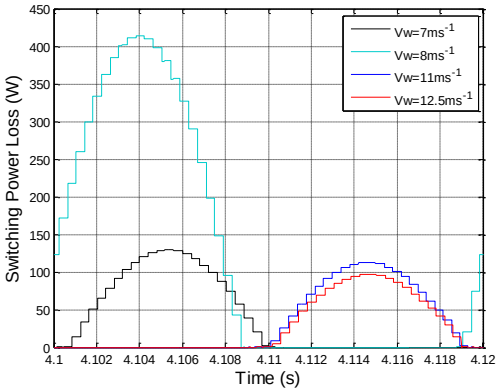

(c) IGBT Switching Loss

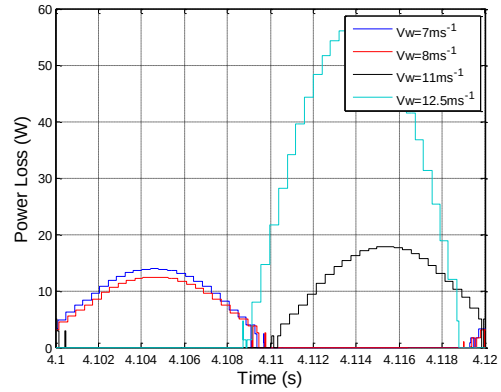

(d) Diode Switching Loss

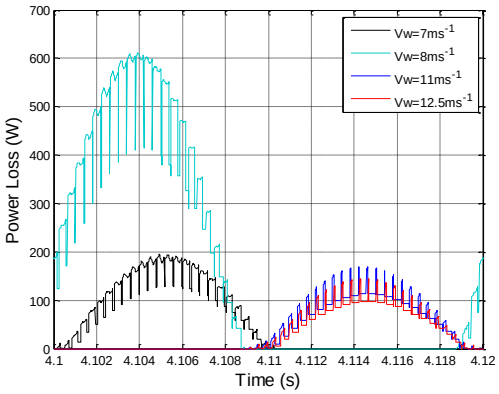

(e) IGBT Total Loss

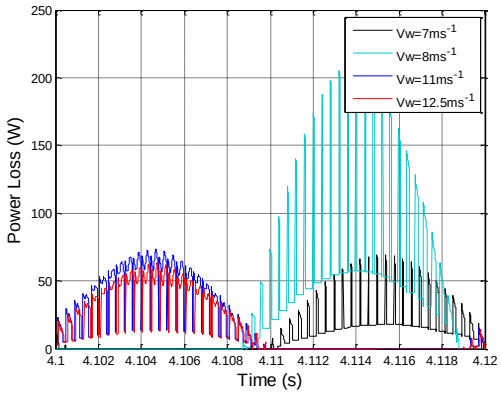

(f) Diode Total Loss

Figure 6-7 Grid Side device power losses

The losses are characterised by two frequency components; the switching frequency which, at 2.5kHz, is too high to have any effect upon the temperature of the devices (given the thermal impedance) and the fundamental frequency of the current, which is much lower and is 50Hz for the grid side converter and lower on the rotor side. The rotor side frequency is dependent on the operating point as too is the magnitude of all the losses, both conduction and switching, in both converters.

The loss profile and how it varies with wind speed may be examined by looking at the mean power loss P_{loss_mean} and the frequency of variation of the loss. These features of the loss characteristic control the mean temperature reached by the device and the temperature cycling frequency. The mean junction temperature will of course be dependant also on the thermal impedance of the devices as too will be the temperature cycling amplitude.

Power Loss Comparison Within Each Device

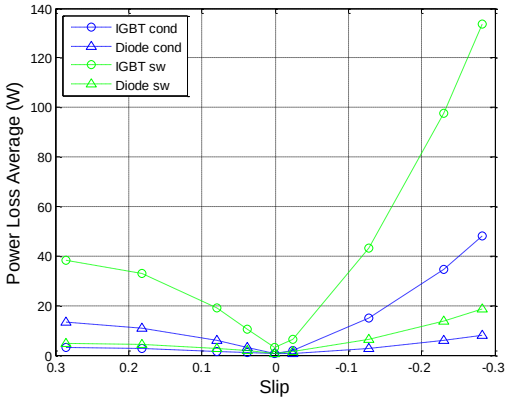

(a) the Grid Side Converter

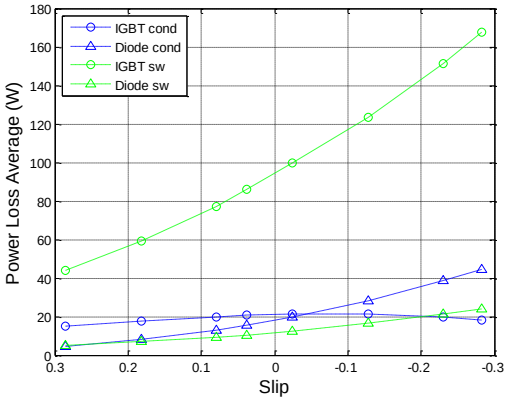

(b) for the Rotor Side Converter

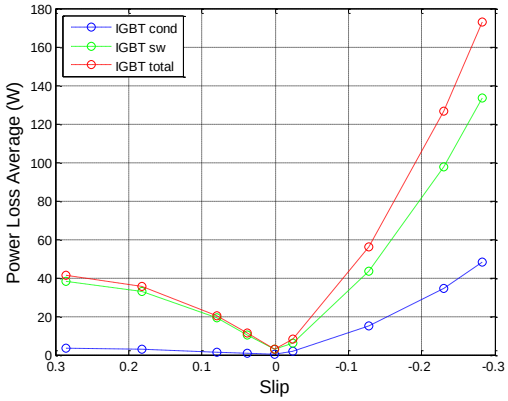

(c) Grid Side IGBT

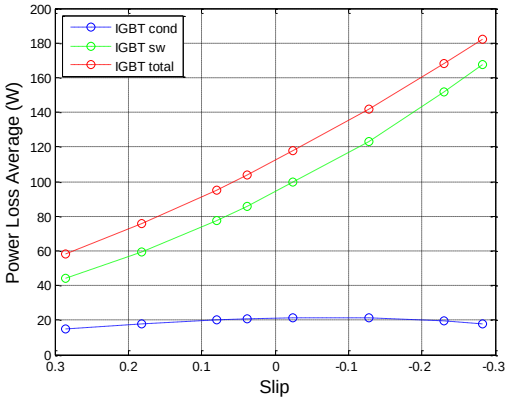

(d) Rotor Side IGBT

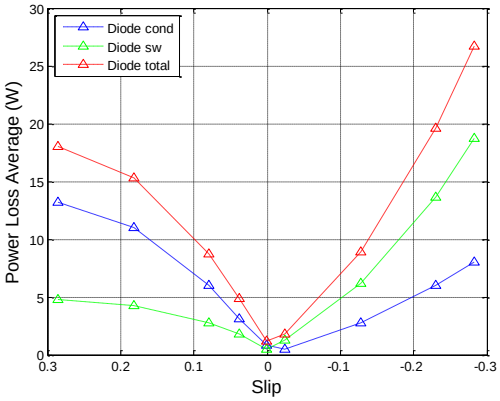

(e) Grid Side Diode

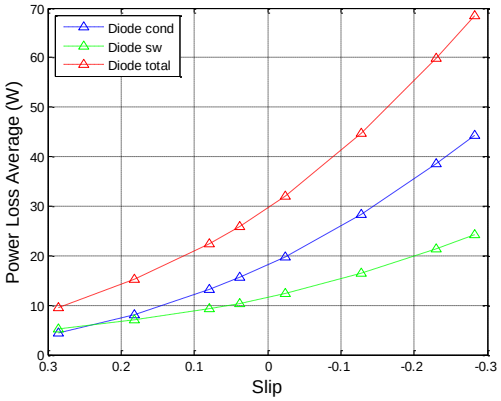

(f) Rotor Side Diode

Figure 6-8 Average Power loss vs Slip

As can be seen from Figure 6-8 (a) and (b) the power loss is dominated by the IGBT switching loss. The relative influence of the other sources of loss; IGBT conduction loss, diode switching loss and diode conduction loss, depend upon the operating point and more specifically whether the machine is in subsynchronous or supersynchronous mode. The magnitude of the IGBT switching loss does, of course, also depend on the operating point.

It can be seen from Figure 6-8 (c) and (d) that the IGBT switching loss is significantly larger than the conduction loss for both rotor and grid side converters. The diode total loss for the grid side converter is mainly conduction loss at subsynchronous speed and above synchronous mainly switching loss. For the rotor side converter the total diode loss is dominated by the conduction loss. The grid side IGBT conduction loss follows a similar variation to the switching loss (Figure 6-8 (c)) however the rotor side IGBT conduction loss seems to peak at or just above synchronous speed (Figure 6-8 (d)).

The rotor side converter operates in rectifying mode at higher speeds as power is taken off the rotor so in this operating region a drop in the rotor IGBT conduction loss is expected, the current instead flowing mainly through the diode. This in fact can be seen if the rotor side loss profiles for the conduction loss at exemplar subsynchronous and supersynchronous operating speeds are examined.

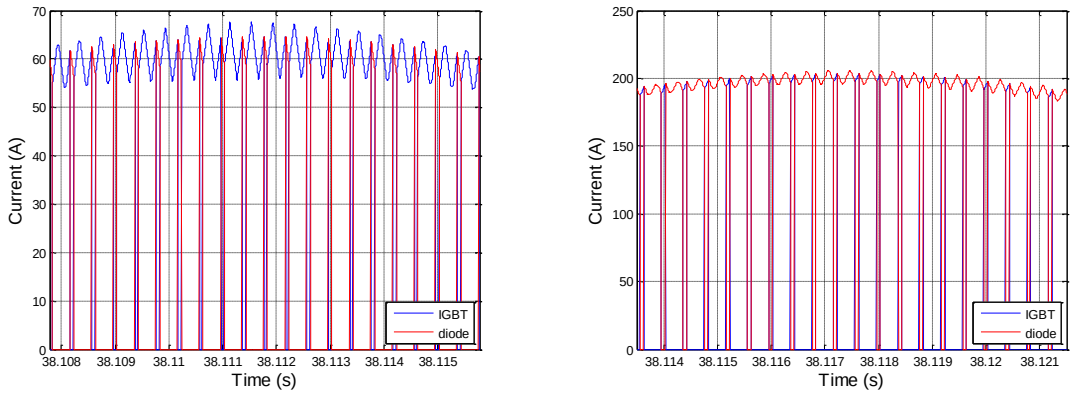

(a) Slip≈0.3 **(b) Slip≈-0.3**

Figure 6-9 Rotor IGBT and diode current

Two operating modes of the rotor side converter can be distinguished in Figure 6-9. At subsynchronous speed as shown in Figure 6-9 (a) the IGBT carries the current for the majority of the duty cycle as power flows to the rotor whereas above synchronous speed the diodes are

conducting for longer (Figure 6-9 (b)) as the converter rectifies the rotor current to charge the dc-link capacitor.

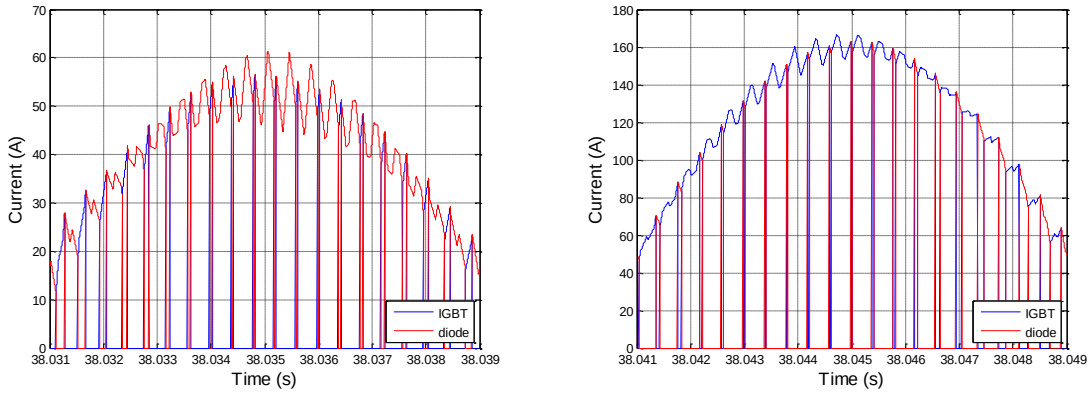

(a) Slip≈0.3 **(b) Slip≈-0.3**

Figure 6-10 Rotor IGBT and diode current

The opposite characteristic is displayed by the grid side converter, which has its IGBTs carrying current for the majority of the time at subsynchronous speed and the diode at supersynchronous speed (Figure 6-9 (b)).

Figure 6-9 and Figure 6-10 merely show that the phase angle between the current and the fundamental component of the converter output voltage is 180° shifted either side of the synchronous operating point. This is trivial if it is considered that the real power flow has to reverse when synchronous speed is reached.

Rotor Side Loss

To examine how the loss characteristic varies between IGBT and diode it is useful to redraw the plots in Figure 6-8 with both device losses on one set of axes.

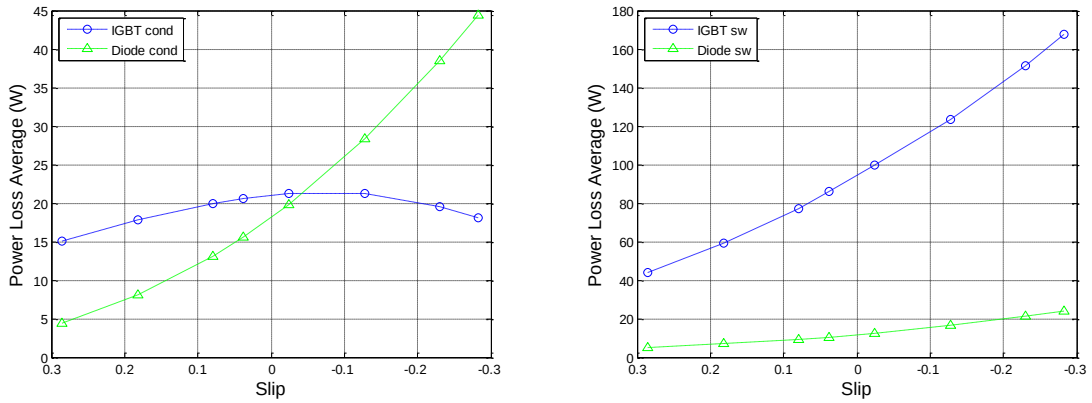

(a) Conduction Side Converter **(b) Switching Side Converter**

Figure 6-11 Average Rotor Power Loss vs Slip

The conduction loss of both IGBT and diode are influenced by two factors, these being phase angle as discussed above, and the magnitude of the current flowing. As shown in Figure 6-3 (a) the rotor current increases with machine speed and the phase angle shift means that above synchronous speed the IGBTs are conducting for much less time when the current is high. Thus the conduction loss does not continue to increase after synchronous speed (Figure 6-11 (a)). The diode conduction loss however increases across the full speed range; at subsynchronous speed the diode is conducting during the time when the current is high but the increasing rotor current trend with speed means that conduction loss increases. Above synchronous speed the phase angle changes so that the diode now conducts the current at the high part of the fundamental cycle thus the conduction loss continues to rise with speed (Figure 6-11 (a)). The switching loss for both devices increases across the full range of speeds, following the current variation. The loss when a device switches is independent of the time the switch remains in the state it switches to: even if the pulse is very narrow the loss dissipated will still only depend on the current and the dc-link voltage (which is controlled to be constant).

Grid Side Loss

A similar analysis for the grid side losses may be done.

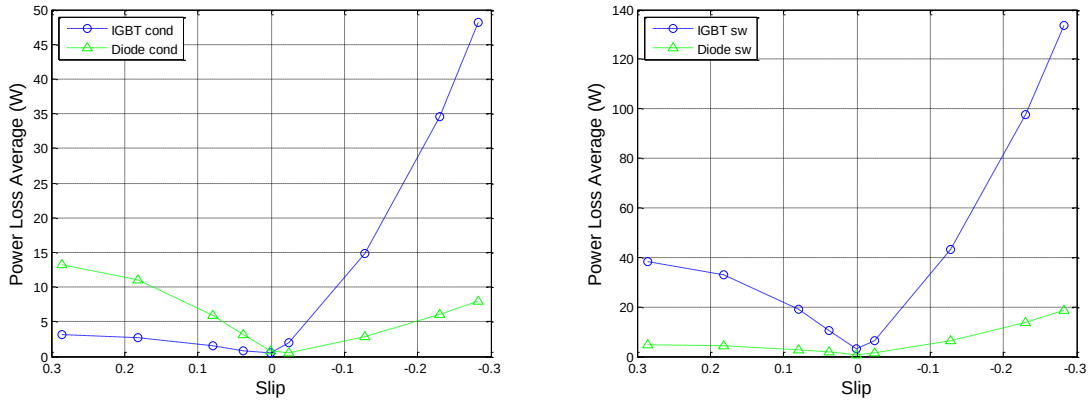

(a) Conduction Loss **(b) Switching Loss**

Figure 6-12 Average Grid Side Power Loss vs Slip

The grid side conduction loss follows the grid side current (Figure 6-4). At subsynchronous speeds the diode is conducting the current for the majority of the duty cycle and thus dissipates a larger loss. This is reversed above synchronous speed where the IGBT conducts the current for longer and thus has a larger loss. The switching loss again follows the current variation.

To summarise the power loss results it may be noted that the power loss characteristics are driven by two factors; the current variation with wind speed and the operating mode of the converter (inverter/rectifier). The latter has bearing upon the relative sharing of the current between IGBT and diode.

So it is seen that the grid side power losses all have the same variation with wind speed as the current. The relative contribution to the total loss from conduction and switching losses changes as the converter moves from inverter to rectifier mode. Due to the specific loss characteristics of the diode this effect is enough to mean that the switching loss becomes dominant above synchronous speed whereas the conduction loss dominates the diodes loss below synchronous speed. The switching loss for the IGBT is larger than the diode switching loss and so dominates the IGBT loss across all speeds.

On the rotor side, again the current vs wind speed characteristic is followed but the IGBT conduction loss can be seen to fall off above synchronous speed as the converter enters rectifier mode. The

IGBT switching loss continues to rise as the IGBT current is rising with wind speed; the fact that the IGBT conducts for shorter pulses as wind speed increases does not affect the switching loss but, of course, is the very reason the IGBT conduction loss drops off. At subsynchronous speed the converter is in inverter mode and so the diode conduction loss is low. As wind speed increases the current through the diode increases, above synchronous speed the diode conducts more and so the conduction loss dominates.

6.3. Temperature Cycling Results

The power loss within each device oscillates at the fundamental frequency of the current, and each device is active for one half cycle before being in the OFF state for the following half cycle. The temperature of each device oscillates about a mean temperature (when steady state is reached) at a frequency equal to that of the electrical frequency. This changes with operating point for the rotor side devices but is fixed at 50Hz for the grid side devices (Figure 6-13).

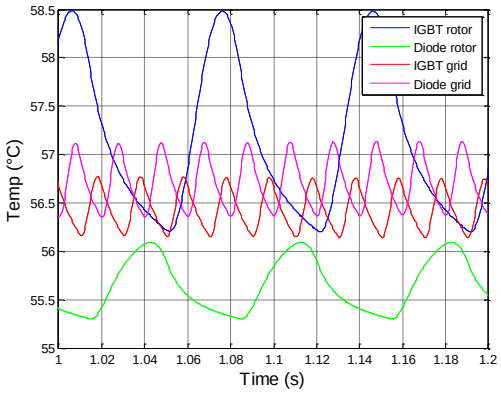

(a) Wind Speed = 7ms^{-1}

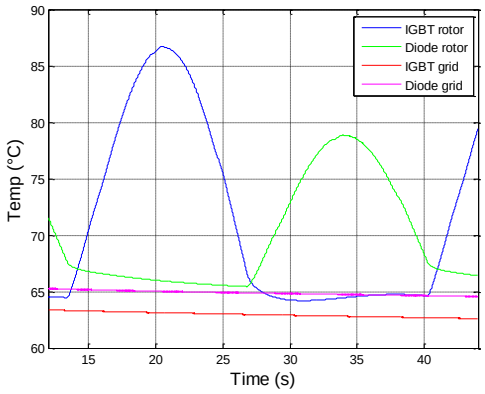

(b) Wind Speed = 9.755ms^{-1}

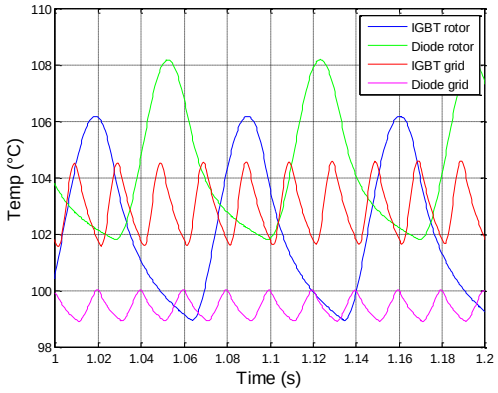

(c) Wind Speed = 12.5ms^{-1}

Figure 6-13 Grid Side and Rotor Side IGBT and Diode Junction Temperature

The temperature variation may be said to be characterised by three qualities; the mean temperature (T_{j_mean}), the change in temperature within each temperature cycle (ΔT_j) and the frequency of the temperature cycles.

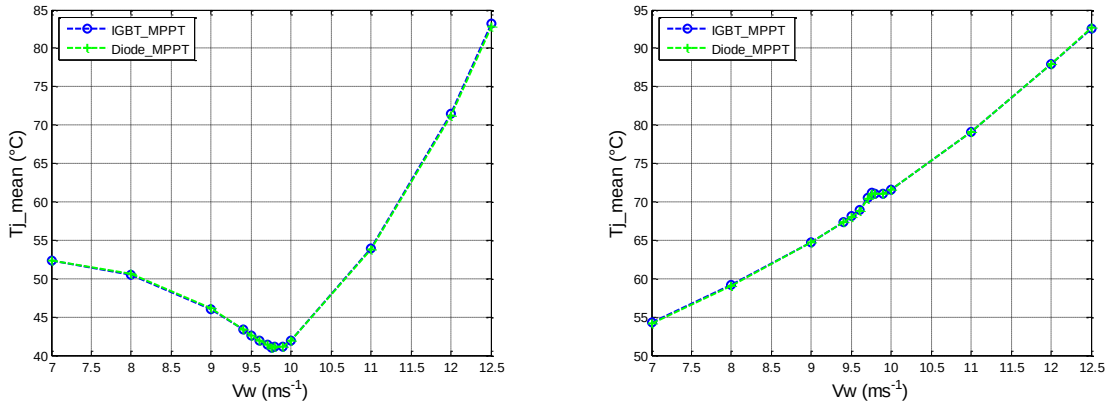

(a) Grid Side Converter **(b) Rotor Side Converter**

Figure 6-14 Mean junction temperature

The mean temperature is driven by the average power loss and the fundamental frequency of the power loss variation. The grid side mean junction temperature follows the power loss and so moves towards zero at synchronous speed where the mean power loss was lowest. Moving away from this operating point entails greater loss and so a higher temperature. (Figure 6-14 (a)). The rotor side mean temperatures rises across the full range of operating speeds (Figure 6-14 (b)).

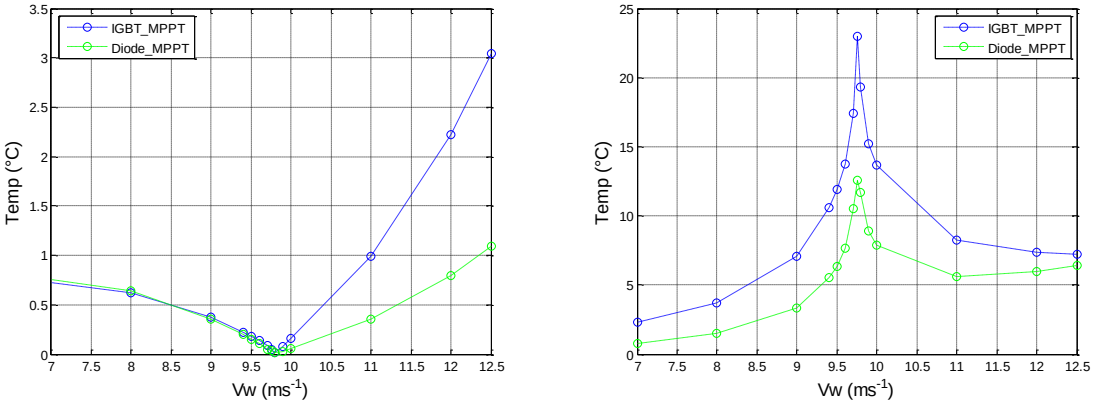

(a) Grid Side Converter **(b) Rotor Side Converter**

Figure 6-15 Temperature cycle magnitude vs Wind Speed

The magnitude of the temperature cycles depends on the power loss, electrical frequency and the thermal impedance. The grid side devices ΔT_j follow the variation of the power losses (Figure 6-15 (a)), as the frequency is unchanging with operating point. The rotor side power losses vary in fundamental frequency and so the ΔT_j results reflect this (Figure 6-15 (b)). The frequency being low at synchronous speed means that the thermal impedance is higher and so is the ΔT_j. And as the frequency will go to zero at exactly synchronous speed then the thermal impedance becomes the dominating factor at this operating point.

The response of the thermal circuit for a module was assessed by calculating the IGBT junction to casing thermal impedance at a range of frequencies. The casing temperature is assumed constant (this assumption is justified below).

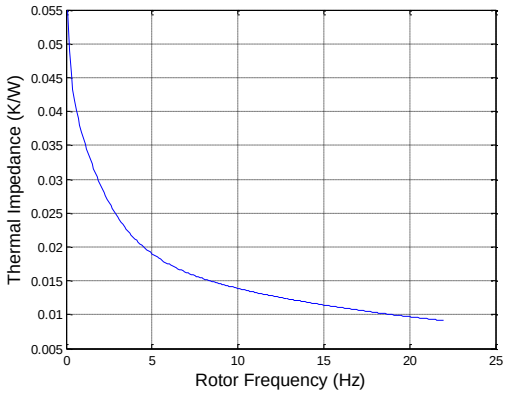

Figure 6-16 Thermal Impedance vs Rotor Frequency

There is clearly a high sensitivity at frequencies below 5Hz and beyond this range the impedance has dropped off considerably (Figure 6-16). The peak of ΔT_j in the rotor temperature results (Figure 6-15 (b)) occurs between wind speeds of 9 and 11 ms^{-1} which correspond to temperature cycling frequencies of 4.39 and 6.35 Hz respectively. The maximum value itself will occur at 0Hz but its peak extends out as far as around 5Hz either side of the maximum.

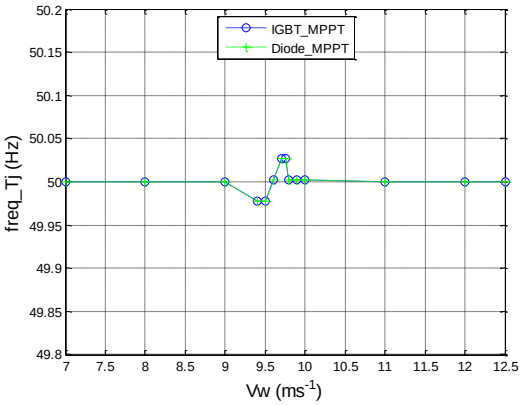

(a) Grid Side Converter

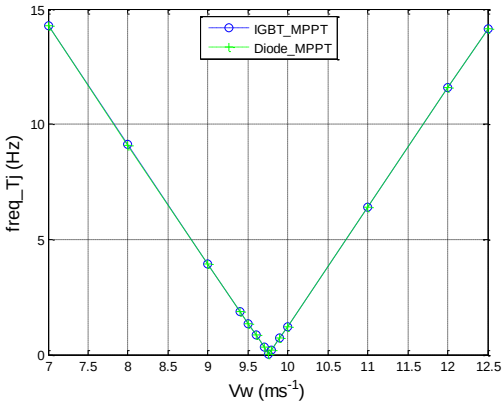

(b) Rotor Side Converter

Figure 6-17 Frequency of Temperature Cycling vs Wind Speed

The frequency of the temperature cycles is the same as the electrical frequency. This may seem trivial but is not necessarily so. The power loss that arrives at the casing-heat sink interface from each of the four modules on the heat sink has a frequency that is double that of the electrical frequency. The upper IGBT, say, will conduct for half a cycle before the lower IGBT conducts for the second half the cycle. As the upper and lower switches within each module are thermally connected at the casing it might be expected that the temperature of the devices would follow the sum of the loss from the devices, as heat flows from one device to another as well as to the heat sink. This is not the case however, the dominant path for heat excursion is directly out from the junction to ambient via the heat sink and the temperature oscillation is dominated by the electrical frequency. An upper device junction emits a half cycle of power loss followed by a period of no loss and although its partner device in the same leg emits power loss during this no loss period this does not warm the junction of the upper device by any noticeable amount. The casing temperature is steady, that is, it is constant during steady state wind conditions, the junction to casing thermal capacitance having smoothed out the temperature oscillation experienced by the junction.

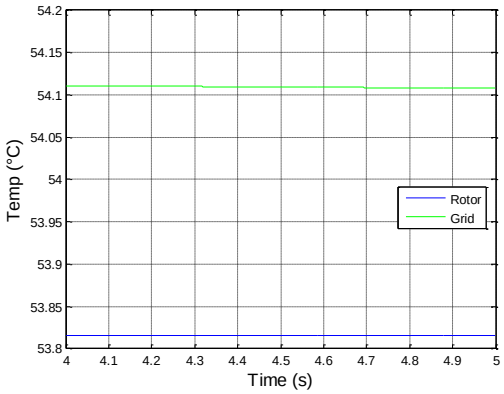

(a) Wind Speed = 7ms^{-1}

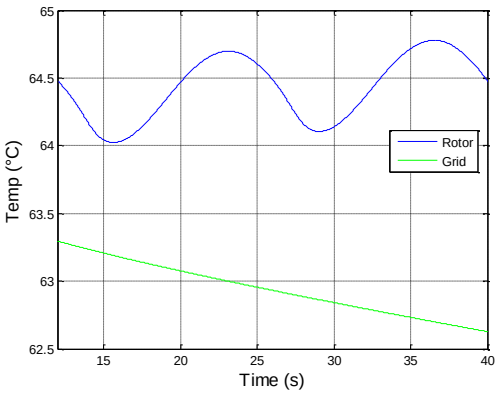

(b) Wind Speed = 9.755ms^{-1}

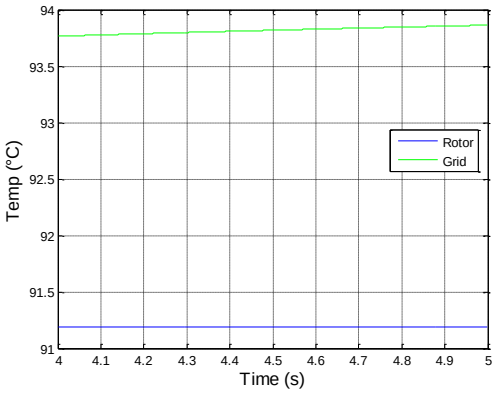

(c) Wind Speed = 12.5ms^{-1}

Figure 6-18 Reference Point (casing) Temperature

The exception to this is found at operation close to synchronous speed (ie for electrical frequencies less than approx. 2Hz), where the casing temperature is observed to oscillate at twice the frequency of the power loss; it is in this case following the combined loss from the upper and lower devices (Figure 6-18).

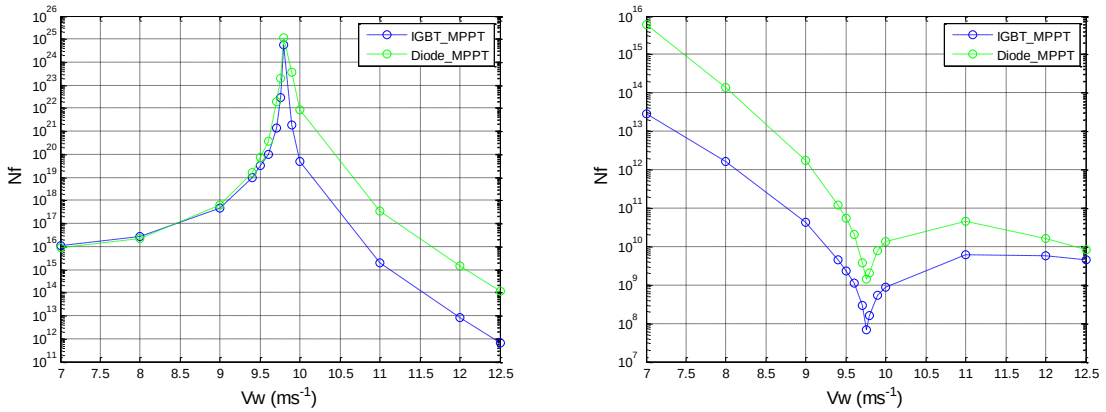

(a) Grid Side Converter **(b) Rotor Side Converter**

Figure 6-19 Number of Cycles to Device Failure vs Wind Speed

The number of cycles to failure (N_f) depends on the mean temperature and the magnitude of the temperature cycles. The grid side converter has very low ΔT_j at synchronous speed and so the N_f is highest at this point (Figure 6-19 (a)). The higher mean temperature dominates at high speeds and N_f falls off. The rotor side N_f follows the trend of the mean temperature, in that the higher more damaging temperatures at high speeds mean that the number of cycles before failure falls as the wind speed increases (Figure 6-19 (b)). A dip in this general trend is observed at synchronous speed where the high magnitude of ΔT_j starts to dominate.

These plots of N_f are easily converted into lifetime plots by factoring in the period of each cycle.

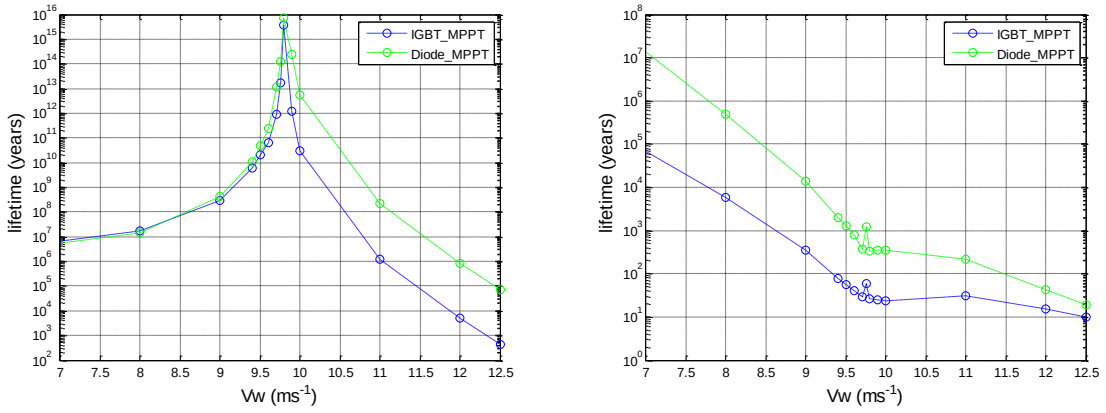

(a) Grid Side Converter **(b) Rotor Side Converter**

Figure 6-20 Lifetime vs Wind Speed

The grid side lifetime plot has the same shape as the grid side plot of cycles to failure as, the grid temperature cycling frequency is constant (Figure 6-20 (a)). The rotor side lifetime plot follows the same general shape as the N_f plot but the spike at synchronous speed is reduced in severity as the periods of the cycles around this point are very large so the low values of N_f do not necessarily correspond to a low lifetime (Figure 6-20 (a)).

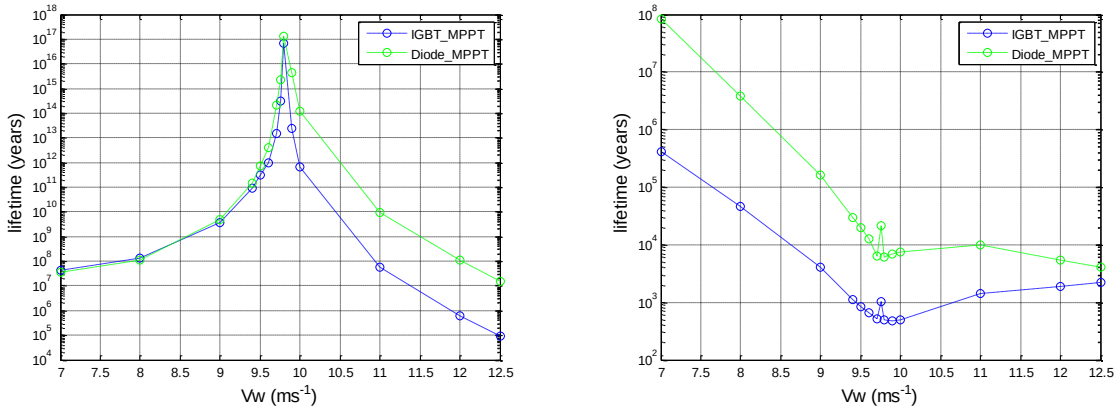

(a) Grid Side Converter **(b) Rotor Side Converter**

Figure 6-21 Lifetime vs Wind Speed adjusted by probability of Wind Speeds

Figure 6-21 shows the lifetime results weighted by the probability of the individual wind speeds. The high significance of the high wind speed region for the rotor plot is reduced by taking into account the fact that these wind speeds are less probable. The near synchronous region is clearly seen to be the most damaging operating region. The accumulated damage can be represented by a plot of lifetime consumption (Figure 6-22) which is simply the inverse of the Weibull adjusted plot.

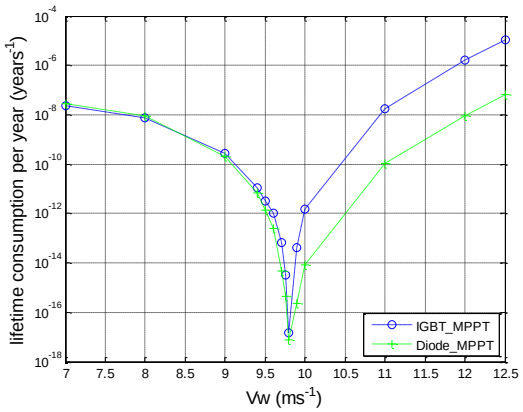

(a) Grid Side Converter

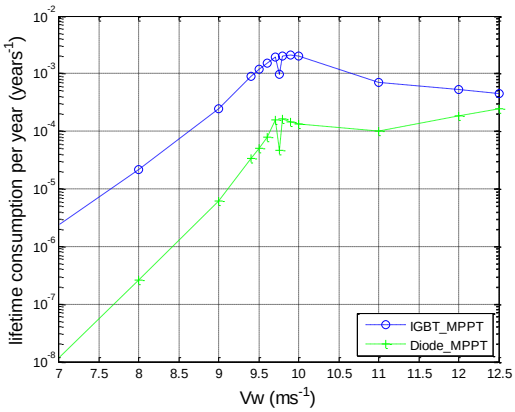

(b) Rotor Side Converter

Figure 6-22 Lifetime consumption per year vs Wind Speed

6.4. Summary

Steady state wind conditions were simulated and power loss results obtained. The power loss results are dominated by IGBT switching loss. The device power losses obey a similar relationship with wind speed to that followed by the current; the conduction losses are also dependant on the phase angle between converter voltage and current which undergoes a 180° shift when the synchronous speed operating point is crossed.

Temperature results show that the main flow of heat is directly out from the junction to the ambient environment. The casing temperature remains constant at steady wind conditions, except when close to the synchronous operating point (ie for electrical frequencies less than approx. 2Hz), where there is small magnitude oscillation driven by the combined power loss from the upper and lower devices on each module. Mean temperature, being driven by the average power loss, increases with wind speed whilst temperature cycling magnitude varies with the power loss and frequency. At synchronous speed the frequency becomes the dominant factor influencing the magnitude of the temperature cycling.

The number of cycles to failure is determined and shown to be lowest for the rotor side IGBT at synchronous speed. The grid side devices have a much higher number of cycles to failure. Lifetimes are predicted and shown to be shortest at synchronous speed and above for the diode and for the IGBT the minimum lifetime is at or near the synchronous point.

Chapter 7. **Steady State Simulation Modified MPPT**

Chapter 6 outlined the fact that the damage done to the converter as a result of thermal cycling depended upon the operating point at which the WT was at. The low frequency cycles occurring at synchronous speed appear to have a significant effect in reducing the converter lifetime; an effect which is not encountered by the grid side converter due to the fact that it operates at a single frequency, this being the grid frequency.

A modified control approach which avoids operating the rotor side converter at low frequencies so as to mitigate the damage done by temperature cycling is suggested here as a means to extend the lifetime of the rotor side converter. This extended life comes at a cost to energy capture from the WT as any change to the control algorithm necessarily implies a move away from the MPPT curve, which allows the maximum capture of energy.

The region of concern for the rotor converter is very close to synchronous speed. The thermal impedance shows greatest sensitivity to frequency, for frequencies less than 5 Hz. The spike in the plot of rotor ΔT_j vs wind speed (Figure 6-15) was at around ±0.1 slip, which implies an operating frequency of around 5 Hz or less. Operating points are selected which bound this damaging region of operation. These are defined as ±4% of the synchronous speed. The proposed novel control adaptation replaces a small region of Torque vs Speed curve for MPPT with a linear region of negative gradient. If the WT enters this region then the mismatch between machine's electromagnetic torque and the mechanical torque from the blades will cause the system to accelerate across the forbidden zone thus avoiding operation at low frequencies.

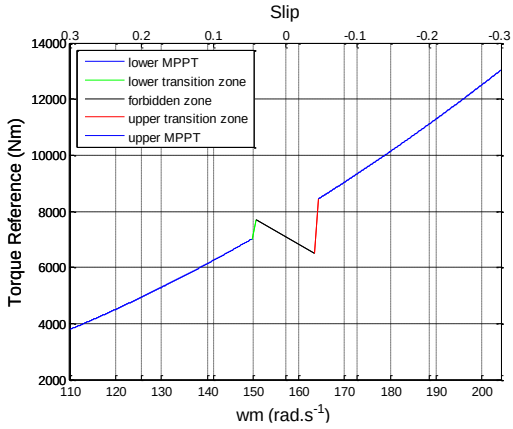

Figure 7-1 Torque vs Speed and Slip for, MPPT with control adaptation

To substitute a linear torque vs speed characteristic of negative gradient at a particular section in the MPPT torque curve requires at least one intermediate section that will allow a smooth transition between the two characteristics. As can be seen in Figure 7-1 two positive gradient linear regions are inserted to ensure a continuous plot. These are designated the *lower transition zone* and the *upper transition zone*. The central zone sandwiched between these and containing the synchronous operating point will be referred to as the *forbidden zone*.

7.1. Operation of modified MPPT control Algorithm

7.1.1. The Power Characteristic

In normal operation of a WT, the controller will respond to a change in wind speed signalled by an increase or decrease in the rotor speed by altering the electromagnetic torque to the value which keeps the system on the MPPT curve. In this way the WT's output is maintained at its maximum for a particular speed.

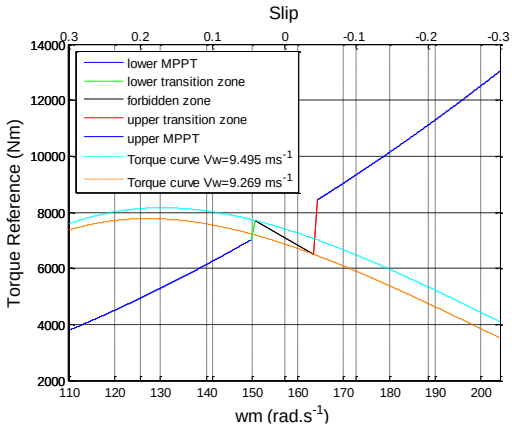

Figure 7-2 Torque vs Rotor Speed and Slip for modified control algorithm.

The modification made to this MPPT curve means that as the wind speed increases from the lower MPPT region it will cause the turbine to enter the lower transition zone. This can be understood by considering Figure 7-2. The stable operating points occur where the wind curves bisect the Torque Reference control curve, at these points the electromagnetic torque from the machine should be equal to the torque from the blades (on the machine side of the gearbox). If the wind increases, from zero, until the orange wind speed (V_w=9.269 ms^{-1}) curve is reached then the system will accelerate along the MPPT curve (blue) and then up along the lower transitional zone (green). Further increase in the wind will cause the system to move along the lower transitional zone until

a wind speed of V_w=9.495 ms^{-1} is reached (cyan curve). At this point the system will accelerate (as the mechanical torque is in excess of the electromagnetic torque, as set by the controller) across the forbidden zone. As the system accelerates and the mechanical torque thus follows the cyan curve, the electromagnetic torque is controlled to remain at a lower value and in fact across the forbidden zone the machine torque falls at a greater rate than the mechanical torque. The next stable operating point is reached at the intersection of the V_w=9.495ms^{-1} curve and the upper transitional zone. At this point a drop in the wind speed back below 9.495ms^{-1} will not return the WT back to the low transitional zone. The steep gradient of the forbidden zone ensures that the after transiting the forbidden zone the system is now approximately one third of the way up the upper transitional zone (red). A return to the low speed side of the forbidden zone requires that the wind reduces to 9.269 ms^{-1}.

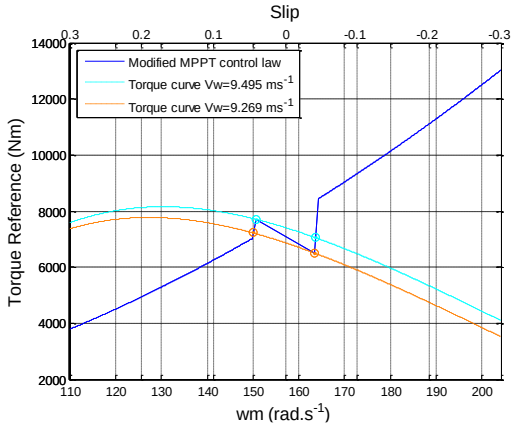

Figure 7-3 Torque vs Rotor Speed and Slip for modified control algorithm

Figure 7-3 shows the modified control algorithm along with the critical wind curves, again. This time the co-ordinates where the discontinuities between stable operating points occur are highlighted with circles. Between these pairs of points the difference between the machine and mechanical torque increases, meaning that there are no stable operating points at which the WT may operate.

By examining the torque vs wind speed characteristic the hysteresis in the control algorithm is easily seen.

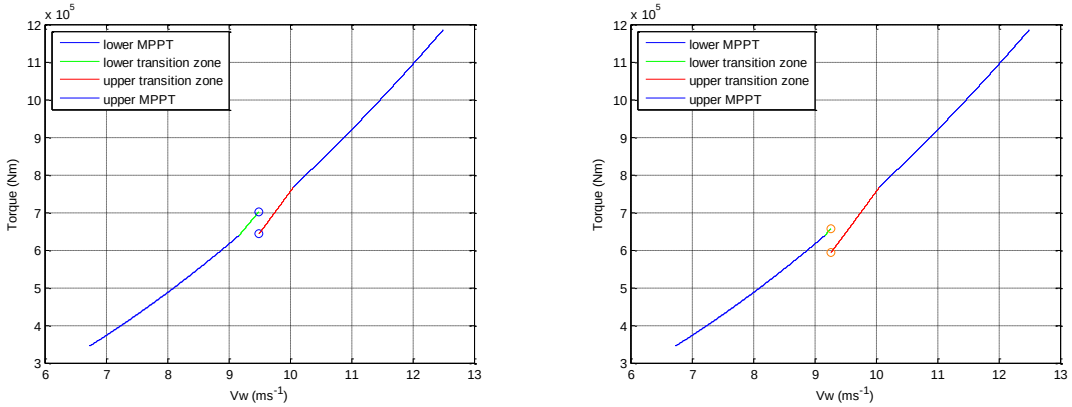

(a) Increasing Scenario **(b) Decreasing Scenario**

Figure 7-4 Torque versus Wind Speed

Figure 7-4 (a) shows the torque variation with wind speed for the case where the wind speed increases from the lower MPPT zone towards and across the forbidden zone. Figure 7-4 (b) shows the decreasing scenario where wind speed decreases from the upper MPPT zone down across the forbidden zone. It can be seen that the upper transitional zone is much larger, in that it covers are more extensive range of wind speeds (it should be noted that Figure 7-4 (b) shows the full upper transitional zone whereas Figure 7-4 (a) only shows the section available after the system has crossed the forbidden zone and arrived part way along the upper transition zone). This means that once the system crosses the forbidden zone (due to an increasing wind), the wind must increase by a larger amount to reach the upper MPPT zone than it must decrease to reach the lower MPPT zone when the crossing is a result of a decrease in wind speed.

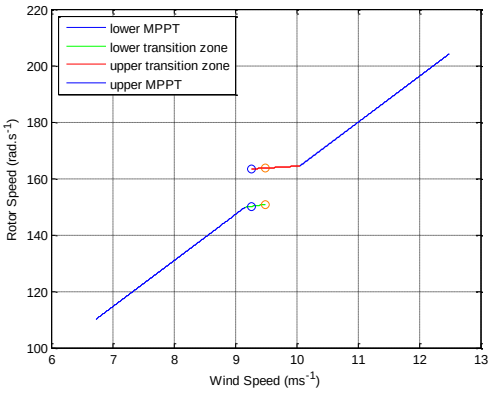

Figure 7-5 Rotor Speed versus Wind Speed

The overlap in wind speeds in the adapted region of the control algorithm is clear in Figure 7-5. So for a small range of wind speed between, 9.269 ms^{-1} and 9.495 ms^{-1} there are two possible rotor speeds depending upon whether the system is in the increasing wind speed or decreasing wind speed scenario. The basic principle of operation of the control algorithm is clearly seen in Figure 7-5, in that the turbine speed is allowed to vary with wind speed until the synchronous region is approached, at which point the rotor speed is held at approximately the same speed until the wind speed is of the correct magnitude to permit operation on the opposite side of the synchronous zone. Figure 7-5 also shows clearly the discontinuity in the speed range. The gap in the rotor speed range (150.80-163.36 $rad.s^{-1}$) contains the speeds close to synchronous which arise when rotor frequencies approach zero. Thus it is clear that these speeds are eliminated.

7.1.2. The Power Characteristic

The adapted power law algorithm has a similar form to that of the torque curve - the MPPT curve represents a cubic relationship rather than the squared form taken by the torque MPPT curve.

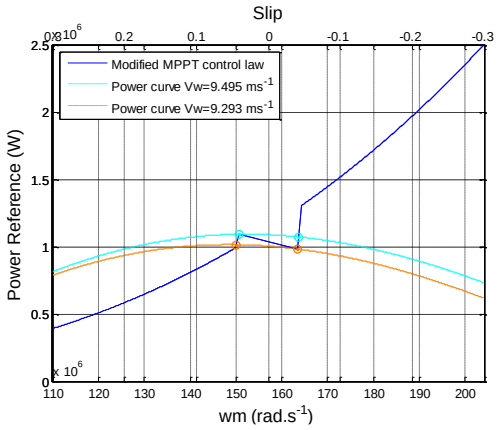

Figure 7-6 Power versus Rotor speed

From Figure 7-6 it may be seen that the Power in the forbidden zone drops off more slowly than in the corresponding torque curve (Figure 7-3). It can also been seen that the power curves for the wind speeds at which the crossings of the forbidden zone occur are intersected by the control curve at values that are still quite close to the maximum power point. This indicates that the power lost in using the adapted control algorithm may not be that great. By examining the variation in power with wind speed it may be seen how far the control adaptations remove the control algorithm from the standard MPPT control.

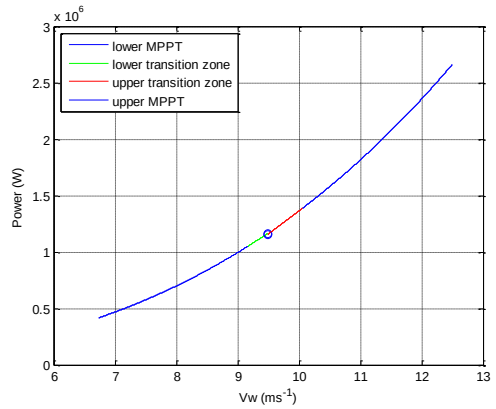

(a) New Control Algorithm for Increasing Scenario

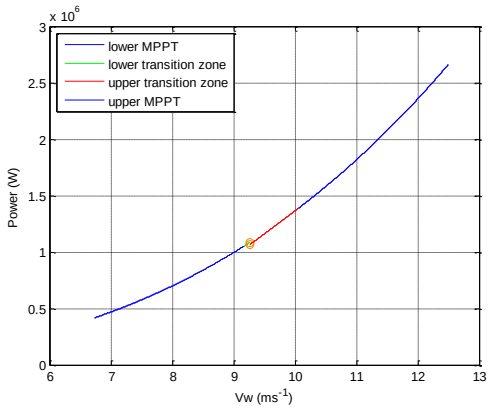

(b) New Control Algorithm for Decreasing Scenario

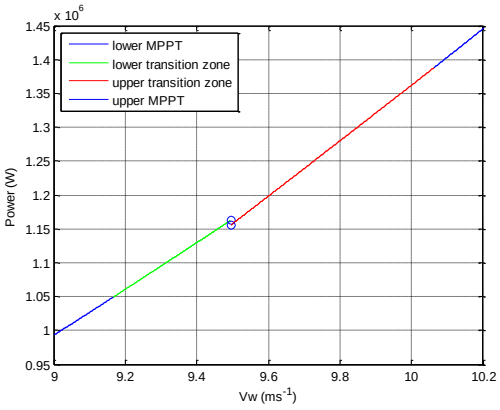

(c) New Control Algorithm for Increasing Scenario in the synchronous region

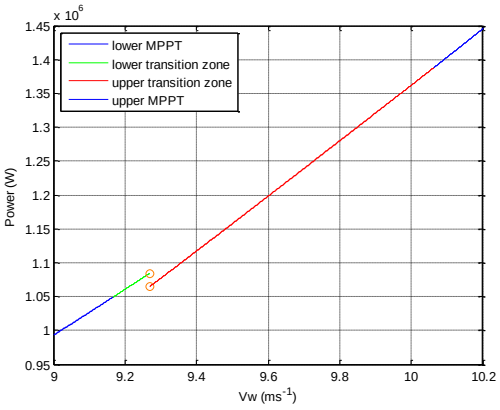

(d) New Control Algorithm for Decreasing Scenario in the synchronous region

Figure 7-7 Power versus Wind Speed

From Figure 7-7 (a) and (b) it can be seen that the general shape of the control curve is close to the MPPT curve. Figure 7-7 (c) and (d) show the linear lower and upper transitional zones. These are not equal as, after the forbidden zone has been crossed, the system will arrive somewhere along the lower/upper transitional zone as opposed to at its end/beginning. Both the transitional zones are below where the MPPT curve would be in this region; as would be expected bearing in mind the MPPT curve represents the control law which ensure optimal power generation.

7.1.3. Power Sacrificed

Power is clearly lost as a result of the control adaptations around the synchronous operating point. This is the cost of the any improvement in reliability that may be gained by adapting the standard MPPT control law.

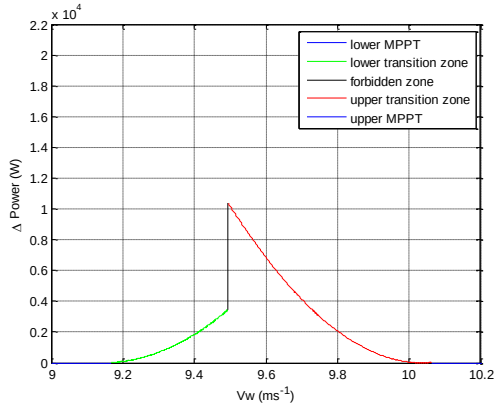

(a) Increasing Scenario

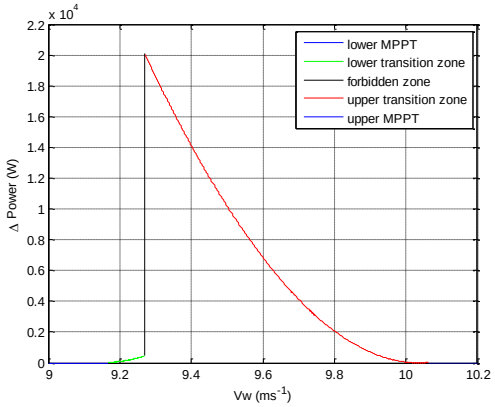

(b) Decreasing Scenario

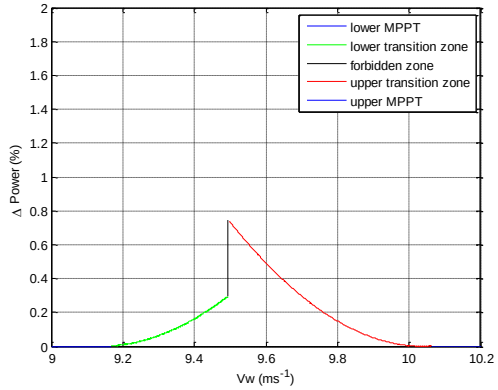

(c) Increasing Scenario Percentage loss

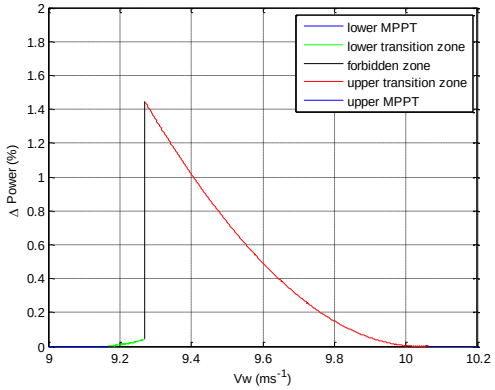

(d) Decreasing Scenario Percentage loss

Figure 7-8 Power Sacrificed vs Wind Speed

The power sacrificed has a maximum value of approximately 20 kW when in the decreasing scenario the lower speed end of the upper transitional zone is reached. This represents a maximum percentage loss of 1.4% of the power generated. As the system approaches this point the power sacrificed rapidly increases and upon crossing the forbidden zone the power sacrificed experiences a large step change, to a very low value (≈0.004% or ≈450W). The maximum power sacrificed for the increasing scenario is 10 kW (≈0.75%). Over the lifetime of the turbine these small power differentials could add up to a sizeable energy loss, however, even in the worst case scenario with the turbine working for long periods in the synchronous region the system will at worst be operating at 98.6% of the optimal performance, as given by MPPT.

7.2. Response of Controller within the Forbidden Zone

While the above plots describe the characteristics of the control adaptation, inasmuch as they detail how the torque and power vary with rotor speed and wind speed they fall short of a full description in that they do not show the response of the system when it is moved into the forbidden zone as a result of an increasing or decreasing wind. The controller operation in the forbidden zone can be observed, for example, by running the system up towards synchronous speed from a low wind speed.

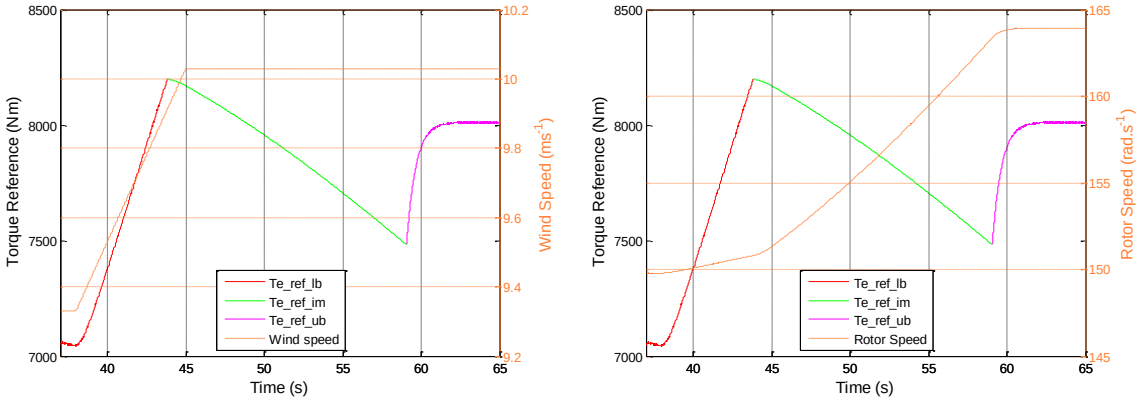

(a) Wind Speed transient **(b) Rotor Speed transient**

Figure 7-9 New Controller Operation in Synchronous Region

The wind speed is increased steadily until the system overtops the lower transitional zone and enters the forbidden zone. The wind speed stops increasing and then remains constant for the remainder of the simulation (Figure 7-9 (a)). In normal operation with a MPPT control law the system would now reach a steady state operating point where the electromagnetic machine torque equalled the mechanical low speed shaft toque from the blades. However, with the present control algorithm the electromagnetic torque now drops off causing the system to accelerate rapidly until the upper transitional zone (Figure 7-9 (b)) is reached. The machine torque then increases with rotor speed until equilibrium is reached between the mechanical and electromagnetic torques. By controlling the machine torque in this way the controller ensures that the forbidden zone is transited in around 10 seconds. Thus the time spent by the WT operating within the low frequency forbidden zone is limited to 10 second intervals that occur only when the top of the lower transitional zone (increasing scenario) or bottom of the upper transitional zone (decreasing scenario) have been reached. It is important to remember that when transiting the forbidden zone the turbine is still producing power, so there is no desperate need for this transit time to be

minimised, so far as the general operation of the WT is concerned. However, the shorter the transit time the less time the rotor side converter will spend operating at the damaging low frequencies and so there is motivation from a reliability standpoint. The swifter the system accelerates through the forbidden zone toward a stable operating point on the opposite side of it, the greater the extent of the oscillation that will occur as the controller tries to re-establish equality between the electromagnetic and mechanical torque. Thus a steady acceleration through the forbidden zone will allow the system to reach a steady state more smoothly without significant speed and torque oscillation.

The speed of the transit of the forbidden zone is determined by the steepness of the forbidden zone in the control algorithm. The larger the gradient the greater the rate of increase in the difference between the electromagnetic torque and the mechanical torque as the forbidden zone is crossed. A steeper forbidden zone will also mean that the power sacrificed will increase. Thus a balancing act is required, where the reliability risk posed by a longer crossing time and thus increased time spent operating at low frequencies of the forbidden zone is weighed up against the need to avoid a rapid crossing which would result in torque oscillations and also a greater shedding of power.

The forbidden zone selected had the lowest possible gradient that still ensured the critical wind curve for the decreasing scenario (9.269 ms^{-1}) was, in its entirety, under the forbidden zone. At the high speed end of the forbidden zone the wind curve at (9.269 ms^{-1}) has a steeper gradient. The forbidden zone's gradient is thus set by this local value as it must be at all times be steeper than the wind curves that cause the transit of the zone.

The time taken for the transit of the forbidden zone at this gradient is not excessive (10s) and so this minimum value is acceptable.

The time constant for the speed control is of the order 2-4s whilst the electromagnetic time constant is considerably shorter. Thus there is no need to be concerned with regards to the interaction between these components of the controller due to the significant difference in response.

7.3. Power loss and Temperature Results

The modification to the standard control algorithm occurs only within a small band within the range of rotor speeds and thus the Power Loss results and their respective temperature profiles are identical safe for this relatively narrow band.

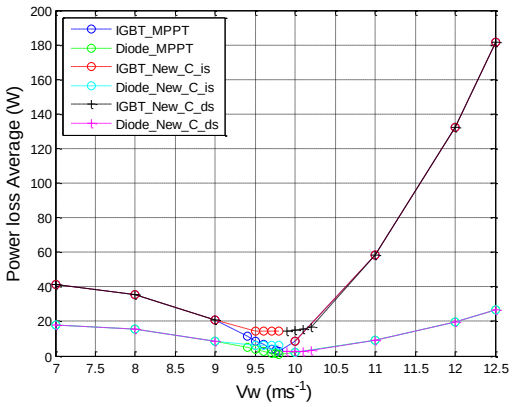

(a) Grid Side

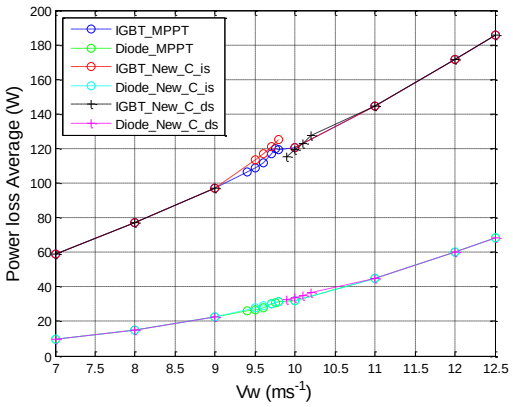

(b) Rotor Side

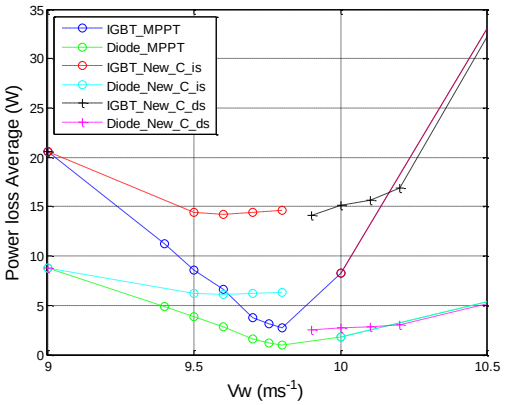

(c) Grid Side, zoomed in

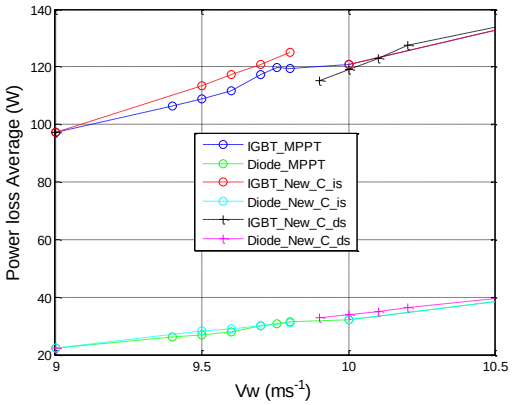

(c) Rotor Side, zoomed in

Figure 7-10 Power loss for IGBT and Diode vs wind speed

Figure 7-10 shows the mean power loss at the junction of both IGBT and diode. It can be seen that the new control regime results in an increase in loss for both devices and in both the grid side and rotor side converters. This occurs in spite of the fact that the power generated by the WT is reduced. To understand why the power loss increases it is useful to look at the value of instantaneous current in the devices.

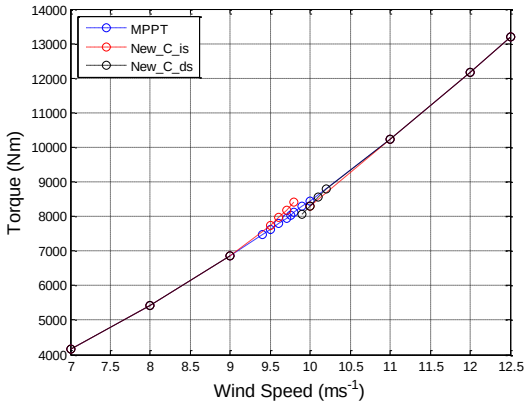

(a) Full Wind Speed range

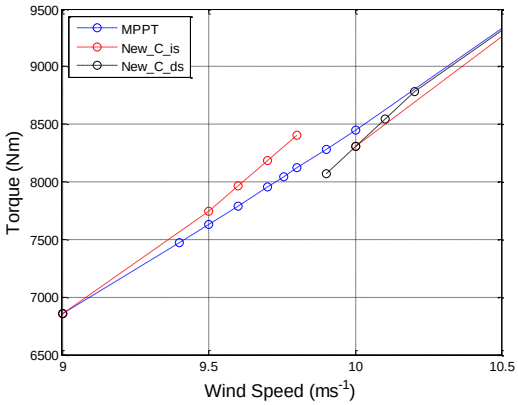

(b) Synchronous Zone Wind Speed range

Figure 7-11 Torque vs Wind Speed

Considering the rotor side converter, from Figure 7-11 it can be seen that the new control algorithm necessitates a higher torque in the lower transitional zone and a lower one in the upper transitional zone. This is as expected from the two plots in Figure 7-4. Indeed with more points plotted around synchronous wind (ie the wind speed that would give rise to synchronous operation under MPPT control) a larger overlap would form just as if Figure 7-4(a) and (b) were superimposed. The higher torque (below synchronous speed) implies a larger value of i_{qr} and since i_{dr} is controlled to be zero (or close to it) then total rotor current must then be higher. Above synchronous speed the torque is lower and thus so is the current.

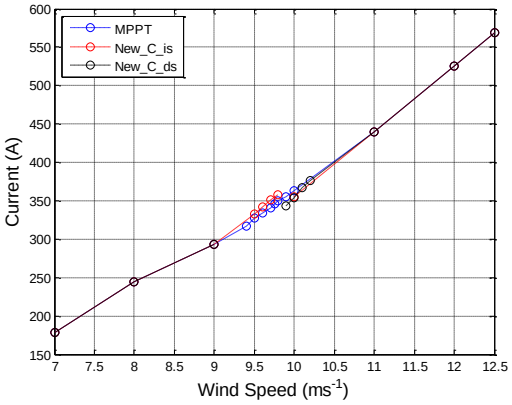

(a) Full Wind Speed range

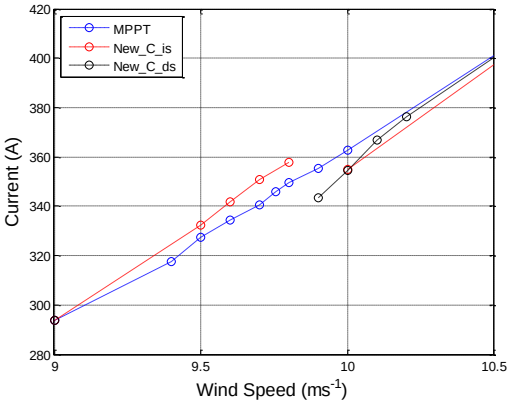

(b) Zoomed in

Figure 7-12 Rotor Current vs Wind Speed

Indeed this is the case, as can be seen from Figure 7-12.

For the case of the grid side power loss (Figure 7-10 (a) and (c)) the power loss is also higher with the new control algorithm than with MPPT control. This can be understood by considering the power flow through the grid side converter.

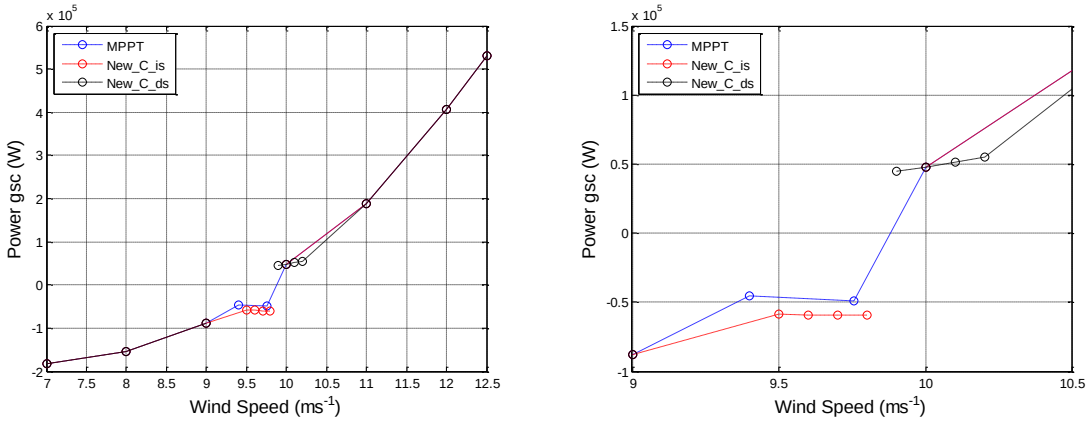

(a) Full Wind Speed range **(b) Zoomed in**

Figure 7-13 Grid Side Converter Power vs Wind Speed

The rotor power falls toward zero at synchronous speed, as is seen in Figure 7-13 for the MPPT case. As the new control algorithm avoids this operating point then the power to/from the rotor is always non-zero. For MPPT the grid converter power is near zero at synchronous speed as the grid side converter current is likewise small.

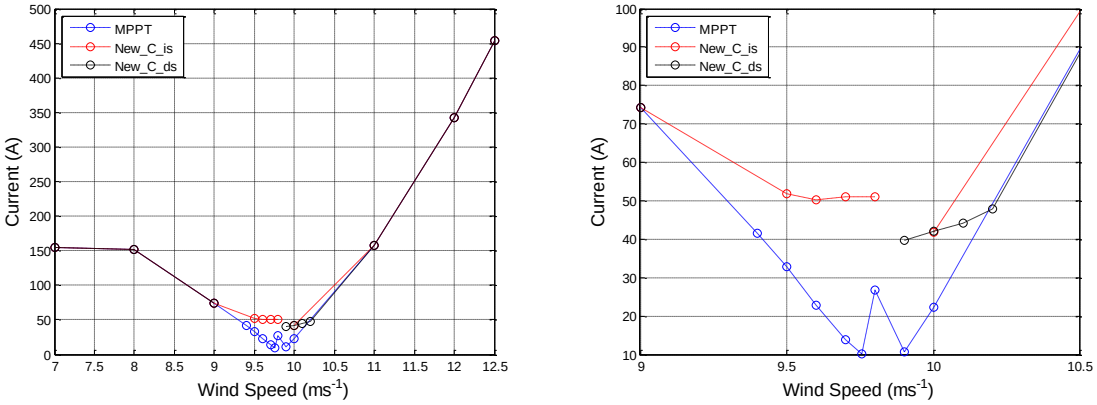

(a) Full Wind Speed range **(b) Zoomed in,**

Figure 7-14 Grid Current vs Wind Speed

For the new control algorithm the current is greater in the wind speed range that defines the synchronous region for MPPT. Hence the loss is increased for the new controller over the MPPT case.

The temperature and lifetime results for the new controller may be compared with MPPT case.

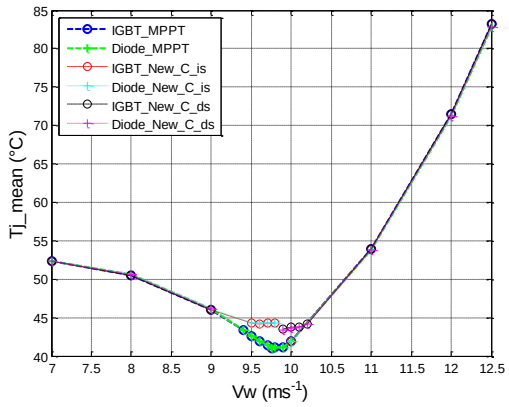

(a) Grid Side

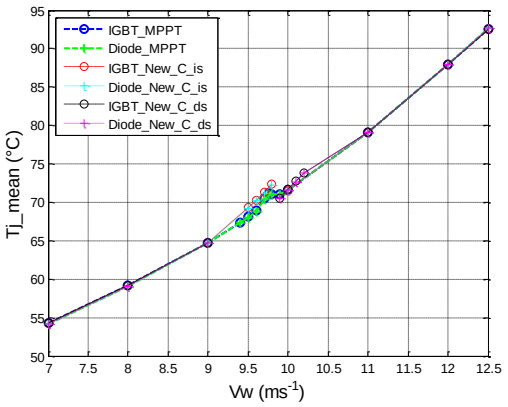

(b) Rotor Side

Figure 7-15 Mean junction temperature

Firstly looking at the mean temperature (Figure 7-15) it can be seen that the variation with wind speed follows that of the mean power loss as expected. The new control algorithm hence results is slightly higher mean temperatures in the synchronous zone. On the grid side this amounts to at most around 4°C and on the and on the rotor side around 2°C.

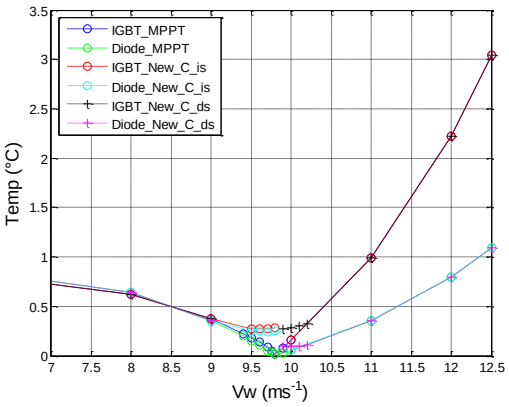

(a) Grid Side

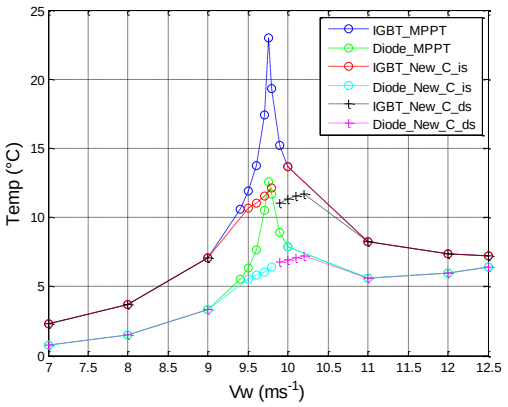

(b) Rotor Side

Figure 7-16 Temperature cycle magnitude vs Wind Speed

As for the size of the temperature cycles, the aim of the controller itself was to mitigate damage on the rotor side by reducing cycle amplitude and indeed the temperature cycles are found to be smaller. Maximum cycle amplitude is reduced from 23°C to 12.25°C (Figure 7-16(b)). This is for the rotor IGBT. The diode's temperature cycle magnitude is reduced from 12.75°C to 6.8°C. The large peak, centred on the synchronous operating point is almost entirely removed. This reduction in the thermal cycling amplitude on the rotor side is paid for, in part, by an increase in the cycling amplitude on the grid side where a the IGBT cycle amplitude increases by a maximum of 0.275°C and a very minor increase in the diode cycling of around 0.1°C (Figure 7-16 (a)).

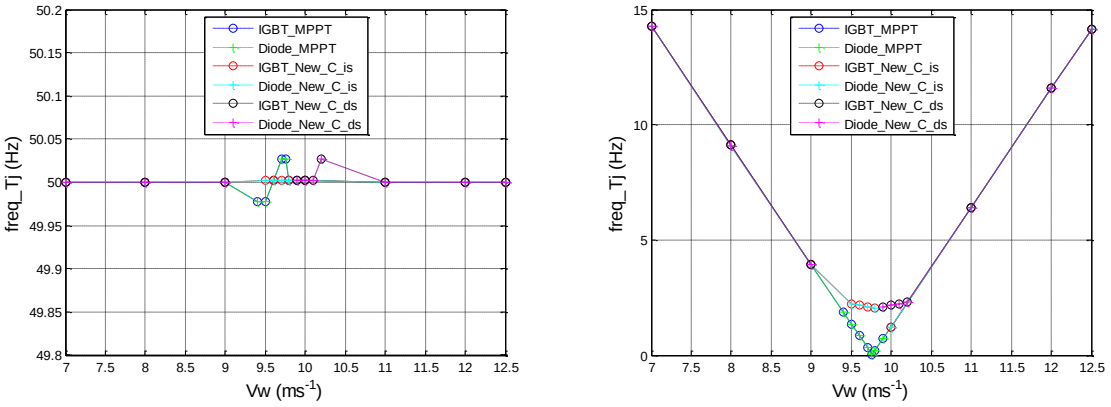

(a) Grid Side **(b) Rotor Side**

Figure 7-17 Frequency of Temperature Cycling vs Wind Speed

The frequency of temperature cycles on the grid side is unaffected (Figure 7-17(a)) by the new control algorithm, as is expected by virtue of the fact that the grid converter frequency remains unchanged at 50Hz. The rotor side frequency plot gives a good indication of the operation of the new control algorithm. The frequency within the wind speed region that would give near-synchronous operation under MPPT is, under the new control algorithm, limited to around 2.5Hz (Figure 7-17(a)).

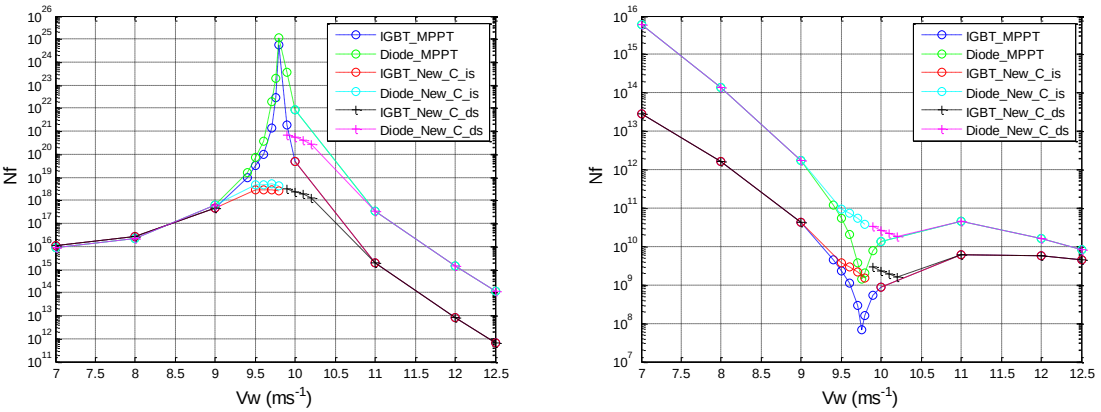

(a) Grid Side **(b) Rotor Side**

Figure 7-18 Number of Cycles to Device Failure vs Wind Speed

The number of cycles to failure is increased in both grid and rotor side converters. The rotor side minimum number of cycles to failure for the IGBT under MPPT was approximately 6.83×10^{7} and under the new control algorithm this is increased to 8.97×10^{8}. For the diode the minimum number of cycles to failure goes from 1.40×10^{9} to 8.4×10^{10} (Figure 7-18(b)).

However the diode plot has a slightly different shape, inasmuch as the minimum value under the new control algorithm occurs at maximum wind speed; at this operating point the mean junction temperature is large enough to cause damage that is greater than that caused at the low frequencies. If the synchronous wind speed region is considered only then the number of cycles to failure can be said to have changed from 1.40×10^{9} to 1.38×10^{10}.

The grid side devices' number of cycles to failure decreases considerably (Figure 7-18(a)), however the values are still high compared to the rotor side devices. Frequency is not a factor here (as the grid side converter is always operating at 50Hz) but even at high wind speed (and thus high mean junction temperature) the number of cycles to failure for the grid side devices are only as low as the rotor values at lower speeds. In other words, the most damaging area of operation for grid side components is only sufficiently damaging to cause damage levels similar to those occurring at low speed in the rotor side converter.

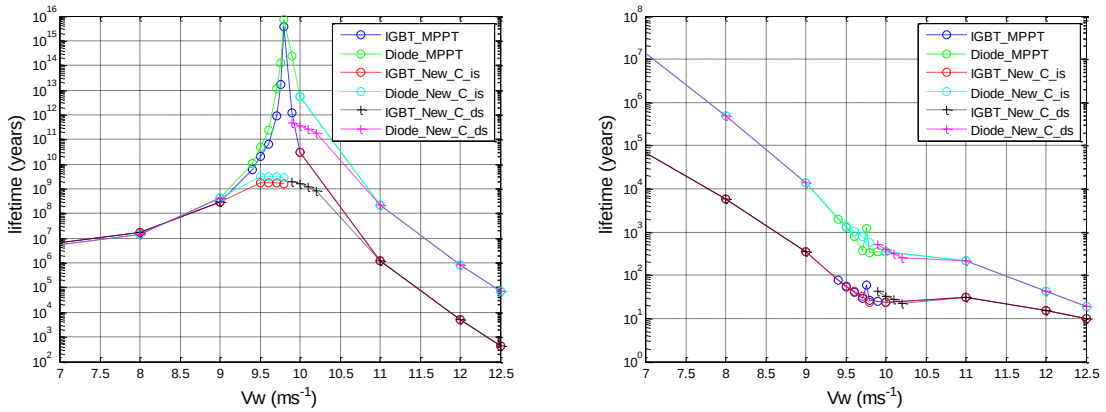

(a) Grid Side **(b) Rotor Side**

Figure 7-19 Lifetime vs Wind Speed

The lifetime improvement is not quite so dramatic, as the time taken per cycle is taken into account but nonetheless a clear increase in lifetime across the synchronous zone may be seen (Figure 7-19(b)) except for at the wind speed that causes synchronous operation under MPPT. Here the period of oscillation is so long that very few cycles occur within a given time period and thus even though the cycle magnitude is larger, the cumulative damage is low under MPPT so for operation very close to synchronous speed (less than approximately 0.2Hz) the lifetimes under both control algorithms are comparable. For the bulk of the synchronous zone, however there is a lifetime improvement. These plots (Figure 7-19) are however for a single speed operation and the real significance of any lifetime plot is improved if the wind distribution is accounted for.

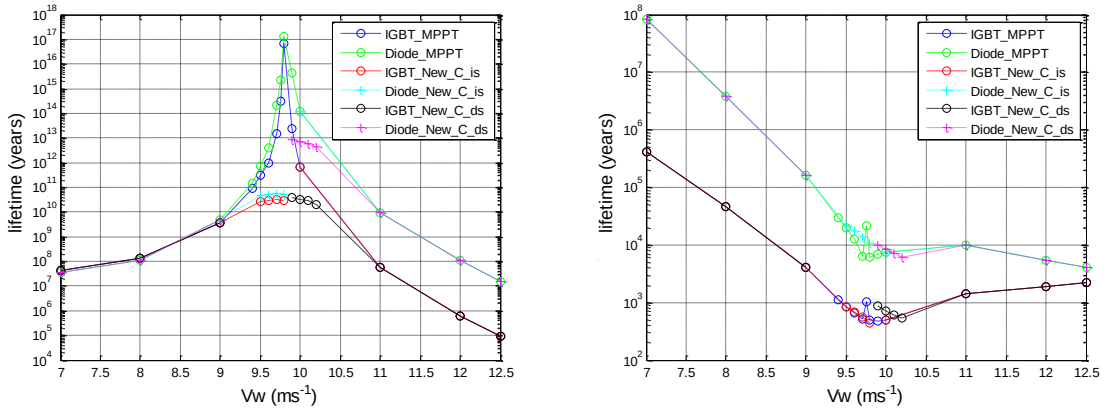

(a) Grid Side **(b) Rotor Side**

Figure 7-20 Weibull adjusted Lifetime vs Wind Speed

Thus the Weibull adjusted lifetimes are shown (Figure 7-20). Here it can be seen that the lifetime improvement is occurring within the more wearing range of frequencies - indeed for the IGBT this is the most damaging region.

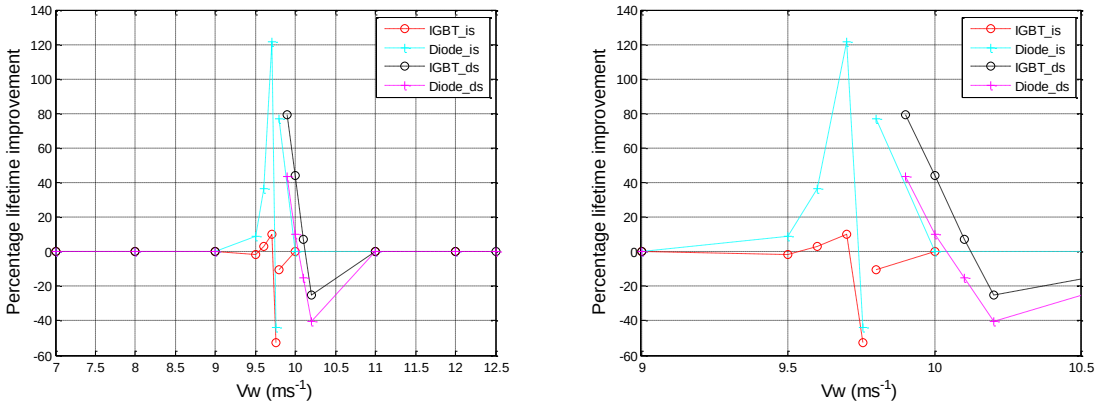

(a) Rotor Side **(b) Rotor Side, zoomed in**

Figure 7-21 Improvement in Lifetime vs Wind Speed

The improvement in lifetime may be plotted against wind speed (Figure 7-21). The distinctive shape of the plot arises from the inclusion of the result at very low frequency. Within a tight band around synchronous speed under MPPT the lifetime increases due to the extremely low number of cycles per minute occurring, thus a `reduction in lifetime arises under the new control algorithm at this speed. Outwith this band, it can be seen that the new control algorithm has a lifetime advantage over MPPT control that peaks for the IGBT at around 80% and for the diode around 120%. This is a significant improvement in lifetime, though the correct interpretation is that the contribution towards lifetime from operation at this wind speed is reduced under the new control approach. More simply put, the damage accumulation at this speed is reduced.

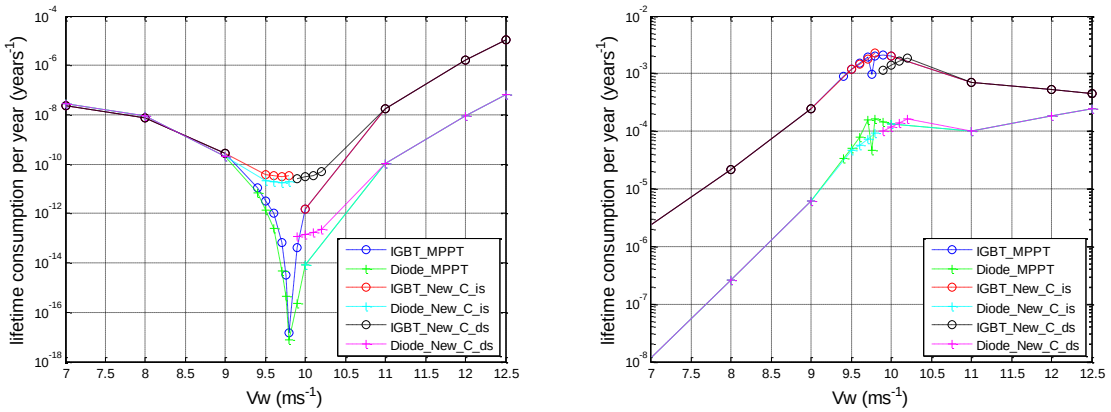

(a) Grid Side **(b) Rotor Side**

Figure 7-22 Lifetime consumption per year vs Wind Speed

As one final way of looking at the lifetime results, a lifetime consumption plot can be made (Figure 7-22). This is the inverse of the Weibull adjusted lifetime plot. The contribution from high speed can be seen to be the largest for both devices, but the new control algorithm targets the synchronous zone, flattening the lifetime consumption curve at wind speeds centred around 9.8 ms^{-1} which leaves the lifetime plot with a linear characteristic on the log plot.

The analysis from simulation has been based upon single wind speed continuous operation and at quasi-steady state (the mean temperature having reached steady state, and superimposed upon this is the thermal cycling). Whilst a useful method of comparing the thermal effects at different operating points, it is evident that there is a secondary and perhaps more obvious form of cycling occurring, i.e. that caused by the variation of the wind with time. The computational effort involved in performing a simulation of long enough duration to examine such wind speed variation is too great for the current model. This would require more time than is available or more suitably a simplified model of the converter that perhaps avoids modelling each switching instance.

As a guide to the effect of wind speed variation, the current set of results may be used to demonstrate the influence on lifetime of the diurnal and turbulent components of the wind speed variation. To model the diurnal variation a representative daytime peak wind and a representative night wind speed were assumed and the lifetime calculation performed based on the mean temperatures determined or these wind speeds in the steady state results and using a period of 24 hours. For the turbulent wind variation, a mean junction temperature was set using the value determined at a particular wind speed (e.g. 8 ms^{-1}) then the upper and lower bounds of the temperature cycling were set by using the mean junction temperatures from the simulations at

wind speeds at 1 ms^{-1} above and below (e.g. 7 and 9 ms^{-1}). This is used as a guide to determining the effect of turbulence derived thermal cycling. In reality the wind speed oscillation (ie the magnitude of the turbulence) would increase with wind speed (in the current work turbulence of ± 1 ms^{-1} is assumed). The scale of turbulence here is however relatively large and so can be used as a worst case scenario (at least in the frequency range of interest - very high turbulence could arise at high wind speed) to judge the effect of turbulence. The lifetime is calculated for the turbulent conditions based upon a period of one minute (turbulence would be increasingly damped by the inertia of the wind turbine as the frequency increased). Both periods are taken from the van der hoven spectrum of wind speed variation [8].

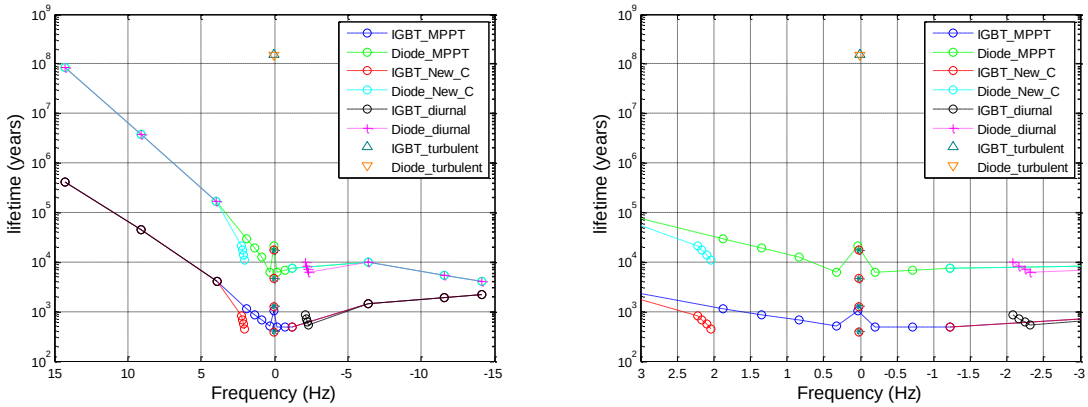

(a) Rotor Side **(b) Rotor Side, zoomed in**

Figure 7-23 Weibull adjusted Lifetime vs frequency including turbulent and diurnal cycling effect

Figure 7-23 shows the diurnal and turbulent thermal cycling superimposed onto the Weibull adjusted lifetime plot. The x-axis this time is frequency, as the new results are for variable wind conditions so are more easily plotted on the Lifetime vs wind speed plot.

At these low frequencies there is little difference between IGBT and diode lifetimes. The diurnal variation causes an extremely low frequency cycle and so the damage accumulation will be low, thus the lifetime is long. The turbulent component of wind speed variation has a much greater effect on lifetime and the effect is felt more strongly by the diode. This is due to the fact that the lifetimes here are calculated based on mean temperatures which for IGBT and diode are very similar which in turn is due to the fact these are values determined at steady state.

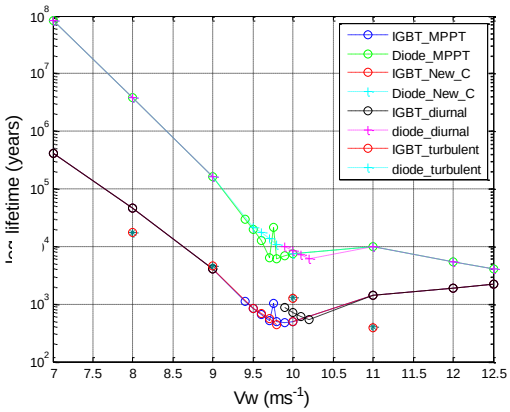

Figure 7-24 Weibull adjusted Lifetime vs Wind Speed including turbulent

It is clear that the strategy put forward in the current work of tackling the effects of low frequency cycling occurring in the synchronous zone means that the source of aging that is targeted is amongst the most significant. Figure 7-24 shows the lifetimes plotted against wind speed where the mean wind speed is used to plot the lifetimes resulting from turbulence induced thermal cycling. Thus the effect of the mean wind speed at which the turbulence occurs is very significant. To some extent this source of ageing has to be tolerated, at high wind speeds any modification to MPPT control will result in high sacrifice of energy captured. Damping from the turbine inertia will also help to reduce the effect of turbulence; in the current work any damping is not accounted for due to the simplified method used to determine the lifetimes for turbulence induced thermal cycling. The determination of the lifetime resulting from turbulent thermal cycling assumes a continual operation with the same turbulent intensity. In this sense the turbulent lifetimes (as well as the diurnal lifetimes) are not modified by a scaling factor accounting for the proportion of time that the turbulence of the selected magnitude is occurring. Where the MPPT and new controller lifetimes are modified by the Weibull distribution of wind speed, the turbulent and diurnal lifetimes should also be similarly scaled. This scaling would significantly increase the lifetimes as it is a clear simplification to assume continual operation at any turbulence intensity.

The new controller would have little effect upon the diurnal effect as this variation occurs while the turbine is moving through a large range of wind speeds (of which the synchronous zone is only a small part) thus excluding the synchronous zone would not prevent the temperature cycle occurring. For turbulence induced temperature cycling the new controller may slightly increase the damage accumulation caused, by virtue of the fact that mean junction temperatures in the synchronous zone are increased as compared with MPPT control. Cycling between these increased

junction temperatures will reduce lifetime. However, as the increase in mean temperatures resulting from new controller operation is small then any change in lifetime will also be small.

7.4. Summary

A new control algorithm for a DFIG WT is proposed based upon the commonly used MPPT but including an adaptation close to the synchronous operating point ±4%. Either side of the synchronous operating point the frequency is not allowed to reduce below certain limits. The effect is to prevent the system from operating at low frequencies and thus low frequency temperature cycling as experience by the converter under MPPT is avoided. Any modification to the MPPT control law implies a reduction in energy yield. This was quantified and gave a worst case scenario of 98.6% when the WT was running at any single operating point in steady state.

By forbidding the WT from operating within the synchronous zone a tipping point arises whereby in increasing wind the system is caused to accelerate from the low speed side of synchronous speed through a range of speed until reaching an upper threshold on the high speed side of synchronous. And likewise the reverse occurs when the wind reduces below a certain value. The response of the system at this tipping point was shown. A balancing act is required so that the WT can cross the synchronous zone in a controlled manner without large oscillations in speed when reaching the other side but at the same time does not take overly long to complete the crossing.

The improvement in lifetime of the devices was shown to be significant (up to 120% for the idealised case of continuous operation at a single wind speed). A simple determination of lifetimes resulting from the likely thermal cycling induced by turbulence and the diurnal variation in wind speed was carried out. Whilst the diurnal variation may be discounted as a significant contributor to thermal cycling induced aging (due to the extremely low frequency), the turbulent component of the wind speed variation is more significant. This indeed has a similar effect upon lifetime as does the low frequency thermal cycling. A modifying factor that would scale the lifetimes based on turbulence induced thermal cycling would increase the lifetimes calculated. Thus it can be said that the control strategy is targeting a key contributor to thermal cycling induced ageing of the converter devices.

Chapter 8. **Conclusion and further work**

9.1. Conclusion

This thesis examined the effect of temperature cycling upon the rotor side converter in a DFIG WT. It was seen that the greatest negative lifetime effect was found to occur around the synchronous operating point. This is due to the low frequency thermal cycling that occurs when the output frequency of the rotor side converter is also low. Avoidance of these damaging thermal cycles was targeted as a means of operational management to improve converter lifetime.

An adaptation to the standard MPPT control algorithm, used in WT applications, was proposed which designated a forbidden zone around the synchronous point. This controlled the system to avoid this zone and in so doing the minimum operating frequency was increased from 0 Hz to 2 Hz. Rotor speeds which would arise under MPPT within a band, approximately 6 rad.s^{-1} either side of synchronous speed, were not permitted by the controller thus moving the system off the MPPT curve with a resultant sacrifice of some energy capture.

The lifetime of the converter semiconductor devices as determined for continuous operation at constant wind speeds was increased when compared to MPPT operation. The lifetime increase varied across the wind speed spectrum but was zero outwith the near synchronous speed region as here the controller followed standard MPPT control. Lifetime improvements in the range of 10-120% were achieved at certain wind speeds. At the synchronous speed point there was a significant decrease in lifetime. This was because for the case of MPPT the frequency here was so low (ideally 0Hz) that very few cycles were occurring and although the temperature swing was maximised here the frequency dominated. This effect was limited to very close to synchronous speed (at frequencies less than 0.2Hz), and across most of the forbidden zone there was large lifetime improvement.

The energy sacrificed under the new control system was low. At the worst possible operating point the system could harvest 98.6% of the energy that was available when MPPT control was used - that being a loss of 20kW for the 2.5MW turbine. The power sacrificed tailed off sharply from this maximum. More specifically there was some asymmetry in the power sacrificed when it was plotted versus the wind speed. In the decreasing scenario (as when wind decreased from a wind speed above the synchronous region) the power sacrificed increased rapidly until the system was moved to the other side of synchronous by the controller where the power sacrificed reduced to a low

level. Whereas for the increasing scenario the power sacrificed was shared more equally on either side of synchronous again with the larger loss being on the slow speed side of synchronous.

The study shows that operational management could be a valuable strategy to extend the lifetime expectation of DFIG power converters. The strategy could be adopted easily by adapting the converter controller and would avoid the need to enhance the power electronic hardware, this being the preferred solution currently being adopted by several manufacturers who have recognised the need of reliability improvement on the rotor side converter. The method proposed in this study, based on what is meant to be a more in depth understanding of the root causes of the problem, has been thoroughly evaluated and shown to be acceptable.

8.1. Future work

There is scope for optimisation that was not performed in the current work. Depending on the distribution of wind speeds at a particular site there may be an advantage that can be gained in terms of reduction in energy sacrificed over the course of a year's operation by moving the boundaries of the forbidden zone slightly. The zone could be increased or decreased symmetrically or it could also be skewed to one side of the synchronous speed operating point (i.e. so that it was no longer symmetrically positioned around the synchronous speed operating point). This could be achieved by bringing one of the boundaries of the forbidden zone closer to synchronous speed which would mean that the converters minimum frequency was reduced and thus result in an effect on the lifetime. Alternatively the zone could be skewed to one side of the synchronous speed by merely extending the current forbidden zone either side of the synchronous speed. There is a trade-off here between reducing the amount of energy that is sacrificed and increasing the lifetime of the converter. Whereas the current work has been concerned with examining the concept of an adapted controller for converter lifetime improvement, the possibility of performing optimisation here is left open for future work. In the current work the lifetime improvement was significant enough to justify the reduction in energy yield and as mentioned this sacrifice in yield was low.

The transit of the forbidden zone was shown to take approximately 20s. It is possible the wind may increase by an amount sufficient to initiate a crossing of the forbidden zone, only for it to reduce again and cause the system to re-transit the zone. The hysteresis band is not particularly wide the wind speed has only to change by around $0.15ms^{-1}$ in either direction for a re-crossing of the forbidden zone to occur. This sort of wind variation is not at all unlikely and so there is room here for further study in the form of an examination of the effect of multiple crossings of the forbidden

zone. Further the effect, in terms of loss of energy yield, of increasing the size of the hysteresis band could be examined. The rapid acceleration of the system during the transit of the forbidden zone may have some implications as to reliability in other areas of the WT, where mechanical reliability is paramount. Drivetrain elements such as the gearbox, bearings and the electrical machine itself may be affected by this acceleration across the forbidden zone and especially if this was to occur often or in rapid succession. Also it is yet to be ascertained what would result if the wind speed was to change markedly during the crossing of the forbidden zone.

These dynamic issues regarding operation of the new control algorithm within the WT could be analysed and any lifetime effect of mechanical stressing determined. As the WT is constantly subjected to varying rotor speeds it seems unlikely that any lifetime effect would be significant. Nevertheless, comparison could be made between this lifetime effect and the gain in lifetime resulting from operation of the new controller.

The findings of the current work will be combined with a more realistic lifetime model developed by colleagues at Warwick University and a journal paper submitted.

References

[1] "Energy Technology Perspectives: Scenarios & Strategies to 2050," IEA2010.

[2] "World Energy Outlook Special Report: Redrawing the Energy-Climate Map," Intergovernmental Panel on Climate Change10 June 2013 2013.

[3] EWEA, "Wind in Power," Feb 2013 2013.

[4] "World Energy Outlook 2012 - Executive Summary," IEA2012.

[5] "Technology Roadmap Wind energy," IEA2009.

[6] "Global Wind Report Annual Market Update," GWEC, http://www.gwec.net/publications/global-wind-report-2/2012.

[7] "Uranium 2009: Resources, Production and Demand," A Joint Report by the OECD Nuclear Energy Agency and the International Atomic Energy Agency2010.

[8] I. Vanderhoven, "Power Spectrum of Horizontal Wind Speed in the Frequency Range from 0.0007 to 900 Cycles Per Hour," Journal of Meteorology, vol. 14, pp. 160-164, 1957.

[9] P. J. Tavner, J. Xiang, and F. Spinato, "Reliability analysis for wind turbines," Wind Energy, vol. 10, pp. 1-18, 2007.

[10] M. A. Levin and T. T. Kalal, "The Reliability Toolbox," in Improving Product Reliability, ed: John Wiley & Sons, Ltd, 2005, pp. 64-112.

[11] P. Tavner, "Wind Turbine Reliabiltiy – Can we see the Effects of Turbulence," Presentation at Durham University School of Engineering and Computer Sciences, 2012.

[12] P. Tavner, S. Faulstich, B. Hahn, and G. J. W. van Bussel, "Reliability & Availability of Wind Turbine Electrical & Electronic Components," EPE Journal, vol. 20, 2010.

[13] Y. Shaoyong, A. Bryant, P. Mawby, X. Dawei, L. Ran, and P. Tavner, "An Industry-Based Survey of Reliability in Power Electronic Converters," Industry Applications, IEEE Transactions on, vol. 47, pp. 1441-1451, 2011.

[14] Y. Shaoyong, X. Dawei, A. Bryant, P. Mawby, L. Ran, and P. Tavner, "Condition Monitoring for Device Reliability in Power Electronic Converters: A Review," Power Electronics, IEEE Transactions on, vol. 25, pp. 2734-2752, 2010.

[15] R. Bayerer, "Advanced packaging yields higher performance and reliability in power electronics," Microelectronics Reliability, vol. 50, pp. 1715-1719, 2010.

[16] C. Busca, "Modeling lifetime of high power IGBTs in wind power applications - An overview," in Industrial Electronics (ISIE), 2011 IEEE International Symposium on, 2011, pp. 1408-1413.

[17] I. F. Kovačević, U. Drofenik, and J. W. Kolar, "New physical model for lifetime estimation of power modules," in Power Electronics Conference (IPEC), 2010 International, 2010, pp. 2106-2114.

[18] M. Ciappa, "Selected failure mechanisms of modern power modules," Microelectronics Reliability, vol. 42, pp. 653-667, 2002.

[19] W. Lixiang, R. J. Kerkman, R. A. Lukaszewski, L. Haihui, and Y. Zhenhuan, "Analysis of IGBT Power Cycling Capabilities Used in Doubly Fed Induction Generator Wind Power System," Industry Applications, IEEE Transactions on, vol. 47, pp. 1794-1801, 2011.

[20] F. Van Hulle and N. Fichaux, "Powering europe : wind energy and the electricity grid," EWEA, Brussels, Belgium2010.

[21] S. Holstein, "LandWirtschaftsKammer," ed. online.

[22] P. Tavner, F. Spinato, G. Van Bussel, and E. Koutoulakos, "Reliability of different wind turbine concepts with relevance to offshore application," in European Wind Energy Conference & Exhibition, 2008, pp. 166-170.

[23] M. Wilkinson, B. Hendriks, F. Spinato, E. Gomez, H. Bulacio, J. Roca, P. Tavner, Y. Feng, and H. Long, "Methodology and results of the ReliaWind reliability field study," in European Wind Energy Conference, 2010.

[24] (March 2014). Continuous Reliability Enhancement for Wind (CREW) Database and Analysis Program. Available: http://energy.sandia.gov/?page_id=6682

[25] V. Peters, A. Ogilvie, and C. Bond, "Continuous Reliability Enhancement for Wind (CREW) Database: Wind Plant Reliability Benchmark," Sandia National Laboratories, Energy, Climate, & Infrastructure Security. energy. sandia. gov, 2012.

[26] P. Wyllie, P. J. Tavner, and L. Ran, "Visit To Converteam, UK 4th and 5th Aug, 2009," TR0018, 4-5 Aug 2009.

[27] W. Musial, S. Butterfield, and B. McNiff, "Improving wind turbine gearbox reliability," in Proceedings of the European wind energy conference, 2007.

[28] K. Smolders, H. Long, Y. Feng, and P. J. Tavner, "Reliability Analysis and Prediction of Wind Turbine Gearboxes " presented at the European Wind Energy Conference (EWEC 2010) 2010.

[29] J. Ribrant and L. Bertling, "Survey of failures in wind power systems with focus on Swedish wind power plants during 1997-2005," in Power Engineering Society General Meeting, 2007. IEEE, 2007, pp. 1-8.

[30] K. Alewine and W. Chen, "Wind turbine generator failure modes analysis and occurrence," in Wind Power 2010 Conference, Dallas, 2010.

[31] P. Tavner, "Review of condition monitoring of rotating electrical machines," Electric Power Applications, IET, vol. 2, pp. 215-247, 2008.

[32] S. Faulstich, M. Durstewitz, B. Hahn, K. Knorr, and K. Rohrig, "Windenergie Report Deutschland 2008," Institut für solare Energieversorgungstechnik (Hrsg.), Kassel, 2008.

[33] M. Wilkinson, K. Harman, B. Hendriks, F. Spinato, and T. van Delft, "Measuring wind turbine reliability, results of the reliawind project," in EWEA Conference, 2011, pp. 1-8.

[34] P. Tavner, S. Faulstich, B. Hahn, and G. Van Bussel, "Reliability and availability of wind turbine electrical and electronic components," EPE journal., vol. 20, 2011.

[35] F. Spinato, "The reliability of wind turbines," University of Durham, 2008.

[36] F. Spinato, P. J. Tavner, G. J. W. van Bussel, and E. Koutoulakos, "Reliability of wind turbine subassemblies," Renewable Power Generation, IET, vol. 3, pp. 387-401, 2009.

[37] P. J. Tavner, G. J. W. Van Bussel, and F. Spinato, "Machine and Converter Reliabilities in Wind Turbines," in Power Electronics, Machines and Drives, 2006. The 3rd IET International Conference on, 2006, pp. 127-130.

[38] U. I. Dayaratne, S. B. Tennakoon, N. Y. A. Shammas, and J. S. Knight, "Investigation of variable DC link voltage operation of a PMSG based wind turbine with fully rated converters at steady state," in Power Electronics and Applications (EPE 2011), Proceedings of the 2011-14th European Conference on, 2011, pp. 1-10.

[39] I. Trintis, S. Munk-Nielsen, F. Abrahamsen, and P. B. Thoegersen, "Efficiency and reliability improvement in wind turbine converters by grid converter adaptive control," in Power Electronics and Applications (EPE), 2013 15th European Conference on, 2013, pp. 1-9.

[40] V. A. Sankaran, C. Chen, C. S. Avant, and X. Xu, "Power cycling reliability of IGBT power modules," in Industry Applications Conference, 1997. Thirty-Second IAS Annual Meeting, IAS '97., Conference Record of the 1997 IEEE, 1997, pp. 1222-1227 vol.2.

[41] M. Ciappa and W. Fichtner, "Lifetime prediction of IGBT modules for traction applications," in Reliability Physics Symposium, 2000. Proceedings. 38th Annual 2000 IEEE International, 2000, pp. 210-216.

[42] H. Hui, A. T. Bryant, and P. A. Mawby, "Electro-thermal modelling of three phase inverter," in Power Electronics and Applications (EPE 2011), Proceedings of the 2011-14th European Conference on, 2011, pp. 1-7.

[43] W. Lixiang, R. J. Kerkman, R. A. Lukaszewski, B. P. Brown, N. Gollhardt, and B. W. Weiss, "Junction Temperature Prediction of a Multiple-chip IGBT Module under DC Condition," in Industry Applications Conference, 2006. 41st IAS Annual Meeting. Conference Record of the 2006 IEEE, 2006, pp. 754-762.

[44] P. Cova and F. Fantini, "On the effect of power cycling stress on IGBT modules," Microelectronics Reliability, vol. 38, pp. 1347-1352, 1998.

[45] W. Lixiang, R. J. Kerkman, and R. A. Lukaszewski, "Evaluation of Power Semiconductors Power Cycling Capabilities for Adjustable Speed Drive," in Industry Applications Society Annual Meeting, 2008. IAS '08. IEEE, 2008, pp. 1-10.

[46] W. W. Lee, L. T. Nguyen, and G. S. Selvaduray, "Solder joint fatigue models: review and applicability to chip scale packages," Microelectronics Reliability, vol. 40, pp. 231-244, 2000.

[47] M. Ciappa, F. Carbognani, and W. Fichtner, "Lifetime prediction and design of reliability tests for high-power devices in automotive applications," Device and Materials Reliability, IEEE Transactions on, vol. 3, pp. 191-196, 2003.

[48] K. Mainka, M. Thoben, and O. Schilling, "Lifetime calculation for power modules, application and theory of models and counting methods," in Power Electronics and Applications (EPE 2011), Proceedings of the 2011-14th European Conference on, 2011, pp. 1-8.

[49] L. GopiReddy, L. M. Tolbert, and B. Ozpineci, "Lifetime prediction of IGBT in a STATCOM using modified-graphical rainflow counting algorithm," in IECON 2012 - 38th Annual Conference on IEEE Industrial Electronics Society, 2012, pp. 3425-3430.

[50] H. Hui and P. A. Mawby, "A Lifetime Estimation Technique for Voltage Source Inverters," Power Electronics, IEEE Transactions on, vol. 28, pp. 4113-4119, 2013.

[51] R. Bayerer, T. Herrmann, T. Licht, J. Lutz, and M. Feller, "Model for Power Cycling lifetime of IGBT Modules - various factors influencing lifetime," in Integrated Power Systems (CIPS), 2008 5th International Conference on, 2008, pp. 1-6.

[52] M. Held, P. Jacob, G. Nicoletti, P. Scacco, and M. H. Poech, "Fast power cycling test of IGBT modules in traction application," in Power Electronics and Drive Systems, 1997. Proceedings., 1997 International Conference on, 1997, pp. 425-430 vol.1.

[53] M. Ke, M. Liserre, and F. Blaabjerg, "Lifetime estimation for the power semiconductors considering mission profiles in wind power converter," in Energy Conversion Congress and Exposition (ECCE), 2013 IEEE, 2013, pp. 2962-2971.

[54] E. Baygildina, P. Peltoniemi, O. Pyrhonen, M. Ke, and F. Blaabjerg, "Thermal loading of wind power converter considering dynamics of wind speed," in Industrial Electronics Society, IECON 2013 - 39th Annual Conference of the IEEE, 2013, pp. 1362-1367.

[55] K. Xie, Z. Jiang, and W. Li, "Effect of Wind Speed on Wind Turbine Power Converter Reliability," Energy Conversion, IEEE Transactions on, vol. 27, pp. 96-104, 2012.

[56] M. Ke and F. Blaabjerg, "Multilevel converters for 10 MW Wind Turbines," in Power Electronics and Applications (EPE 2011), Proceedings of the 2011-14th European Conference on, 2011, pp. 1-10.

[57] M. Arifujjaman and C. Liuchen, "Reliability comparison of power electronic converters used in grid-connected wind energy conversion system," in Power Electronics for Distributed Generation Systems (PEDG), 2012 3rd IEEE International Symposium on, 2012, pp. 323-329.

[58] N. Holtsmark and M. Molinas, "Thermal analysis of matrix and Back-To-Back converters for series-connected wind turbines," in Industrial Electronics Society, IECON 2013 - 39th Annual Conference of the IEEE, 2013, pp. 4967-4972.

[59] R. Pittini, S. D'Arco, M. Hernes, and A. Petterteig, "Thermal stress analysis of IGBT modules in VSCs for PMSG in large offshore Wind Energy Conversion Systems," in Power Electronics and Applications (EPE 2011), Proceedings of the 2011-14th European Conference on, 2011, pp. 1-10.

[60] M. Musallam and C. M. Johnson, "Impact of different control schemes on the life consumption of power electronic modules for variable speed wind turbines," in Power Electronics and Applications (EPE 2011), Proceedings of the 2011-14th European Conference on, 2011, pp. 1-9.

[61] W. Lixiang, R. J. Kerkman, R. A. Lukaszewski, L. Haihui, and Y. Zhenhuan, "Analysis of IGBT power cycling capabilities used in Doubly Fed Induction Generator wind power system," in Energy Conversion Congress and Exposition (ECCE), 2010 IEEE, 2010, pp. 3076-3083.

[62] M. Bartram, J. von Bloh, and R. W. De Doncker, "Doubly-fed-machines in wind-turbine systems: is this application limiting the lifetime of IGBT-frequency-converters?," in Power

Electronics Specialists Conference, 2004. PESC 04. 2004 IEEE 35th Annual, 2004, pp. 2583-2587 Vol.4.

[63] M. Bruns, B. Rabelo, and W. Hofmann, "Investigation of doubly-fed induction generator drives behaviour at synchronous operating point in wind turbines," in Power Electronics and Applications, 2009. EPE '09. 13th European Conference on, 2009, pp. 1-10.

[64] T. Lei, M. Barnes, and A. C. Smith, "Thermal cycling evaluation for DFIG wind turbine power converter based on joint modelling," in Energy Conversion Congress and Exposition (ECCE), 2013 IEEE, 2013, pp. 3845-3851.

[65] J. Jung and W. Hofmann, "Investigation of thermal stress in the rotor of Doubly-Fed Induction Generators at synchronous operating point," in Electric Machines & Drives Conference (IEMDC), 2011 IEEE International, 2011, pp. 896-901.

[66] D. A. Murdock, J. E. Ramos, J. J. Connors, and R. D. Lorenz, "Active thermal control of power electronics modules," in Industry Applications Conference, 2003. 38th IAS Annual Meeting. Conference Record of the, 2003, pp. 1511-1515 vol.3.

[67] V. Blasko, R. Lukaszewski, and R. Sladky, "On line thermal model and thermal management strategy of a three phase voltage source inverter," in Industry Applications Conference, 1999. Thirty-Fourth IAS Annual Meeting. Conference Record of the 1999 IEEE, 1999, pp. 1423-1431 vol.2.

[68] W. Lixiang, J. McGuire, and R. A. Lukaszewski, "Analysis of PWM Frequency Control to Improve the Lifetime of PWM Inverter," Industry Applications, IEEE Transactions on, vol. 47, pp. 922-929, 2011.

[69] Z. Jianwen, C. Gen, and C. Xu, "Thermal smooth control for Multi-MW parallel wind power converter," in TENCON 2013 - 2013 IEEE Region 10 Conference (31194), 2013, pp. 1-4.

[70] M. Ke, M. Liserre, and F. Blaabjerg, "Reactive power influence on the thermal cycling of multi-MW wind power inverter," in Applied Power Electronics Conference and Exposition (APEC), 2012 Twenty-Seventh Annual IEEE, 2012, pp. 262-269.

[71] Z. Dao, F. Blaabjerg, M. Lau, and M. Tonnes, "Thermal Behavior Optimization in Multi-MW Wind Power Converter by Reactive Power Circulation," Industry Applications, IEEE Transactions on, vol. 50, pp. 433-440, 2014.

[72] J. Birk and B. Andresen, "Parallel-connected converters for optimizing efficiency, reliability and grid harmonics in a wind turbine," in Power Electronics and Applications, 2007 European Conference on, 2007, pp. 1-7.

[73] Z. Dao, F. Blaabjerg, M. Lau, and M. Tonnes, "Thermal profile analysis of Doubly-Fed induction generator based wind power converter with air and liquid cooling methods," in Power Electronics and Applications (EPE), 2013 15th European Conference on, 2013, pp. 1-10.

[74] L. Meysenc, M. Jylhakallio, and P. Barbosa, "Power electronics cooling effectiveness versus thermal inertia," Power Electronics, IEEE Transactions on, vol. 20, pp. 687-693, 2005.

[75] W. J. Choy, A. Castellazzi, and P. Zanchetta, "Adaptive cooling of power modules for reduced power and thermal cycling," in Power Electronics and Applications (EPE 2011), Proceedings of the 2011-14th European Conference on, 2011, pp. 1-10.

[76] R. Pena, J. C. Clare, and G. M. Asher, "Doubly fed induction generator using back-to-back PWM converters and its application to variable-speed wind-energy generation," Electric Power Applications, IEE Proceedings -, vol. 143, pp. 231-241, 1996.

[77] R. Pena, J. C. Clare, and G. M. Asher, "A doubly fed induction generator using back-to-back PWM converters supplying an isolated load from a variable speed wind turbine," Electric Power Applications, IEE Proceedings -, vol. 143, pp. 380-387, 1996.

[78] G. Abad, L. Marroyo, and G. Iwanski, Doubly fed induction machine: modeling and control for wind energy generation vol. 86: Wiley. com, 2011.

[79] P. C. Krause, O. Wasynczuk, and S. D. Sudhoff, Analysis of electric machinery and drive systems, 2nd ed.: IEEE Press (New York), 2002.

[80] A. Petersson, L. Harnefors, and T. Thiringer, "Comparison between stator-flux and grid-flux-oriented rotor current control of doubly-fed induction generators," in Power Electronics Specialists Conference, 2004. PESC 04. 2004 IEEE 35th Annual, 2004, pp. 482-486 Vol.1.

[81] M. Canas-Carreton, A. Vigueras-Rodriguez, and A. Molina-Garcia, "Rotor-Side Control Schemes for DFIG Wind Turbines: Comparison of Approaches," presented at the EWEA, Brussels, 2011.

[82] J. B. Ekanayake, L. Holdsworth, W. XueGuang, and N. Jenkins, "Dynamic modeling of doubly fed induction generator wind turbines," Power Systems, IEEE Transactions on, vol. 18, pp. 803-809, 2003.

[83] A. Tapia, G. Tapia, J. X. Ostolaza, and J. R. Saenz, "Modeling and control of a wind turbine driven doubly fed induction generator," Energy Conversion, IEEE Transactions on, vol. 18, pp. 194-204, 2003.

[84] "PLECS," ed. http://www.plexim.com/.

[85] C. Liu, Y. Kang, J. Chen, L. Kevin, X. Lin, X. Liu, and F. Xu, "Simplified Active and Reactive Power Control of Doubly Fed Induction Generator and the Simulation with STATCOM," in Applied Power Electronics Conference and Exposition, 2009. APEC 2009. Twenty-Fourth Annual IEEE, 2009, pp. 1927-1931.

[86] C. Wessels, F. Gebhardt, and F. W. Fuchs, "Fault Ride-Through of a DFIG Wind Turbine Using a Dynamic Voltage Restorer During Symmetrical and Asymmetrical Grid Faults," Power Electronics, IEEE Transactions on, vol. 26, pp. 807-815, 2011.

[87] M. J. Kadhim and D. Chavan, "Improvement Fault-ride Through of DFIG Based Wind Turbines by Using a Series Compensation Technology with Emphasis Put on the Mitigation of Voltage Dips," vol. 2, May, 2013 2013

[88] T. Ackermann, Wind power in power systems vol. 140: Wiley Online Library, 2005.

[89] J. L. Duarte, A. Van Zwam, C. Wijnands, and A. Vandenput, "Reference frames fit for controlling PWM rectifiers," Industrial Electronics, IEEE Transactions on, vol. 46, pp. 628-630, 1999.

[90] A. Ourici, "Double flux orientation control for a doubly fed induction machine," International Journal of Electrical Power & Energy Systems, vol. 43, pp. 617-620, 2012.

[91] Semikron. (2012). Available: http://www.semikron.co.uk/products/data/cur/assets/SKiiP_2013_GB172_4DL_V3_20450182.pdf

[92] A. Wintrich, U. Nicolai, W. Tursky, and T. Reimann, Application Manual Power Semiconductors: SEMIKRON International GmbH, 2011.

[93] "PicoLog Data Acquisition Software," vol. 2014, ed. http://www.picotech.com/data-logging-software.html, 2014.

[94] C. J. Crabtree, "Condition Monitoring Techniques for Wind Turbines," Durham University, 2011.

Appendix

SKiiP 2013 GB172-4DL V3

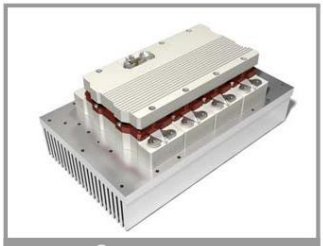

SKiiP® 3

2-pack-integrated intelligent Power System

SKiiP 2013 GB172-4DL V3

Features

- SKiiP technology inside
- Trench IGBTs
- CAL HD diode technology
- Integrated current sensor
- Integrated temperature sensor
- Integrated heat sink
- UL recognized File no. E63532

Typical Applications*

- Renewable energies
- Traction
- Elevators
- Industrial drives

Footnotes

[1] With assembly of suitable MKP capacitor per terminal

Absolute Maximum Ratings			T_s = 25°C unless otherwise specified	
Symbol	**Conditions**		**Values**	**Unit**
System				
V_{CC} [1]	Operating DC link voltage		1200	V
V_{isol}	DC, t = 1 s, main terminals to heat sink		5600	V
$I_{t(RMS)}$	per AC terminal, $T_{terminal}$ <115°C		400	A
I_{FSM}	T_j = 125 °C, t_p = 10 ms, sin 180°		13500	A
I^2t	T_j = 150 °C, t_p = 10 ms, diode		911	kA^2s
f_{out}	fundamental output frequency		1	kHz
T_{stg}	storage temperature		-40 ... 85	°C
IGBT				
V_{CES}	T_j = 25 °C		1700	V
I_C	T_j = 150 °C	T_s = 25 °C	2102	A
		T_s = 70 °C	1617	A
I_{Cnom}			2000	A
T_j	junction temperature		-40 ... 150	°C
Diode				
V_{RRM}	T_j = 25 °C		1700	V
I_F	T_j = 150 °C	T_s = 25 °C	1758	A
		T_s = 70 °C	1338	A
I_{Fnom}			1650	A
T_j	junction temperature		-40 ... 150	°C
Driver				
V_s	power supply		13 ... 30	V
V_{iH}	input signal voltage (high)		15 + 0.3	V
V_{isolPD}	QPD <= 10pC, PRIM to POWER		1500	V
dv/dt	secondary to primary side		75	kV/µs
f_{sw}	switching frequency		7	kHz

Characteristics			T_s = 25°C unless otherwise specified			
Symbol	**Conditions**		**min.**	**typ.**	**max.**	**Unit**
IGBT						
$V_{CE(sat)}$	I_C = 1200 A at terminal	T_j = 25 °C		1.9	2.4	V
		T_j = 125 °C		2.2		V
V_{CE0}		T_j = 25 °C		1.00	1.20	V
		T_j = 125 °C		0.90	1.10	V
r_{CE}	at terminal	T_j = 25 °C		0.75	0.95	mΩ
		T_j = 125 °C		1.1	1.3	mΩ
$E_{on} + E_{off}$	I_C = 1200 A, T_j = 125 °C	V_{CC} = 900 V		780		mJ
		V_{CC} = 1200 V		1150		mJ
$R_{th(j-s)}$	per IGBT switch				0.015	K/W
$R_{th(j-r)}$	per IGBT switch				0.015	K/W

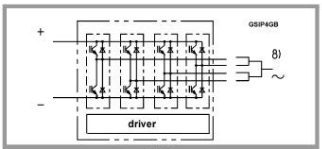

S43

SKiiP 2013 GB172-4DL V3

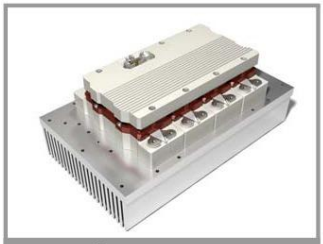

SKiiP® 3

2-pack-integrated intelligent Power System

SKiiP 2013 GB172-4DL V3

Features

- SKiiP technology inside
- Trench IGBTs
- CAL HD diode technology
- Integrated current sensor
- Integrated temperature sensor
- Integrated heat sink
- UL recognized File no. E63532

Typical Applications*

- Renewable energies
- Traction
- Elevators
- Industrial drives

Footnotes

[1] With assembly of suitable MKP capacitor per terminal

Characteristics			T_s = 25°C unless otherwise specified			
Symbol	**Conditions**		**min.**	**typ.**	**max.**	**Unit**
Diode						
$V_F = V_{EC}$	I_F = 1200 A at terminal	T_j = 25 °C		2.00	2.15	V
		T_j = 125 °C		1.80		V
V_{F0}		T_j = 25 °C		1.1	1.2	V
		T_j = 125 °C		0.8	0.9	V
r_F	at terminal	T_j = 25 °C		0.74	0.8	mΩ
		T_j = 125 °C		0.8	0.9	mΩ
E_{rr}	I_F = 1200 A, T_j = 125 °C	V_R = 900 V		144		mJ
		V_R = 1200 V		171		mJ
$R_{th(j-s)}$	per diode switch				0.029	K/W
$R_{th(j-r)}$	per diode switch				0.048	K/W
Driver						
V_s	supply voltage non stabilized		13	24	30	V
I_{S0}	bias current @V_s=24V, f_{sw} = 0, I_{AC} = 0			330		mA
I_s	k_1 = 55 mA/kHz, k_2 = 0.00035 mA/A²		= 330	+ k_1* f_{sw}	+ k_2 * I_{AC}^2	mA
V_{IT+}	input threshold voltage (HIGH)		12.3			V
V_{IT-}	Input threshold voltage (LOW)				4.6	V
R_{IN}	input resistance			10		kΩ
C_{IN}	input capacitance			1		nF
t_{pRESET}	error memory reset time			0.0122		ms
t_{TD}	top / bottom switch interlock time			3		µs
t_{jitter}	jitter clock time			125		ns
t_{SIS}	short pulse suppression time			0.625	0.7	µs
I_{TRIPSC}	over current trip level		2450	2500	2550	A_{PEAK}
T_{trip}	over temperature trip level		110	115	120	°C
V_{DCtrip}	over voltage trip level,			not impl.		V
$t_{d(on)IO}$	V_{CC} = 1200 V, I_C = 1200 A, T_j = 25 °C	input-output turn-on propagation time		1.4		µs
$t_{d(off)IO}$		input-output turn-off propagation time		1.4		µs
System						
$R_{th(r-a)}$	flow rate=390m³/h, T_a=25°C, 500m above sea level				0.0255	K/W
$R_{CC'+EE'}$	terminals to chip, T_s = 25 °C			0.13		mΩ
L_{CE}	commutation inductance			3		nH
C_{CHC}	per phase, AC-side			6.8		nF
I_{CES} + I_{RD}	V_{GE} = 0 V, V_{CE} = 1700 V, T_j = 25 °C			4.8		mA
M_{dc}	DC terminals, SI Units		6		8	Nm
M_{ac}	AC terminals, SI Units		13		15	Nm
w	SKiiP System w/o heat sink			3.1		kg
w_h	heat sink			8		kg

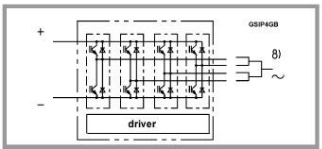

S43

Isolation coordination acc. to EN 50178 and IEC 61800-5-1	
Maximum grid RMS voltage, line-to-line, star point grounded mains	690V+20%
Installation altitude for maximum grid RMS voltage, line-to-line, star point grounded mains	2000m
Maximum transient peak voltage between low voltage circuit and mains	1600V
Pollution degree acc. to IEC 60664-1 outside the moulded power section	2
Overvoltage cat. acc. to IEC 60664-1 for mains	III
Basic isolation	between heat sink and mains; between low voltage circuit and mains
Protection level acc. to IEC 60529	IP00

Environmental conditions acc.to IEC 60721

	Storage	Transportation	Operation stationary use at weather protected locations	Operating ground vehicle installations	Operating ship environment
Climatic conditions	1K2(1)	2K2(1)	3K3(1)	5K1(1)	---
Biological conditions	1B1	2B1	3B1	5B1	6B1
Chemically active substances (excluded: salt spray)	1C2	2C1	3C2	5C2	6C2
Mechanically active substances	1S1	2S1	3S1	5S1	6S1
Mechanical conditions	1M3	(4)	3M6(2)	5M3(3)	6M3
Contaminating fluids	---	---	---	5F1	---

(1) expanded temperature range: -40°C / +85°C. Please note: by operation near 85°C the life time of product is reduced.
(2) 3M7 possible, but due to the mechanic load capacity of external components like DC-Link capacitors limited to 3M6
(3) 5M3 without impact of foreign bodies, stones
(4) no declaration due to customer-specific packing

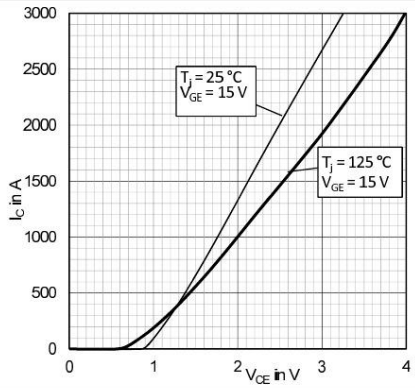

Fig. 1: Typical IGBT output characteristic

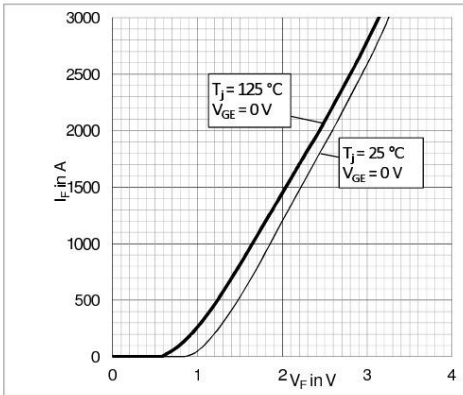

Fig. 2: Typical diode output characteristics

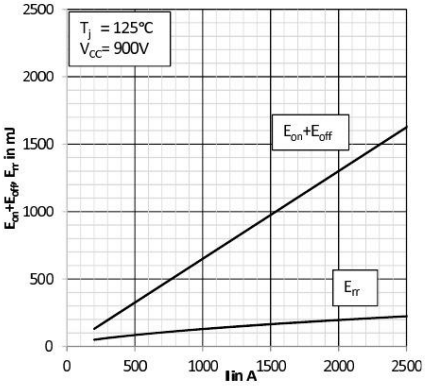

Fig. 3: Typical energy losses E = f(I_c, V_{cc})

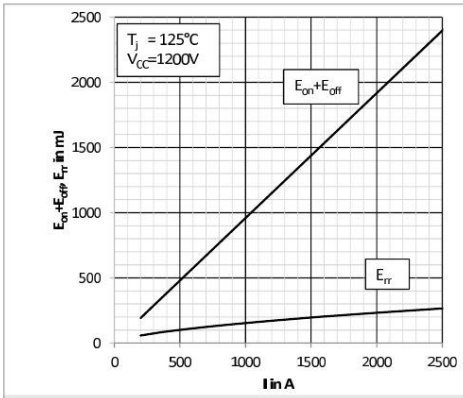

Fig. 4: Typical energy losses E = f(I_c, V_{cc})

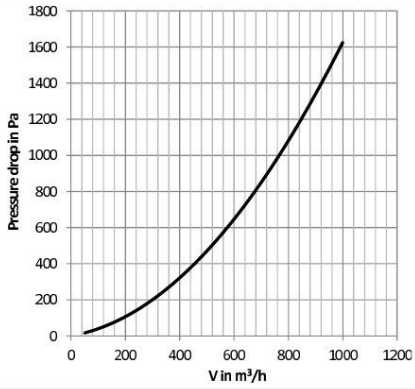

Fig. 5: Pressure drop Δp versus flow rate V

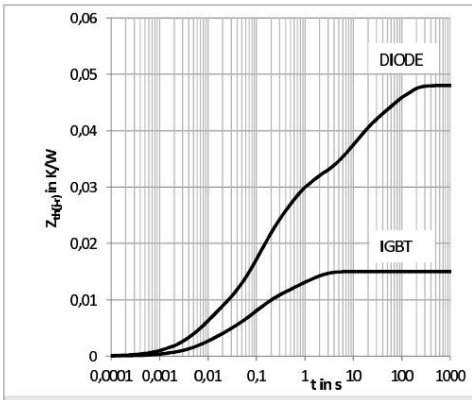

Fig. 6: Transient thermal impedance Zth(j-r)

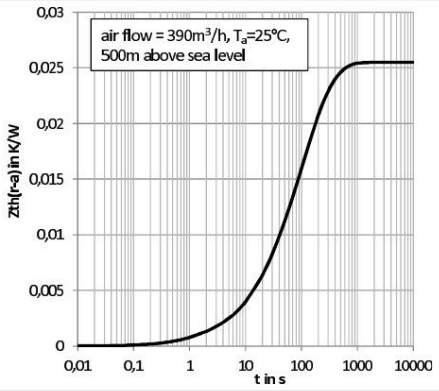

Fig. 7: Transient thermal impedance Zth(r-a)

	R_{th} [K/W]					
	1	2	3	4	5	6
$Z_{th(j-r)}$ I	0,0027	0,0055	0,0022	0,0046	0,0000	0,0000
$Z_{th(j-r)}$ D	0,0061	0,0126	0,0113	0,0076	0,0019	0,0085
$Z_{th(r-a)}$	0,0008	0,0030	0,0120	0,0097	0,0000	0,0000
	tau [s]					
	1	2	3	4	5	6
$Z_{th(j-r)}$ I	0,0090	0,0700	0,2200	1,1000	1,0000	1,0000
$Z_{th(j-r)}$ D	0,0070	0,0850	0,4400	8,3000	12,000	72,000
$Z_{th(r-a)}$	1,3800	17,000	82,000	209,00	1,0000	1,0000

Fig. 8: Coefficients of thermal impedances

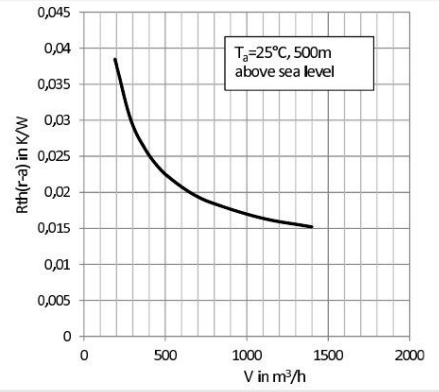

Fig. 9: Thermal resistance Rth(r-a) versus flow rate V

This is an electrostatic discharge sensitive device (ESDS), international standard IEC 60747-1, Chapter IX

* The specifications of our components may not be considered as an assurance of component characteristics. Components have to be tested for the respective application. Adjustments may be necessary. The use of SEMIKRON products in life support appliances and systems is subject to prior specification and written approval by SEMIKRON. We therefore strongly recommend prior consultation of our staff.